

DEPARTMENT OF PHYSICS AND ASTRONOMY
UNIVERSITY OF HEIDELBERG

Bachelor Thesis in Physics
submitted by

Friederike Bock

born in Gardelegen (Germany)

2010

ALICE Capabilities for Studying Photon Physics with the Conversion Method at LHC Energies

This Bachelor Thesis has been carried out by Friederike Bock at the
Physikalisches Institut at the University of Heidelberg
under the supervision of
Prof. Dr. Johanna Stachel

ALICE Capabilities for Studying Photon Physics with the Conversion Method at LHC Energies

We will present a detailed γ -ray tomography of the ALICE detector system at the LHC obtained with the first data taken at a center of mass energy of $\sqrt{s_{NN}} = 7$ TeV from March to June of the year 2010. The measurement is based on photons that convert into electron positron pairs in the material of the Inner Tracking System and the Time Projection Chamber, resulting in a two track event signature. To show the precision of the method a resolution study will be presented as well. The very good resolution obtained with this method was essential in order to localize discrepancies in the simulation of the detector material. Moreover, due to the good resolution it is used to estimate the systematic uncertainty of the material budget of the detector. The first estimation of the systematic error gives an error of the order of $\pm 4\%$ after the first iteration of the simulations. Additionally the photon signals which are expected from the Quark Gluon Plasma will be discussed.

Leistungsfähigkeit des ALICE Detektors zur Untersuchung der Physik von Photonen mittels Photonenkonversionen bei LHC Energien

In dieser Arbeit wird eine detaillierte γ -Ray Tomographie des ALICE Detektors am LHC vorgestellt. Diese wurde mittels Photonenkonversionen unter Verwendung der ersten Daten bei einer Kollisionsenergie von $\sqrt{s_{NN}} = 7$ TeV aus dem Zeitraum März bis Juni 2010 erstellt. Hierbei wurden Ereignisse benutzt, bei denen Photonen im Detektormaterial des Inner Tracking Systems und der Time Projection Chamber in Elektron-Positron-Paare konvertieren. Dies führt zu einer Zwei-Spuren-Ereignissignatur. Um die Genauigkeit der Methode zu verdeutlichen, wurde ebenfalls eine Auflösungsstudie durchgeführt. Auch diese Ergebnisse werden in der vorliegenden Arbeit präsentiert. Die sehr gute Auflösung die mit der Methode erreicht wird war essentiell für das Auffinden von Unterschieden in der Simulation des Detektormaterials. Es zeigt sich, dass aufgrund ihrer guten Präzision die Photonenkonversionsmethode benutzt werden kann, um eine erste Abschätzung der systematischen Ungenauigkeit des verwendeten Detektormaterials zu geben. Diese ist nach der ersten Verbesserung im Bereich der Simulationen mit $\pm 4\%$ anzugeben. Des weiteren werden in dieser Arbeit Photonensignale, die aus dem Quark-Gluon-Plasma herrühren diskutiert.

Contents

1. Introduction	3
2. Theoretical Background	5
2.1. The Standard Model	5
2.2. Quantum Chromodynamics (QCD)	6
2.3. The Quark Gluon Plasma (QGP)	7
2.3.1. Quark Gluon Plasma and the Critical Parameters	7
2.3.2. General Signatures for the Quark Gluon Plasma	8
2.3.3. Photon signals from heavy ion collisions	9
3. Interactions of photons and electrons with matter	13
3.1. Interactions of photons with matter	13
3.1.1. The Photoelectric Effect	13
3.1.2. Compton Scattering	14
3.1.3. Pair creation	14
3.2. Interactions of electrons (positrons) with matter	16
3.2.1. Energy Loss by Ionisation	17
3.2.2. Bremsstrahlung	17
3.2.3. Transition and Cherenkov radiation	18
4. The Experimental Apparatus	19
4.1. The Large Hadron Collider (LHC)	19
4.2. A Large Ion Collider Experiment (ALICE)	21
4.2.1. The Detectors	21
4.2.2. The Trigger System (TRG)	24
4.2.3. Track and Vertex Reconstruction	25
4.3. Comparison of ALICE, ATLAS and CMS with respect to the Capability for Photon Measurements	28
5. Measurement of Photon Conversions in ALICE	31
5.1. The V0 reconstruction method	31
5.2. Reconstruction of the Conversion Point	32
5.3. Data set, event selection and Monte Carlo simulations	34
5.4. Sample of photons	35
5.5. Creating pure photon samples	37
5.6. Characteristics of selected photons	39
6. The Material Budget of the ALICE Detector	43
6.1. Mapping of the different detectors	43
6.2. Material Budget of the ITS	49
6.3. Material Budget of the TPC	52
6.4. Systematic Error Estimation for the Material Budget	55

7. Studies of the Resolution of the Conversion Method	57
7.1. Spatial Resolution of the Conversion Point	58
7.2. Momentum Resolution of the Conversion Method	62
7.3. TRD characteristics for electrons (positrons) from conversions	65
8. Conclusions and Outlook	67
A. Acronyms and Technical Terms	69
B. Mapping Figures of the different Detectors onfly V0 finder	71
C. Mapping Figures of the different Detectors offline V0 finder	81
D. Tables	91

1. Introduction

*”Dass ich erkenne, was die Welt
Im Innersten zusammenhält,
Schau alle Wirkenskraft und Samen,
und tu nicht mehr in Worten kramen.”*

Johann Wolfgang Goethe, Faust I, Studierzimmer I, Uraufführung im Jahr 1829

*“So that I may perceive whatever holds
the world together in its inmost folds,
See all its seeds, its working power,
And cease word-threshing from this hour.”*

Johann Wolfgang Goethe, Faust I, Study I, first performance in the year 1829

Children often ask, why something happens, how it works and how it can be explained. It is part of human nature to question our environment. But sometimes while growing older one loses the ability of questioning things. Scientists on the other hand keep asking these questions, as well as they try to prove their theories for the answers of the questions. Furthermore it is a central theme in literature, as it can be seen in the quotation from “Faust I” the famous play of Goethe. Searching for the origin of matter and its forces is a central part of current physics as well.

This was the main reason for building the Large Hadron Collider (LHC) at the European Organization for Nuclear Research (Conseil Européen pour la Recherche Nucléaire - CERN) near Geneva, Switzerland. At the LHC protons with a center of mass energy of up to $\sqrt{s} = 14$ TeV or heavy ions up to an energy of $\sqrt{s_{NN}} = 5.5$ TeV per nucleon-nucleon pair will be colliding in the four main experiments. Such conditions were never reached before and will therefore offer a new possibility to test the current theories. Furthermore, heavy ion collisions will provide a new insight into Quantum Chromodynamics and especially the Quark Gluon Plasma (QGP).

The experiment dedicated to heavy ion collisions at the LHC is the “A Large Ion Collider Experiment” (ALICE), at which this thesis was carried out with the first data taken at the end of the year 2009 and from March to June of the year 2010.

This thesis will give an overview of the photon signals from the Quark Gluon Plasma which can be measured in the different experiments. Moreover, it will give a detailed γ -ray tomography of the ALICE detector, obtained with the photon conversions measured in the Inner Tracking System

(ITS) and the Time Projection Chamber (TPC) of the ALICE detector. The conversion method, which was used for this studies will be explained in detail and its resolutions will be investigated. With this method the real detector structures in the ALICE experiment can be measured. As the measurement is very precise it allows to give a first error estimation to the material used for the detectors and being implemented in the detector simulations. The error of the material budget will influence most of the physics analysis of the experiment and therefore needs to be decreased as much as possible. Through the investigations carried out for this thesis and the effort of the experts to improve the simulation the systematic error could already be decreased to $\pm 4\%$. However, there is still work ongoing to decrease the error of material budget even more. Additionally, a first study was carried out towards a trigger for high energetic photons measured with the conversion method defined by the Transition Radiation Detector (TRD) of ALICE. The results will be presented as well.

In order to address these topics I will first explain the theory of the Standard Model as well as the theoretical background for signals from the Quark Gluon plasma and the signals themselves (see chapter 2). Afterwards, the theory for the detection of photons will be discussed (see chapter 3), which will then lead over to the presentation of the detectors used for the analysis in chapter 4. Furthermore, an explanation of the conversion method will be given in chapter 5. The material studies will be addressed in chapter 6. Afterwards, chapter 7 will be dedicated to the resolution of the conversion method and the simulation studies towards the trigger. Finally, a short summary of the capabilities of this method will be presented together with the opportunities for the future.

2. Theoretical Background

2.1. The Standard Model

The Standard Model, invented by S. L. Glashow [1], A. Salam [2,3], and S. Weinberg [4] in 1967/8, for which they got the noble prize in 1979, describes the constituents of matter as well as their interactions. In figure 2.1 the fundamental particles of this theory are shown, namely the quarks and leptons, each organized in three generations, and the four gauge bosons mediating the fundamental forces. In addition to the quarks and leptons, fundamental particles with opposite charge but same mass, so called, anti-particles, are needed for building the particles observed in experiments. The Standard Model is already tested very well. This model does not yet include the gravitational force. But for high energy physics the effects of gravitation are rather small and therefore they can be neglected in the calculations. However theorists continuously try to develop a Grand Unified Theory (GUT), containing all four forces, which is then valid at all scales of energy, velocity and space.

One of the remaining open issues is: What causes the fundamental particles to have matter? In 1964 Peter Higgs proposed the Gauge-bosons to get matter by the so called Higgs-mechanism, which can be described as an extension of the spontaneous symmetry breaking to create massive vector bosons in a gauge invariant theory. This theory was reviewed several times and seems to be the most promising answer to the problem of having massive particles. It will be tested at LHC energies mainly in the ATLAS (A Toroidal LHC ApparatuS) and the CMS (Compact Muon Solenoid) experiments.

Three Generations of Matter (fermions)				
	I	II	III	
mass →	2.4 MeV	1.27 GeV	171.2 GeV	0
charge →	$\frac{2}{3}$	$\frac{2}{3}$	$\frac{2}{3}$	0
spin →	$\frac{1}{2}$	$\frac{1}{2}$	$\frac{1}{2}$	1
name →	u up	c charm	t top	γ photon
Quarks	4.8 MeV	104 MeV	4.2 GeV	0
	$-\frac{1}{3}$	$-\frac{1}{3}$	$-\frac{1}{3}$	0
	$\frac{1}{2}$	$\frac{1}{2}$	$\frac{1}{2}$	1
	d down	s strange	b bottom	g gluon
Leptons	< 2.2 eV	< 0.17 MeV	< 15.5 MeV	91.2 GeV
	0	0	0	0
	$\frac{1}{2}$	$\frac{1}{2}$	$\frac{1}{2}$	1
	ν_e electron neutrino	ν_μ muon neutrino	ν_τ tau neutrino	Z⁰ weak force
	0.511 MeV	105.7 MeV	1.777 GeV	80.4 GeV
	-1	-1	-1	±1
	$\frac{1}{2}$	$\frac{1}{2}$	$\frac{1}{2}$	1
	e electron	μ muon	τ tau	W[±] weak force

Figure 2.1.: Standard Model of Particle Physics with its 3 generations of quarks and leptons and its force mediating particles, the gauge bosons.

2.2. Quantum Chromodynamics (QCD)

The Standard Model is not just a summary of the particles, it is a relativistic Quantum Field Theory (QFT) joining the electroweak theory and the quantum chromodynamics. The electroweak theory, is the unified description of two interactions, electromagnetism and weak interaction. The weak interaction is the only process in which a quark can change into another quark, or a lepton into another lepton (flavor changes). QCD is the theory that explains the properties of the strong interaction, the fundamental force describing the interaction between quarks and gluons. According to QCD, the quantum number of color behaves like the charge in the electromagnetic interaction, with gluons as carrier that maintain quarks together in hadrons. All bound states of quarks and gluons have to be colorless (or color neutral), therefore they have to be composed of 3 quarks with different colors (baryons), 3 anti-quarks with different anti-colors (anti-baryons) or one quark and one anti-quark carrying color and anti-color (mesons). Gluons are the gauge bosons mediating the strong interaction, but carrying color charge themselves. As such they can interact with each other, which is one of the main differences between the electroweak theory and QCD. Another characteristic difference is the much higher coupling constant in QCD ($\alpha_s \simeq 1$, whereas $\alpha_{em} \simeq \frac{1}{137}$). α_s is much larger and strongly varying as a function of energy and momentum transfer¹. The phenomenological potential between a $q\bar{q}$ pair is given approximately by:

$$V_s = -\frac{4}{3} \frac{\alpha_s}{r} + kr$$

For smaller r the first term dominates, and it is equivalent to a Coulomb like interaction. As r increases the potential becomes stronger, and consequently the energy to take out a quark from a hadron should be infinity. At some point it becomes energetically more favorable to create a new quark-anti-quark pair (a meson) from the vacuum. This behavior at long-distances is called *confinement* and is the reason why single quarks are never observed in nature. The existence of quarks could only be demonstrated by deep inelastic-scattering experiments of electrons on hadrons and in e^+e^- collisions. With these experiments the momentum distribution of quarks in bound hadronic states could be probed. It occurred that for high momentum transfer from the scattering electron to the parton the latter seems to behave as if it was free. From this it was derived that in the other limiting case of the potential, for $r \rightarrow 0$, α_s has to approach zero as well. This was later called the *asymptotic freedom* of QCD at short distances and high energies. In the case ($\alpha_s \rightarrow 0$) QCD can be calculated perturbatively. On the other hand the study of interactions with small momentum transfer (soft processes) needs to be calculated non-perturbatively. This limit can be accessed by Lattice QCD (LQCD), computer based simulations, where the QCD continuum is discretized on a lattice space-coordinate. Within this approach Monte-Carlo calculations can be carried out to estimate the thermodynamic quantities of the system. LQCD predicts that strongly interacting matter undergoes a phase transition at $T = T_c$, the critical temperature, from the hadronic state to a strongly interacting system with high energy density, where quarks and gluons are deconfined. This state is called Quark Gluon Plasma (QGP) and there are strong indications that this state of matter was reached at least at the Relativistic Heavy Ion Collider (RHIC) in heavy ion collisions. But it might have already been produced at top energies in lead-lead collisions at the Super Proton Synchrotron (SPS). A schematic view of the QCD phase diagram of hadronic matter including the QGP can be seen in figure 2.2.

¹Therefore α_s is also called running coupling constant.

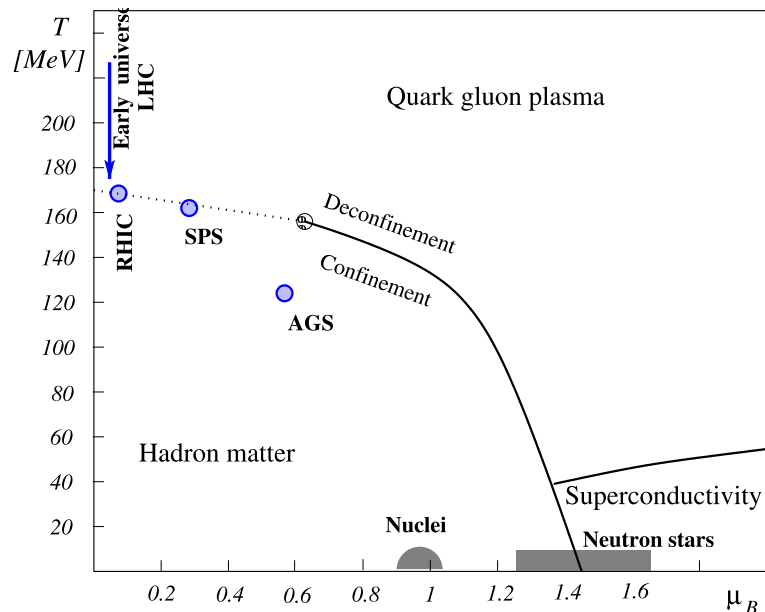


Figure 2.2.: Schematic QCD phase diagram in the $T - \mu_B$ plane. At low T and μ_B nuclear matter shows confinement and hadrons are giving the number of degrees of freedom. On the other hand at higher T a phase transition to a deconfined quark gluon plasma with restored chiral symmetry is predicted by lattice QCD. The phase transition might exhibit a critical point at about $\mu_B \sim 700$ MeV. At higher densities more exotic phases can be reached, e.g. states in very dense neutron stars. In this figure the chemical freeze-out conditions for RHIC, SPS and AGS are indicated as well. LHC will contribute to measurements at low μ_B , but very high temperatures. The blue arrow illustrates how matter is supposed to have evolved after the Big Bang and before chemical freeze-out at LHC [5].

2.3. The Quark Gluon Plasma (QGP)

2.3.1. Quark Gluon Plasma and the Critical Parameters

A Quark Gluon Plasma is expected to have existed approximately 10 picoseconds after the Big Bang, lasting only 10 microseconds. Such conditions are hard to establish in a laboratory.

To investigate a quark gluon plasma one needs to know, how it could be possibly created in a laboratory. Furthermore, for a plasma it is necessary to have a system that consists of a large number of particles. In addition it has to reach local equilibrium, so that variables like pressure, temperature, energy and entropy density can be defined and their relations can be studied. A consequence of these requirements is that the lifetime of the system has to be significantly larger than the inverse rate of interactions, so that at least some interactions occur for each variable, driving the system towards equilibrium [6, 7].

It was observed, that collisions of protons or electrons do not produce enough particles to create a quark gluon plasma. Heavy ion collisions on the other hand seem to be a good candidate for the production of a QGP state, at least if the energy of the colliding nuclei is large enough.

Since 1986 heavy ion collisions can be produced in different laboratories, starting with the Alternating Gradient Synchrotron (AGS) at Brookhaven National Laboratory (BNL) and the Super Proton Synchrotron (SPS) at CERN. These experiments started with rather low energies of $\sqrt{s_{NN}} = 4.6$ and 17.2 GeV per colliding nucleon pair. Although, as one can see in figure 2.2, at least SPS might have already reached an intermediate state between the hadron gas and the quark gluon plasma. Continuing with this research, the Relativistic Heavy-Ion Collider (RHIC) was built at BNL, which reached $\sqrt{s_{NN}} = 200$ GeV per nucleon pair. The results from RHIC already give indications for an established quark gluon plasma. The Large Hadron Collider at CERN will provide energies that are a factor 30 larger than RHIC energies. In these collision the first macroscopic energy will be investigated. The fireball is then expected to contain tens of thousands of gluons and quarks and

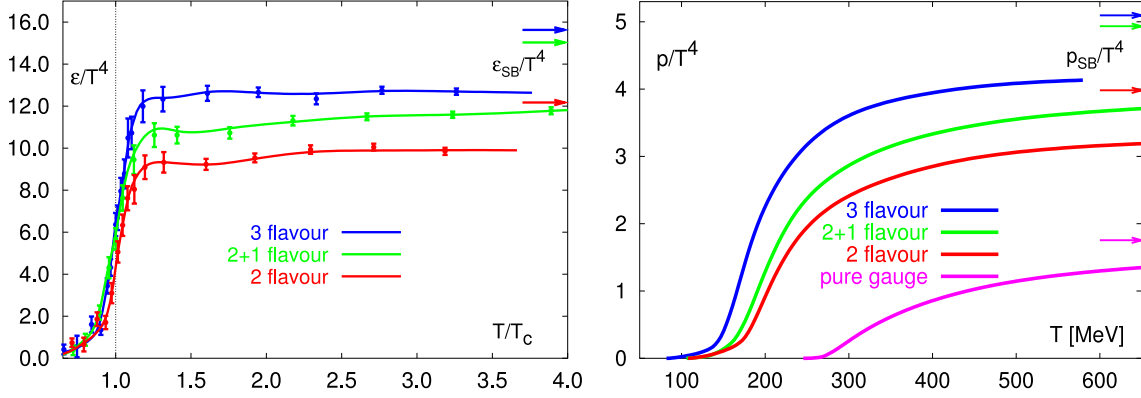


Figure 2.3.: Left: Energy density as a function of the temperature calculated with lattice QCD for different compositions of quark flavors. The critical temperature is around 174 MeV. Right: The pressure in QCD with different number of degrees of freedom as a function of temperature calculated with LQCD. The curves labeled (2 + 1)-flavour corresponds to a calculation with two light and a four times heavier strange quark mass [8].

therefore will exceed the critical temperature for the phase transition several times.

Depending on the number of included quarks LQCD calculations deliver exact results for the critical temperature, the results of one group [8] for the energy density and the pressure including several quarks are shown in figure 2.3. For 2-flavor QCD the expected critical temperature is found to be $T_c = 173 \pm 8$ MeV and in the 3-flavor case it is $T_c = 154 \pm 8$ MeV. Taking two light quarks and one heavier one delivers nearly the same value [9], but it increases slower as in the 3 flavor case. Figure 2.3 shows the pressure and energy density divided by T^4 as a function of temperature in lattice QCD calculations. Both variables rise at T_c . They indicate a significant change of the number of degrees of freedom above T_c , an a possible formation of the QGP.

2.3.2. General Signatures for the Quark Gluon Plasma

The quark gluon plasma can not be observed directly, as it simply vanishes to fast and particle detectors only measure hadronic and leptonic debris from the collisions. But if a quark gluon plasma was created in a collision it will hadronize again after a certain amount of time. In the past 25 years there had been a long discussion what might be signals from this phase transition, a short summary of these signals is given in [5, 6]. As this thesis is dedicated to photon measurements I will concentrate on the signals related to photons in the next section. In the following I will discuss briefly the other signals.

- **Latent heat**

It is possible to measure indirectly the thermodynamical quantity of latent heat. This is normally done by the measurement of all hadron spectra. The slope of the spectra at low transverse momenta can be fitted with a blast wave fit. This function assumes a thermalized spectrum with an effective temperature T_{eff} . Looking at this quantity for kaons as a function of $\sqrt{s_{NN}}$ might offer an inside to the usage of latent heat for freeing additional partonic degrees of freedom.

- **Strangeness enhancement**

Since in our normal hadronic matter strangeness content is negligible, all strange particles occurring in the final state have to be created in the collision. In case of a hadronic gas (HG), particles like kaons and Λ 's have to be produced via the hadronic channels, whereas in a QGP state, the direct creation of $s\bar{s}$ pairs is possible as well. This situation will lead to higher yield for strange particles compared to the hadronic scenario.

- **Charm and beauty suppression or enhancement**

Matsui and Satz argued [10] that the disappearance of quarkonia states e.g. J/ψ is a signal of the QGP. From lattice calculations it can be derived, that the heavy quark potential is effectively screened in the plasma above T_c and therefore $c\bar{c}$ bound states will melt. One would expect them to end up in open charm states instead. However already at RHIC energies charm quarks could be produced with such a high rate, that spontaneous recombination becomes possible if c quarks thermalize in the medium. This would on the contrary to the predicted suppression lead to an enhancement of J/ψ and Υ signals.

- **Jet Quenching**

In the collision fast parton jets can be produced by hard QCD interactions between the nuclei in different stages of the collision. These fast partons have to travel through the hot dense matter surrounding them. If there is a quark gluon plasma the jet will lose energy by interactions with the medium, dominated by induced radiation of gluon bremsstrahlung [11]. This process is called “jet quenching”, it results into a suppression of hadron production at $p_t > 2$ GeV/c. Furthermore the correlated backside jet vanishes, since for the strong energy loss the emission of high p_t hadrons is dominated by surface emission. This can be measured with the suppression factor R_{AA} for hadrons.

$$R_{AA}(p_t) = \frac{\left(\frac{1}{N_{AA}^{evt}}\right) \frac{d^2 N_{AA}}{dp_t dy}}{\frac{\langle N_{coll} \rangle}{\sigma_{pp}^{inel}} \times \frac{d^2 \sigma_{pp}}{dp_t dy}} \quad (2.1)$$

Where the $\langle N_{coll} \rangle / \sigma_{pp}^{inel}$ is the average nucleus thickness, $\langle T_{AA} \rangle$. If heavy ion collisions would only be a superposition of individual nucleon collisions, R_{AA} should be unity for all momenta. But for heavy ion runs at RHIC R_{AA} was roughly 0.3 for π^0 [5]. Therefore it is obvious that heavy ion collisions are more than just a superposition of pp-collisions.

- **Elliptic flow**

The elliptic flow results from the asymmetry in the reaction region in the transverse plane. As the colliding particles are highly Lorentz-contracted the collision is very quick, only lasting roughly 10^{-25} seconds. Depending on the impact-parameter b the geometry of the matter immediately after the collision has an almond-like shape. With the system evolving this highly asymmetrical shape translates into a momentum-space anisotropy. This implies a very asymmetrical particle emission in the plane perpendicular to the axis of the colliding beams. This anisotropy highly depends on the hydrodynamic evolution, the faster the equilibrium is reached the larger the anisotropy will be. The transverse momenta of all emitted particles can be related to the fluid velocity $p_t = m\beta_f\gamma_f$, with m the mass of the particle and β_f and γ_f the relativistic fluid velocity and its Lorentz-factor. From this a characteristic mass-dependent flow pattern arises, resulting in a mass ordering of the anisotropy coefficients ν_2 . With these coefficients the evolution of the fireball can be investigated.

In addition there are some other signals like the modifications of hadronic properties, e.g. for ρ mesons the mass and width will vary through the presence of nuclear matter. Moreover fluctuations in the net charge or baryon number might occur.

2.3.3. Photon signals from heavy ion collisions

The main advantage of photons as probes for the quark gluon plasma is, that if they are produced, they carry the information about the conditions of their production outside of the plasma. Photon production in heavy ion collisions occurs at different stages after the collision. The photons originating from the nucleon-nucleon collision can be separated into 3 categories:

- **Direct Photons** originating from the quark-anti-quark annihilation and the QCD Compton scattering of two incoming partons, which can be seen in figure 2.4 and 2.5.
- **Fragmentation Photons** coming from bremsstrahlung emitted from final state partons.
- **Background Photons** which are produced by decays subsequent to the collision, like $\pi^0 \rightarrow \gamma\gamma$ or $\eta \rightarrow \gamma\gamma$.

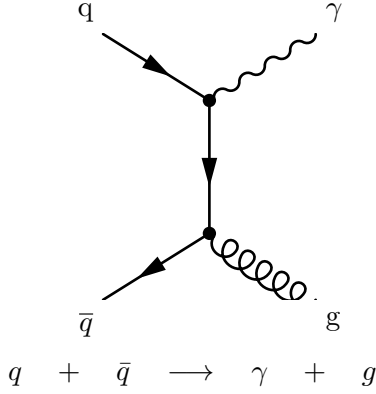


Figure 2.4.: Feynman graph for annihilation of quark and anti-quark.

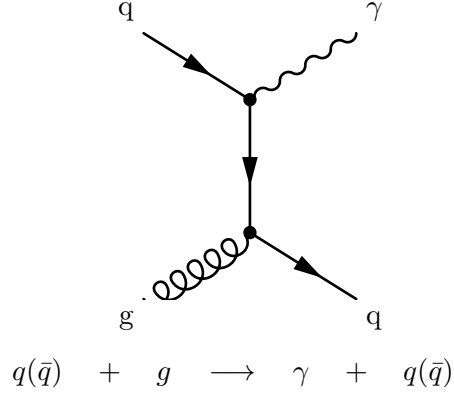


Figure 2.5.: Feynman graph for QCD Compton process.

In some cases direct and fragmentation photons are summarized with the name prompt photons. For nuclei collisions however there are additional sources of photons: the medium contributions which are discussed in detail in [12]. These contributions include:

- **Jet-Photon Conversion**

These photons are produced when a jet crossing the hot medium undergoes annihilation or Compton scattering. Here the p_t distribution is similar to the hard processes. But the jet-photon conversions will be dominated by the gluon-channel (Compton scattering), as the gluon density should be much higher than the quark density in the plasma. Moreover high p_t photons are emitted preferentially early during the QGP phase, when the temperature is at its highest point.

- **Bremsstrahlung Photons**

It is possible that hard partons in the medium produce photons by bremsstrahlung while scattering in the medium. Whereas the rate of the production of these photons is larger than the one from jet-conversions, they normally carry only a fraction of the initial jet energy. Therefore the jet-conversions turned out to dominate over the bremsstrahlung photons if one folds them against the steeply falling jet spectrum.

- **Thermal Photons**

They are emitted from a thermally equilibrated phase. In heavy ion collision they come from the QGP phase and from the hot hadron phase following the QGP. The photon production rate and the photon momentum distribution depend on the momentum distribution of the quarks, antiquarks and gluons in the plasma. Therefore, photons produced in the Quark Gluon Plasma carry information on the thermodynamical state of the medium at the moment of their production.

All these sources and their particular contributions in different transverse momenta are shown in figure 2.6 once for RHIC energies and ones for LHC energies. It can be clearly seen, that at the

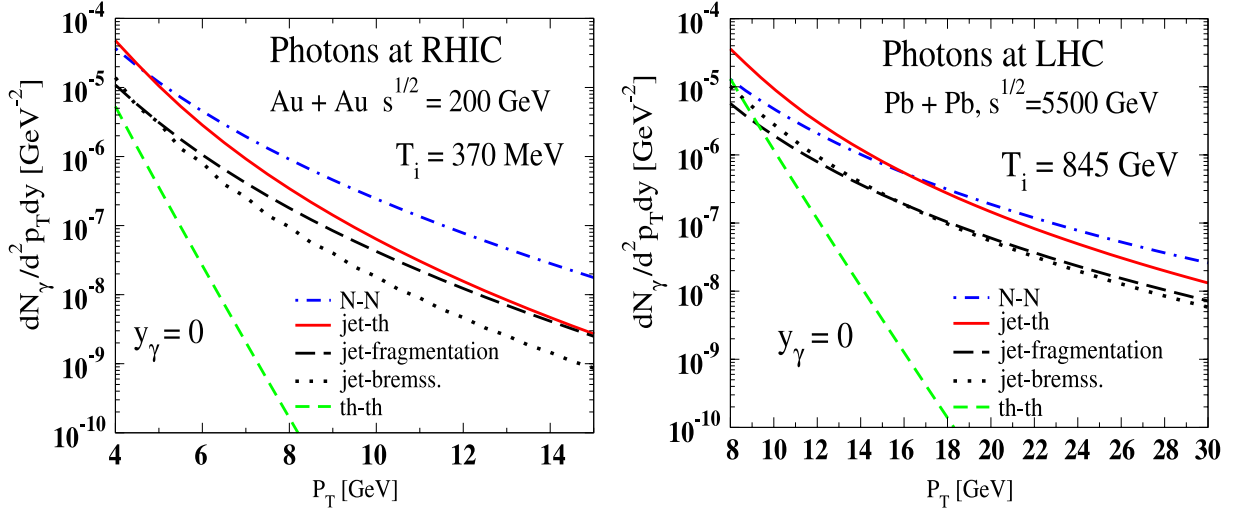


Figure 2.6.: Contribution sources of high p_t photons at midrapidity in central Au-Au collisions at RHIC (left) and for Pb-Pb collisions at LHC (right). The different contributions are (red solid line) Jet-photon conversions in the plasma, (black dotted line) bremsstrahlung from jets in the plasma; (green dashed line) thermal induced production of photons, (black dashed line) fragmentation of jets outside the plasma, (blue dot-dashed line) direct contribution from primordial hard scattering [12].

LHC the jet-photon conversion will dominate the direct photon spectrum for low p_t up to around 16 GeV and afterwards the direct contribution from the primordial hard scattering is dominant. Furthermore, it is shown that at RHIC nearly everywhere (for $p_t > 4$ GeV/c) the hard direct photon component is the leading part. Photon production via jet bremsstrahlung in the plasma turns out to be weak, it is approximately a factor 3 below the jet-photon conversion contribution. As well as thermal induced production is far beyond all other contribution in intensity. However, this contribution is important at low p_t see figure 10 from ref [5].

After having now discussed the different sources of photons the question, why they are so important, still remains. Photons can only interact electromagnetically and therefore will be affected much less by the quark gluon plasma and the following stages of the collision than hadronic probes. That's why especially direct photons can be used as probes for the parton distribution function (PDF) and for measurements of jet quenching. In some cases the other jet arising from the collision will be a hadronic jet losing energy in the medium, whereas the γ -jet will remain unchanged. This might lead to better understanding of the properties of the medium. In addition thermal and jet photons could give a hint about the temperatures in the plasma.

In order to obtain the direct photon spectrum the background from meson decays needs to be subtracted. Actually this is a quite challenging task.

3. Interactions of photons and electrons with matter

This chapter is dedicated to the theory behind the photon conversions and their measurement. Therefore the interactions of photons and electrons (positrons) with matter will be explained (in more detail in [13, 14]).

3.1. Interactions of photons with matter

Photons can be described as electromagnetic radiation with zero mass, zero charge and a velocity that is always c , the speed of light. As they are electrically neutral, they do not steadily lose energy via Coulombic interactions with atomic electrons. Instead they are traveling a considerable distance before undergoing an interaction, they are far more penetrating than charged particles. All interactions of photons with matter lead at least to partial if not total transfer of the photon energy to the electron. Therefore photons either suddenly disappear or scatter by a significant angle with high energy loss. The three mechanisms of photon interactions with matter namely the *photoelectric effect*, *Compton scattering* and *pair production* will be explained in detail in this section. Their relative strength are shown in figure 3.1.

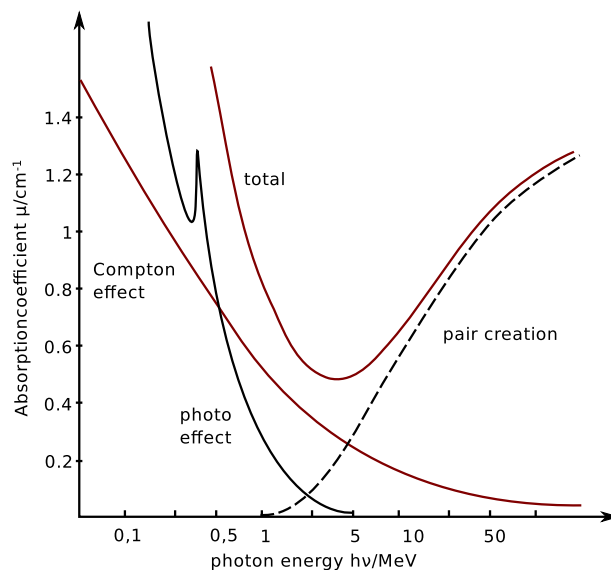


Figure 3.1.: Schematic sketch of the photon absorption coefficient versus energy of the photon. The photoelectric effect dominates roughly up to 0.5 MeV, afterwards the Compton effect becomes more and more important, from 5 MeV on the pair creation is the dominant interaction of photons with matter.

3.1.1. The Photoelectric Effect

In the photoelectric absorption process, a photon undergoes an interaction with an absorber atom in which the photon completely disappears (see figure 3.2, left diagram). In its place an energetic electron is emitted from one of the bound shells of the atom. This interaction is with an atom as

a whole and cannot take place with free electrons, as energy and momentum conservation would be violated in that case. For photons with sufficient energy it is most likely that the electron will originate in the most tightly bound shell of the atom (K shell). Therefore the energy of the electron is given by:

$$E_{e^-} = h\nu - W_A \quad (3.1)$$

where W_A is the binding energy of the electron in its origin shell. This process is dominant at low energies, it is enhanced for absorber materials with high atomic number Z , as the cross section can be expressed as follows:

$$\sigma_{ph} \sim \frac{Z^n}{E_\gamma^n} \quad \text{with } n \text{ varying between 4 and 5} \quad (3.2)$$

The photoelectric effect is most likely to occur if the energy of the incident photon is similar to the binding energy of the electron with which it interacts. Afterwards the quite energetic electron will lose its energy as it will be described in section 3.2.

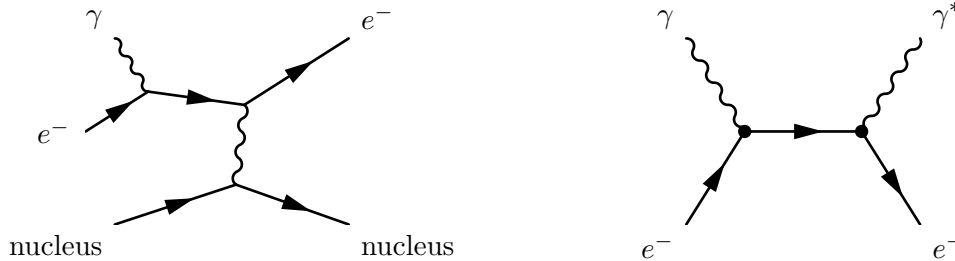


Figure 3.2.: Feynman diagrams for the Photoelectric effect (left) and the Compton scattering (right).

3.1.2. Compton Scattering

The Compton Scattering is the dominant energy loss in the intermediate photon energy region (see figure 3.1). The Feynman graph (figure 3.2 right diagram) shows that the interaction takes place between the incident photon and an electron in the absorbing material. For Compton scattering the incoming γ is deflected through an angle θ with respect to its original direction, transferring a portion of its energy to the Compton electron. As all angles are possible, the transferred energy can vary from 0 to a large fraction of the photon energy:

$$\frac{1}{E_{\gamma^*}} - \frac{1}{E_\gamma} = \frac{1}{m_e c^2} (1 - \cos \theta) \quad (3.3)$$

The probability of Compton scattering per atom of the absorber depends on the number of electron available as scattering targets, therefore it increases linearly with Z . The cross section is therefore approximately proportional to $\frac{Z}{E_\gamma}$.

3.1.3. Pair creation

If an energetic photon enters matter and its energy is higher than 1.02 MeV it may interact with the matter via pair creation, also called photon conversion. In this process a electron positron pair is created from the energy of the incoming photon in the electromagnetic field of a nucleus (figure 3.3). The momentum and energy would not be conserved without the nucleus carrying away a part of the momentum and the energy. As just small fraction of the kinetic energy will be transferred to the nucleus, its state will remain the same and it has a rather passive role. The angle between

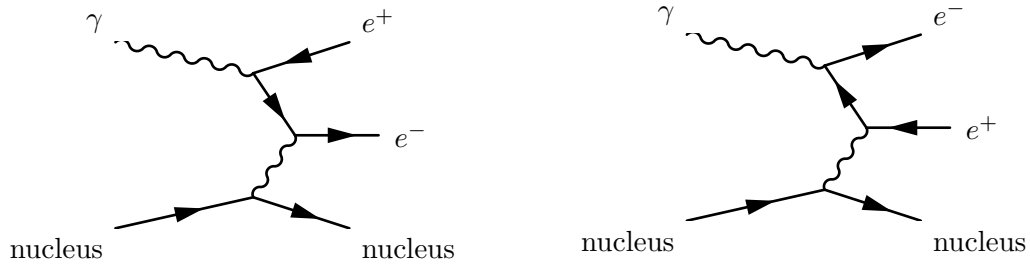


Figure 3.3.: The different Feynman diagrams for pair creation.

the conversion electron and positron for high momentum photons is very small due to momentum conservation.

As with increasing energy the pair creation dominates, an approximation for the differential cross section can be introduced in the complete screening limit, which is valid for high energies. The differential cross section is then given by:

$$\frac{d\sigma}{dx} = \frac{A}{X_0 N_A} \left[1 - \frac{4}{3}x(1-x) \right] \quad (3.4)$$

where A is the atomic number of the material the photon is transversing, N_A the Avogadro constant and X_0 the total radiation length. In addition $x = E/k$ is the fractional energy transfer to the pair-produced electron (or positron), with k the total energy of the incident photon. Taking this into account the cross section has to be symmetric between x and $1-x$, which is shown by the solid line in figure 3.4.

Integrating the formula for differential cross section (equation (3.4)) leads to the high energy limit for the total e^+e^- pair-production cross section:

$$\sigma_{pair} = \frac{7}{9} \frac{A N_A}{X_0} \quad (3.5)$$

The radiation length is the mean distance over which a high energetic electron losses all but $1/e$ of its energy by bremsstrahlung, and $7/9$ of the mean free path for pair production by a high energy

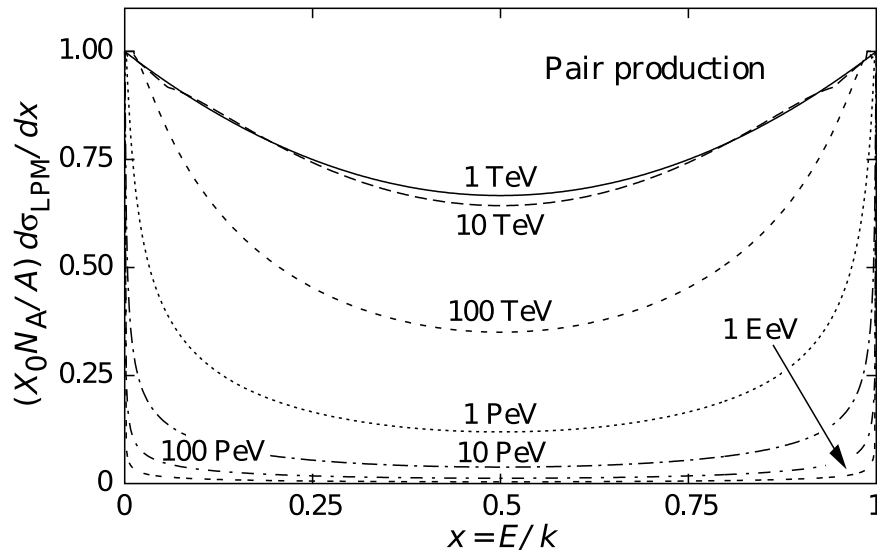


Figure 3.4.: The normalized pair production cross section σ_{LPM}/dx , versus the fractional electron energy $x = E/k$, with k the incident photon energy. From this distribution it is obvious that the momentum transfer to both particles (electrons and positrons) has to be symmetric, but statistically distributed over the fraction of the total energy.

photon. The radiation length can be approximated by:

$$X_0 = \frac{716.4 \text{ g cm}^2 A}{Z(Z+1) \ln 287/\sqrt{Z}} \quad (3.6)$$

where Z is the atomic number and A is the mass number. The radiation length in mixture or compound may be approximated by:

$$\frac{1}{X_0} = \sum_{j=1}^n w_j / X_j \quad (3.7)$$

here w_j and x_j are the fraction by weight and radiation length of the j th element. The probability that a photon converts after traversing a material of thickness x is given by:

$$P_{conv} = 1 - \exp\left(-\frac{7}{9} \frac{x}{X_0}\right) \quad (3.8)$$

Moreover, this probability can be calculated in detector simulations like GEANT by the ratio of the number (#) of converted photons to the number (#) of all photons.:

$$P_{conv} = \frac{\#\text{Converted photons}}{\#\text{All photons}} \quad (3.9)$$

The description of the detector in simulations has to be realistic in terms of geometry, and of the chemical composition of the different materials used, in order to obtain results that are compatible with those of data. The radiation length of the ALICE experiment will be a central point in this analysis, as the photons are reconstructed via the measurement of the electrons and positrons from the conversion.

3.2. Interactions of electrons (positrons) with matter

A charged particle deposits energy if it transverses matter. It can lose energy by *ionization*, which is described by the Bethe-Bloch formula, or by radiative energy losses like *Bremsstrahlung*, *transition radiation* or *Cherenkov radiation*. These processes depend on the particle velocity. Thus, at a given momentum it allows the determination of the particle mass and hence its identity. In this section we will focus on the detection of electrons and positrons, as these are the resulting particles from interactions of photons with matter. The energy loss distributions for different particle species are used in the TPC for identifying and tracking the particles. The minor processes in the energy region of 1 to 10 MeV are scattering and annihilation processes, their Feynman diagrams can be seen in figure 3.5.

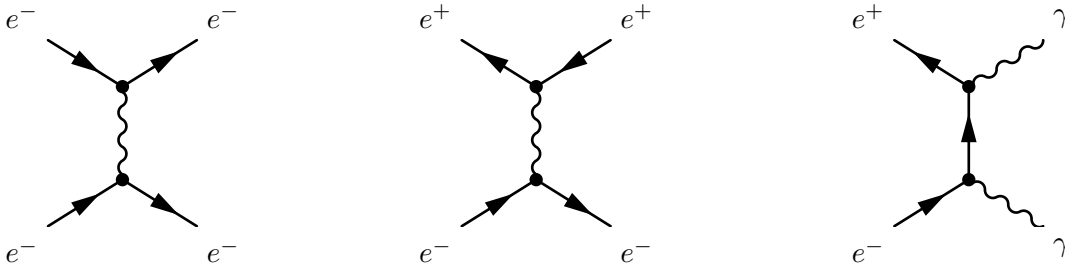


Figure 3.5.: Feynman diagrams for the minor interaction processes of electrons in the region of 1 to 10 MeV: Moller scattering (left), Bhabha scattering (middle) and electron-positron annihilation (right).

3.2.1. Energy Loss by Ionisation

Passing through a medium charged particles lose energy via ionisation or excitation of the constituent atoms. The mean energy loss per path length can be derived from the Rutherford formula for elastic scattering and is described by the *Bethe-Bloch-formula*:

$$-\frac{dE}{dx} = 4\pi N_A r_e^2 m_e c^2 \rho z^2 \frac{Z}{A} \frac{1}{\beta^2} \left[\frac{1}{2} \ln \left(\frac{2m_e c^2 \beta^2 \gamma^2 T_{max}}{I^2} \right) - \beta^2 - \frac{\delta}{2} \right] \quad (3.10)$$

The path length x in the medium is usually given in $[\text{g cm}^{-2}$ or $\text{kg m}^{-2}]$ and corresponds to the amount of matter transversed. In this formula z and v are the charge and the velocity of the transversing particle, β is the relativistic velocity v/c , N_A is the Avogadro number and I is an effective ionization potential of the atom species of the medium (roughly $I = 10Z$ eV). Furthermore Z and A are the atomic mass numbers of the medium atoms. The energy loss drops as described in equation (3.10) with $1/\beta$ for small $\gamma = E/Mc^2 = \sqrt{(1-\beta)^{-1}}$. It reaches a minimum for $E \simeq 3Mc^2$ with M being the mass of the passing particle, afterwards it rises logarithmically with γ . This drop comes from the fact that with increasing velocity the particle has less time to interact with the medium. Whereas the slow rise for high γ originates from relativistic effects, leading to an increase of the transverse electric field of the particle, which enables atoms of the medium that are further away from the particle's path to interact with the particle. This effect saturates into the Fermi plateau, since the polarization of the medium shields the electromagnetic field of the moving particle. For electrons the Bethe-Bloch formula has to be modified, due to the small mass m_e and the maximum energy transfer of $W_{max} = T_{max,e}/2$. This is due to the fact that for electrons after scattering on the atom the incident particle and the ionization electron can not be distinguished anymore. Therefore the energy loss via ionization of a relativistic electron is described by:

$$-\frac{dE}{dx} = 4\pi N_A r_e^2 m_e c^2 z^2 \frac{Z}{A} \frac{1}{\beta^2} \left[\ln \left(\frac{\gamma m_e c^2 \beta \sqrt{\gamma - 1}}{\sqrt{2I}} \right) + F(\gamma) \right] \quad (3.11)$$

3.2.2. Bremsstrahlung

Additionally to ionization losses, electrons lose energy due to radiation of photons while transversing matter (see figure 3.6). This effect arises from the electric field of the atomic nuclei of the medium

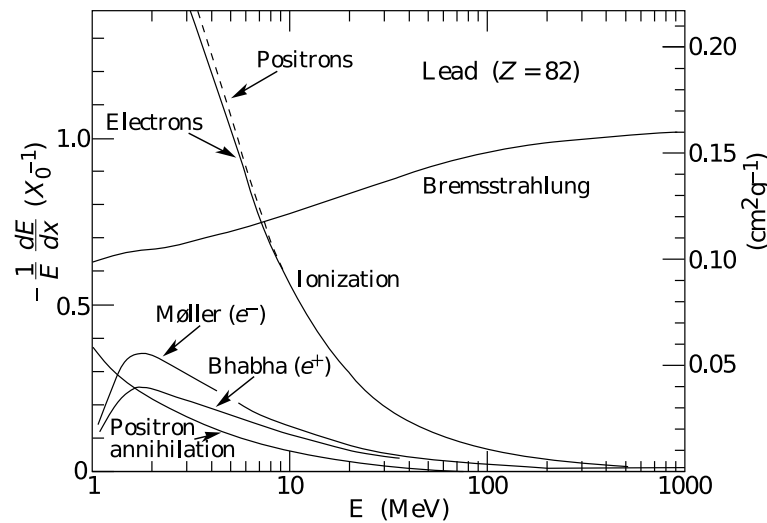


Figure 3.6.: Fractional energy loss per radiation length in lead as a function of electron or positron energy. Electron (positron) scattering is considered ionization when the energy loss per collision is below 0.255 MeV, and as Moller (Bhabha) scattering when it is above. This picture is taken from [13].

decelerating the passing particle, resulting in the emission of a photon. This process is therefore called *Bremsstrahlung*. The average energy loss can be calculated with:

$$-\frac{dE}{dx} = 4\alpha\rho N_A \frac{Z^2}{A} z^2 r_e^2 \left(\frac{m_e}{m}\right)^2 E \ln \frac{183}{Z^{1/3}} = \frac{E}{X_0(m^2/m_e^2)} \quad (3.12)$$

where the variables are the same as used before. The energy loss from Bremsstrahlung drops with the transversing particle mass squared and rises proportionally to its energy, E . Due to the large dependence of the incoming particle mass *Bremsstrahlung* is dominant for electrons at high energies, whereas for heavier particles it plays just a minor role.

In figure 3.6, all contributions to energy loss for electrons are shown. It can be seen that beyond 10 MeV Bremsstrahlung becomes more and more important and from 100 MeV on, there is nearly no other contribution.

3.2.3. Transition and Cherenkov radiation

In addition to these processes two further radiative processes are observed for charged particles. Neither of these processes is important for the energy loss, but can be used for identifying different particle species.

Transition Radiation

The effect of transition radiation is produced by ultra-relativistic particles crossing the boundary surface of two media with different dielectric constants. The electromagnetic field of a charged particle changes with the dielectric constant of the medium by which it is surrounded. Since the electric field is continuous at the boundary the charged particle has to change, therefore radiation is emitted. In contrast to other methods transition radiation is related to $\gamma = \sqrt{(1 - \beta^2)^{-1}}$ and not to β , hence it is a good possibility to identify particles in higher momenta regions. This effect is exploited by the ALICE TRD (see section 4.2.1).

Cherenkov Radiation

Cherenkov radiation is emitted if a charged particle travels through a medium with a higher velocity than the local phase velocity of light in that medium. Then the particle emits photons under the Cherenkov angle:

$$\cos \theta_c = \frac{1}{n\beta} \quad (3.13)$$

where n is the refractive index of the medium. By arranging different media behind each other a particle identification becomes possible in the high p_t region. This technique is used in the ALICE HMPID (see section 4.2.1) to distinguish kaons, pions, protons and electrons.

4. The Experimental Apparatus

4.1. The Large Hadron Collider (LHC)

The Large Hadron Collider (LHC) located at the European Organization for Nuclear Research (Conseil Européen pour la Recherche Nucléaire - CERN) near Geneva, Switzerland, is the most powerful tool for probing the open questions of particle physics in the coming years. It is designed for colliding protons up to a center of mass energy of $\sqrt{s} = 14$ TeV or heavy ions (eg. PbPb) up to an energy of $\sqrt{s_{NN}} = 5.5$ TeV per nucleon-nucleon pair. The LHC should reach design luminosity of $\mathcal{L} = 10^{34} \text{ cm}^{-2}\text{s}^{-1}$ for colliding protons, and of $\mathcal{L} = 10^{27} \text{ cm}^{-2}\text{s}^{-1}$ for heavy ions. Due to these enormous collision energies and luminosities new insights to the structure of matter as well as the

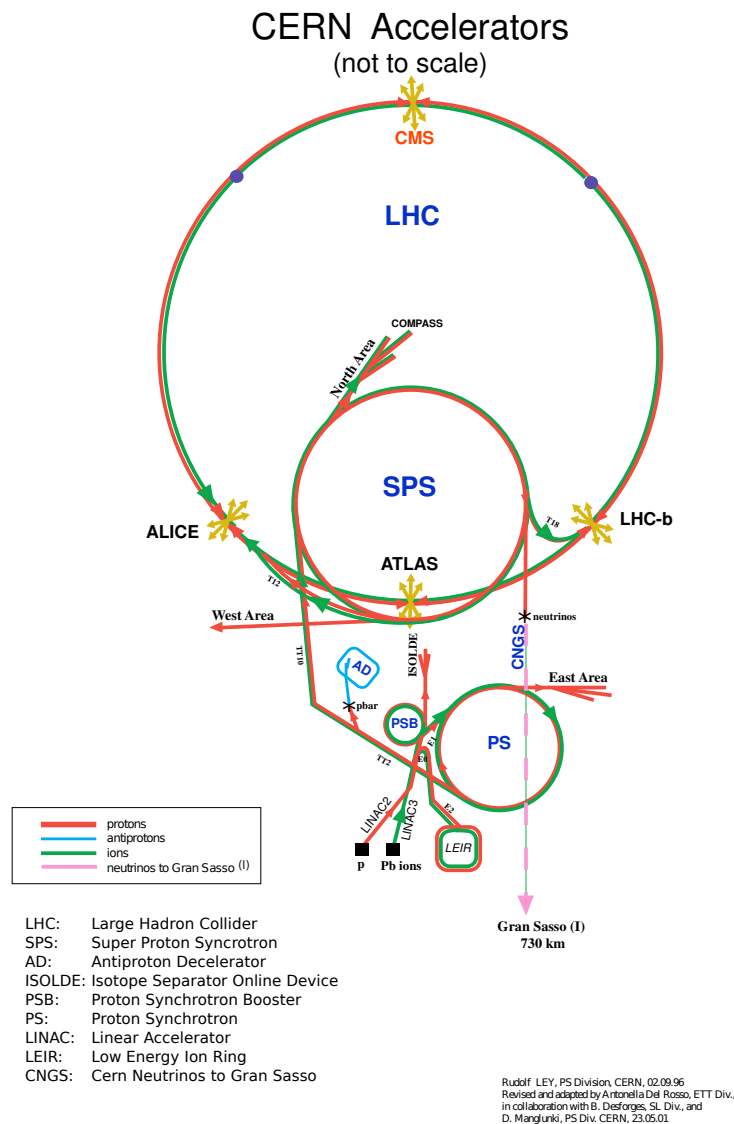


Figure 4.1.: Overview of the CERN accelerator complex [15].

fundamental forces will be possible.

The LHC has been constructed in the existing tunnel of the Large Electron Positron Collider (LEP) which stopped its operation in the year 2000. A schematic overview of the accelerator complex at CERN is shown in figure 4.1. For reaching such high energies it is necessary to do the acceleration in several steps. Therefore for protons at CERN a chain of a linear accelerator (LINAC2), the multi ring Proton Synchrotron Booster (PSB), the Proton Synchrotron (PS) and Super Proton Synchrotron (SPS) is used before injecting the beam, which consists of several bunches of protons, into the LHC, where it is accelerated from 450 GeV to its full energy of 7 TeV. For heavy ions a slightly different set of accelerators is used, namely, the linear accelerator LINAC3, the Low Energy Ion Ring (LEIR) followed by PS and SPS as for protons. To keep the beams on their circles of roughly 4 km radius, 1232 superconducting dipole magnets are installed, which are cooled down to 1.9 K during operation providing a magnetic field of up to 8.3 T. In addition, 392 quadrupole magnets keep the beams focused.

The main LHC experiments are located at 4 of the 8 possible interaction points, as indicated in figure 4.1. Each of this main experiments is optimized for a different set of measurements:

ATLAS

A Toroidal LHC ApparatuS (ATLAS) was designed as a general-purpose detector, therefore it measures the broadest possible range of signals at high transverse momenta. One of the main issues of ATLAS is to search for the Higgs boson or another mechanism giving mass to elementary particles. As well as it might be possible to find indications of new physics beyond the Standard Model such as for super symmetric particles or extra dimensions.

CMS

The Compact Muon Solenoid experiment (CMS) was built to search for the same physics goals as the ATLAS experiment but with complementary detector techniques. Therefore these two experiments can provide corroborating evidence of findings. By now both Collaborations have in addition a physics program for heavy ion collisions.

LHCb

The LHC beauty experiment (LHCb) was built to search for CP-violation in B-meson systems. The results are dedicated to understand the difference between matter and antimatter in the universe.

ALICE

A Large Ion Collider Experiment (ALICE) is the dedicated heavy ion detector at the LHC. The ALICE detector was designed to identify and characterize the Quark Gluon Plasma (QGP). A brief description of ALICE will be given in the next section.

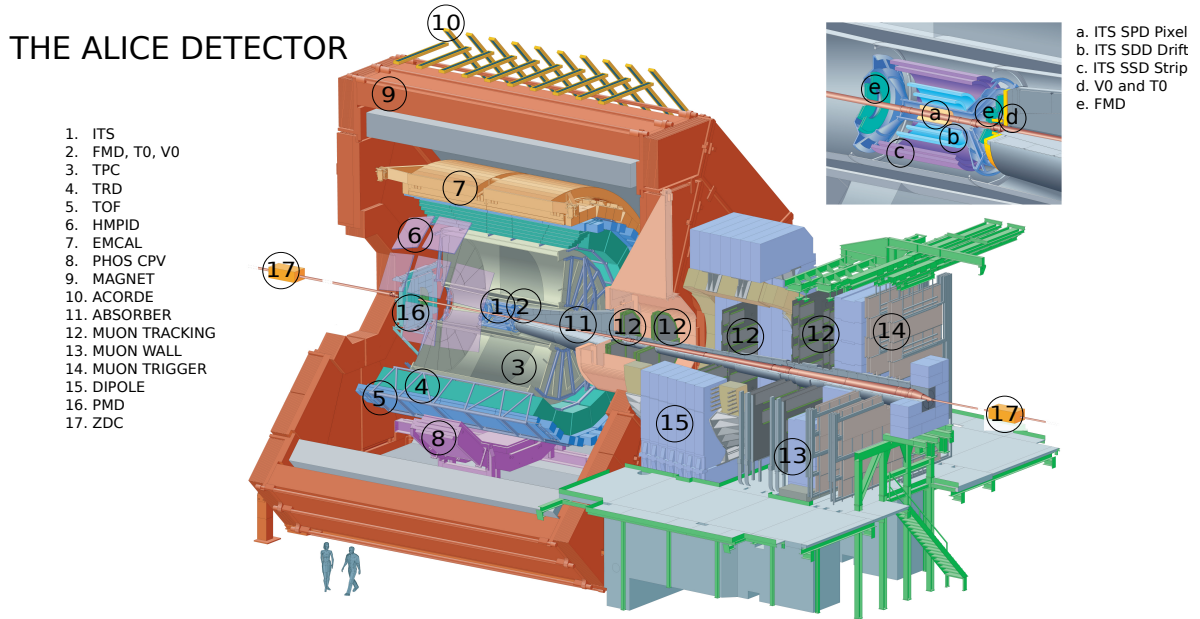


Figure 4.2.: Layout of the ALICE experiment with an insert zooming into the detectors closest to the beam pipe [16].

4.2. A Large Ion Collider Experiment (ALICE)

4.2.1. The Detectors

The ALICE experiment [17] was designed to be capable of identifying and of reconstructing more than ten thousand charged particles over a large transverse momentum range from 100 MeV/c to 100 GeV/c. The experiment is split into two main detector regions the central barrel, measuring hadrons, electrons, positrons and photons, and the muon spectrometer. As this thesis is dedicated to photon physics the muon spectrometer and the cosmic ray detectors will not be discussed any further. A general layout of the detector is shown in figure 4.2.

The central barrel is embedded in a large solenoid magnet reused from the L3 experiment at LEP. From inside out it contains an Inner Tracking System (ITS), a cylindrical Time-Projection Chamber (TPC), three particle identification arrays of Transition Radiation (TRD), Time-Of-Flight (TOF) and Ring Imaging Cherenkov (HMPID) detectors, and two electromagnetic calorimeters the Photon Spectrometer (PHOS) and the Electromagnetic Calorimeter (EMCal). A brief description of the resolution and the detector techniques is given in the following.

Inner Tracking System (ITS)

The ITS [18, 19] was designed to localize the primary vertex of the interaction with a resolution better than 100 μm , to reconstruct secondary vertices coming from the decay of short living particles such as B- and D- mesons and to track and identify particles with a momentum lower than 200 MeV/c. In addition, it can improve the momentum and angular resolution determined by the TPC and it offers the possibility to reconstruct particles in dead areas of the TPC. To keep the distortion of charged particle tracks to a minimum, the total thickness of the ITS was optimized to be 8% of X_0 . It consists of six layers of silicon detectors using 3 different technologies: silicon pixel (SPD), silicon drift (SDD) and silicon double-sided micro-strip (SSD) detectors. The four outer layers have analogue readout, with a dynamic range large enough to provide the dE/dx measurement for low momentum, highly ionizing particles. They are in addition used for particle identification via dE/dx in the non-relativistic ($1/\beta^2$) region. Detailed information about the coverage in η and ϕ , as well as, about the resolution in $r\phi$ and in z are given in table 4.1.

Detector	$\pm\eta$	ϕ	$\sigma_{r\phi}$ [μm]	σ_z [μm]	Specific Resolution
ITS					
SPD 1(2)	± 2 (± 1.4)	$0^\circ < \phi < 360^\circ$	12	100	
SDD	± 0.9	$0^\circ < \phi < 360^\circ$	35	25	
SSD	± 0.97	$0^\circ < \phi < 360^\circ$	20	830	$\sigma_{dE/dx} = 2.0\%$ at low p_t
TPC					
$r \simeq 1.4$ m	± 1.5	$0^\circ < \phi < 360^\circ$	1100	1250	$\sigma_{dE/dx} = 5.0\%$ (for 160 clusters)
$r \simeq 2.8$ m	± 0.9	$0^\circ < \phi < 360^\circ$	800	1100	
TRD	± 0.84	$0^\circ < \phi < 360^\circ$	400	2	$\sigma_p/p = 2.5\% \oplus \frac{0.5\%p}{[\text{GeV}/c]}$
TOF	± 0.9	$0^\circ < \phi < 360^\circ$			$\sigma_t < 70$ [ps]
HMPID	± 0.6	$1.2^\circ < \phi < 58.8^\circ$			
PHOS	± 0.12	$220^\circ < \phi < 320^\circ$			$\sigma_E = 1.12\% \oplus \frac{3.6\%}{\sqrt{E}}$
					$\sigma_{x,y}[\text{mm}] = \sqrt{\left(\frac{3.26}{\sqrt{E[\text{GeV}]}}\right)^2 + 0.44^2}$
EMCal	± 0.7	$80^\circ < \phi < 187^\circ$			$\sigma_E = 1.5\% \oplus \frac{7\%}{\sqrt{E}}$

Table 4.1.: Resolution and detector coverage for the central barrel detectors. [17]

Time Projection Chamber (TPC)

The TPC [20,21] is the main ALICE tracking system, guaranteeing a reliable performance in a multiplicity environment up to 8000 particles per rapidity unit. It provides a momentum measurement for all charged particles and particle identification via specific energy loss dE/dx (see section 3.2.1). A large transverse momentum, p_t , range is covered from low p_t of about 0.1 GeV/c up to 100 GeV/c with good momentum resolution. The TPC is a gaseous detector with a gas mixture of Ne : CO₂ : N₂ (85.7 : 9.5 : 4.8), chosen to reduce space charge and to minimize the electron diffusion. Its active volume goes from 84.8 cm up to 246.6 cm and covers the full azimuthal angle in a pseudo rapidity range of $|\eta| < 0.9$ for full radial track length and $|\eta| < 1.5$ requiring 1/3 of radial track length. For the reconstruction of the 3D-track points the measured drift time (z -direction), with its maximum at $t \sim 80 \mu\text{s}$, and the position on the cathode pads (x -, y -direction) of the induced signal are used.

Transition Radiation Detector (TRD)

Outside of the TPC the TRD [22] is situated, which was designed for tracking and to provide electron identification in the momentum from 1 GeV/c to 100 GeV/c. At the same moment it serves as a trigger for high momentum electrons of above 3 GeV/c. Using the different energy loss of electrons and pions in gases (Xe (85%), CO₂ (15%)), as well as the production of transition radiation (TR) for electrons crossing the border between two different dielectric media (see section 3.2.3), the TRD is capable of separating electrons from the high p_t pion background. A schematic illustration of the signal in the TRD is shown in figure 4.3.

Time-of-Flight Detector (TOF)

The TOF [24] detector will allow pion and kaon identification in a momentum range of 0.5 – 3.0 GeV/c, proton identification for 0.5 – 4.0 GeV/c and electron identification in pp-collisions up to 0.5 GeV/c, by measuring the time a particle needs to fly from the interaction point to the detector. This challenge was overborne by using Multi-gap Resistive Plate Chambers (MRPCs). By choosing this technique a time resolution better than 70 ps was achieved in the test setup. Due to not yet complete calibration this resolution has not been seen in the complete setup so far. The TOF covers as the other inner barrel detectors the full azimuthal angle, but to reduce the amount of material in front of the Photon calorimeter it does not cover the usual rapidity range of $|\eta| < 0.9$ in that area, this fact accounts for TRD as well.

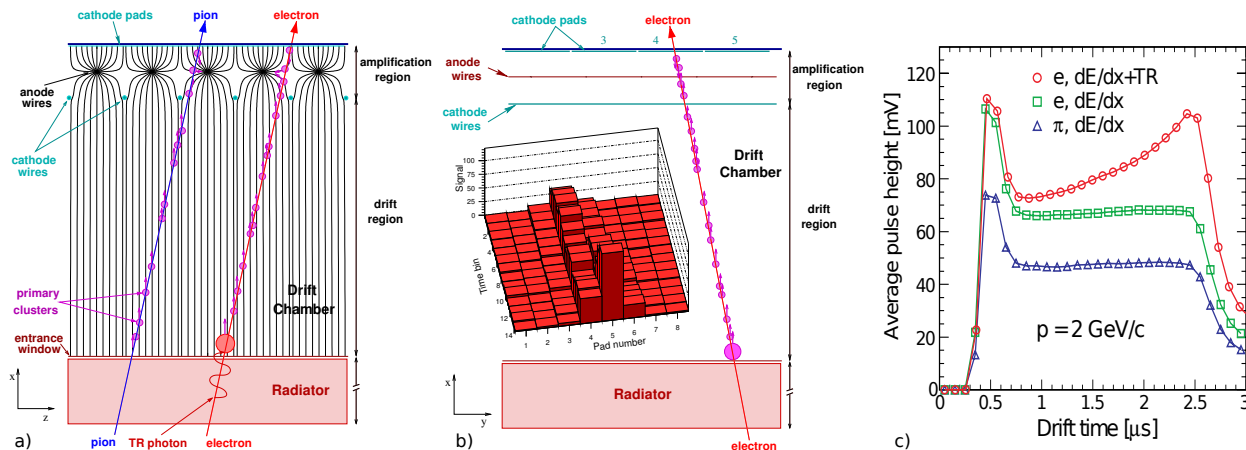


Figure 4.3.: Schematic illustration of the ALICE TRD operational principle. Figure 4.3 a) shows a projection in the plane perpendicular to the wires, whereas figure 4.3 b) is a projection in the bending plane of the ALICE magnetic field, the insert displays the measured electron pulse height distribution over pads and time bins spanning the drift region [22]. The last plot gives the average signal for the 3 typical cases, which can be distinguished in the TRD [23].

High Momentum Particle Identification Detector (HMPID)

The HMPID [25] is dedicated to inclusive measurements of identified hadrons at $p_t > 1$ GeV/c, to enhance the PID capability of ALICE beyond ITS, TPC and TOF measurements. It covers only a small pseudo rapidity area and only reaches from 1.2° to 58.8° in ϕ (see table 4.1). The detector was designed to extend the useful range for π/K and K/p discrimination, on a track-by-track basis, up to 3 GeV and 5 GeV/c. Therefore a Ring Imaging Cherenkov (RICH) detector is used, which consists of 7 modules each equipped with a chamber filled with liquid radiator (C_6F_{14}), readout by a Multi Wire Proportional Chamber (MWPC) filled with CH_4 and pad cathodes covered with a thin CsI film.

Photon Spectrometer (PHOS)

The Photon Spectrometer [26] is designed as a high-resolution electromagnetic spectrometer covering a limited rapidity and azimuthal area (see table 4.1). Being dedicated to photon physics it will try to observe the thermal and dynamical properties of the initial phase of the collision through low p_t direct photons as well as the jet quenching through the measurement of high p_t π^0 and γ -jet correlations. These tasks require fast response as well as a very good position and energy resolution. Therefore lead-tungsten ($PbWO_4$) crystals of $20 X_0$ with a granularity of the order of the Molière radius were chosen as scintillators. In addition a Charged-Particle-Veto detector (CPV) will be installed in front of the crystal area. The required timing resolution is achieved by using fast scintillators and preamplifiers. With this setup a 2 ns time resolution is reached.

Electromagnetic Calorimeter (EMCal)

EMCal [27] was designed in 2008 to enable ALICE to explore in detail the physics of jet quenching over a large kinematic range. It is a large Pb-scintillator (Shashlik) sampling calorimeter with cylindrical geometry located about 4.5 m from the interaction point. But it only covers a small area as seen in table 4.1. The EMCal can provide a fast and efficient trigger for hard jets, photons and electrons. As it can measure the neutral component of the jet as well, in this region a full jet reconstruction is possible. Due to the emphasis on high p_t particles the intrinsic energy resolution is worse than the one of PHOS.

In addition to the already described detectors, there are the forward detectors giving information about centrality, charged particle multiplicity in an η range beyond the central barrel as well as providing fast signals for the trigger. These detectors are (see figure 4.7):

Forward Multiplicity Detector (FMD)

The FMD [17], which is a silicon strip detector, provides charged particle multiplicity information in an pseudo rapidity range from $-3.4 < \eta < -1.7$ and $1.7 < \eta < 5.0$.

T0 Detector

The T0 detector [17] is made of 24 Cherenkov counters in two arrays, placed 73 cm away from the interaction point on the C-side and 375 cm on the A-side. It can provide detailed measurements of the vertex position with the option to give a trigger signal, if they are within a determined window. Therefore the T0 can generate a wake-up signal for the TRD as well as a start time for TOF.

V0 Detector

The V0 detectors [17] are two arrays of scintillation counters covering large pseudo rapidity $-3.7 < \eta < -1.7$ and $2.8 < \eta < 5.1$, generating minimum bias trigger signals for the central barrel detectors. Furthermore, they participate in the measurements of the luminosity in pp-collisions.

Zero Degree Calorimeter (ZDC)

This calorimeter [17] is mainly designed to measure the centrality of heavy ion collisions, it consists of three detectors the ZN for neutrons, the ZP for protons and the ZEM for measuring the energy of particles emitted at forward rapidity $4.8 < \eta < 6.7$.

4.2.2. The Trigger System (TRG)

The ALICE Trigger System [28] hardware consisting of the Level 0 (L0) trigger after $1.2 \mu\text{s}$, the Level 1 (L1) after $6.5 \mu\text{s}$ and the Level 2 (L2) after $88 \mu\text{s}$ is based on the following operational principle: Some of the detector systems (i.e. V0, T0, PHOS, TRD, muon spectrometer, ACCORDE) can give a signal very fast, providing information about a specific measurement (e.g. multiplicity, photons at high- p_t , muon pair). These logical signals are then sent to the Central Trigger Processor (CTP), where they are combined by logical operations inside a FPGA to form different physics triggers (e.g. minimum bias, dilepton, ...). The calculated output signal of the CTP is afterwards sent to the different Local Trigger Units (LTU), typically one for each sub-detector, where they are processed and then according to different detector needs send to the Front-End Electronics (FEE). In the ALICE detector relatively low interaction rates are expected and some detectors are relatively “slow”, therefore some FEE are awaiting a trigger signal after $1.2 \mu\text{s}$, otherwise they will not process the data any further. This signal can be given by the L0, but as some detectors are not able to deliver their signals in that time a second level (L1) is introduced, up to which all trigger signals have reached the CTP. The third step, the L2 decision, waits for the end of the drift time of the TPC. The read-out of the detector electronics into the optical data link is only initiated if a positive L2 signal was received. Additionally ALICE uses a very fast interaction “pretrigger” (derived from the multiplicity arrays V0 and T0), which activates the TRD within $\leq 100 \text{ ns}$ [29]. After having received a L2 accepted the FEE is read out and the data are sent in parallel to the Data Acquisition system (DAQ) and to the High Level Trigger (HLT). The software-based HLT is a farm of up to 1000 multiprocessor computer systems performing an on-line analysis of the events readout. It reduces the data volume being stored, by choosing just a fraction of the data recorded or by compressing the complete event information.

There are several triggers e.g. a minimum bias trigger, a centrality trigger, dielectron and a jet trigger based on the cone algorithm. Furthermore, there will be a γ -jet trigger provided by PHOS, tagging very high momentum photons. As the subject of this thesis is the reconstruction of photons with the conversion method only one specific trigger, the dielectron trigger, will be discussed in detail.

The dielectron trigger

This trigger [28] shall select events with e^+e^- pairs from decays of J/ψ and Υ . Therefore the TRD will trigger on high transverse-momentum tracks and on electron candidates. But this trigger is mainly dominated by the background, which consists of:

- ◆ electrons and positrons coming from gamma conversions after bremsstrahlung, and from secondary interactions,
- ◆ electron-positron decay from Dalitz decays of π^0 , η , vector-meson decays of ρ , ω , ϕ and semileptonic decays of B and D mesons,
- ◆ misidentified pions,
- ◆ fake tracks resulting from combination of clusters from different tracks.

The biggest contributions to the background can be rejected by the HLT, the misidentified pions and the electrons from secondary interactions with wrong momenta, as the TRD assumes that the particle comes from the primary vertex and calculates the transverse-momentum with this assumption. This reduction can be reached by combining the TRD tracklets with TPC and ITS tracking and the usage of the PID rejection power from the TPC dE/dx . At the end, an invariant mass spectrum of the e^+e^- pairs will be calculated and invariant mass windows around J/ψ and Υ will be applied in order to reduce the amount of data stored from this trigger. A photon conversion trigger could have a similar structure as the J/ψ or Υ trigger. But the requirements for the TRD and the HLT would be slightly different as the opening angle between the electrons and positrons is very small, tracks do not originate on the primary vertex, and the mass window is different.

4.2.3. Track and Vertex Reconstruction

Primary Vertex determination

The primary vertex reconstruction [17] is based on information provided by the Silicon Pixel Detectors (SPD). Two pairs of reconstructed points, required to be close in azimuthal and transverse plane, are selected in the 2 layers of the SPD. From their z -coordinates a first estimate of the primary vertex z -position is calculated by linear extrapolation. Afterwards the same procedure is performed in the transverse plane, which can only give a rough estimate according to bending of the track in the transverse plane due to the magnetic field. However, because of the small distance from the interaction point, the x - and y -coordinates can be determined with an adequate precision. With these coordinates a correction of the z -coordinate can be performed. If the beam is well focused one could determine the transverse position by averaging over several events.

The precision of this measurement highly depends on the multiplicity and can reach for low multiplicities in pp-collisions from about $150 \mu\text{m}$ down to $10 \mu\text{m}$ for heavy-ion-collisions. This first calculation is improved after the track reconstruction using the measured track-parameters. Therefore for pp-collisions the transverse resolution can be improved to $70 \mu\text{m}$ and the z resolution down to $110 \mu\text{m}$. Additionally the reconstruction of the primary vertex is performed on the level of the tracking, reaching a very good precision as well.

Track reconstruction

The track reconstruction [17] is done in several steps by finding and fitting the track using Kalman filtering. This method highly depends on the seed values for the track parameters and their covariance matrix. The seeding is done by choosing space points reconstructed by the TPC. These space points are calculated by the center of gravity method in both directions the pad-row as well as the time direction. For higher multiplicities this will be done by cluster unfolding. Additionally the seeding is done twice, once assuming the track originating from the primary vertex and the other time from somewhere else. Then a track is

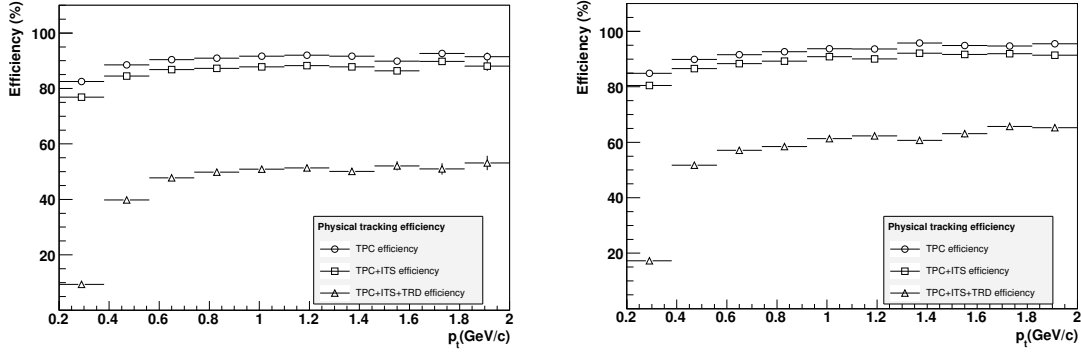


Figure 4.4.: Physical track finding efficiency for different combinations of tracking detectors for central Pb-Pb collisions at $dN_{ch}/d\eta = 6000$ (left) and pp collisions (right) [30].

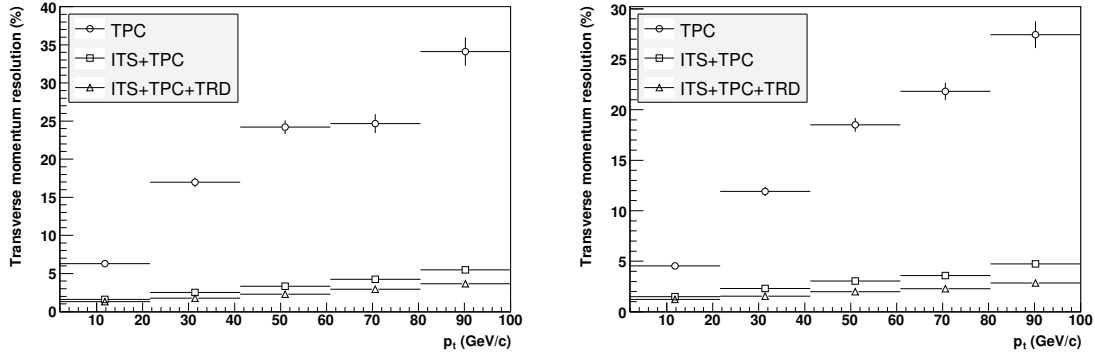


Figure 4.5.: Transverse momentum resolution for different combinations of tracking detectors for central Pb-Pb collisions at $dN_{ch}/d\eta = 6000$ (left) and pp collisions (right) [30].

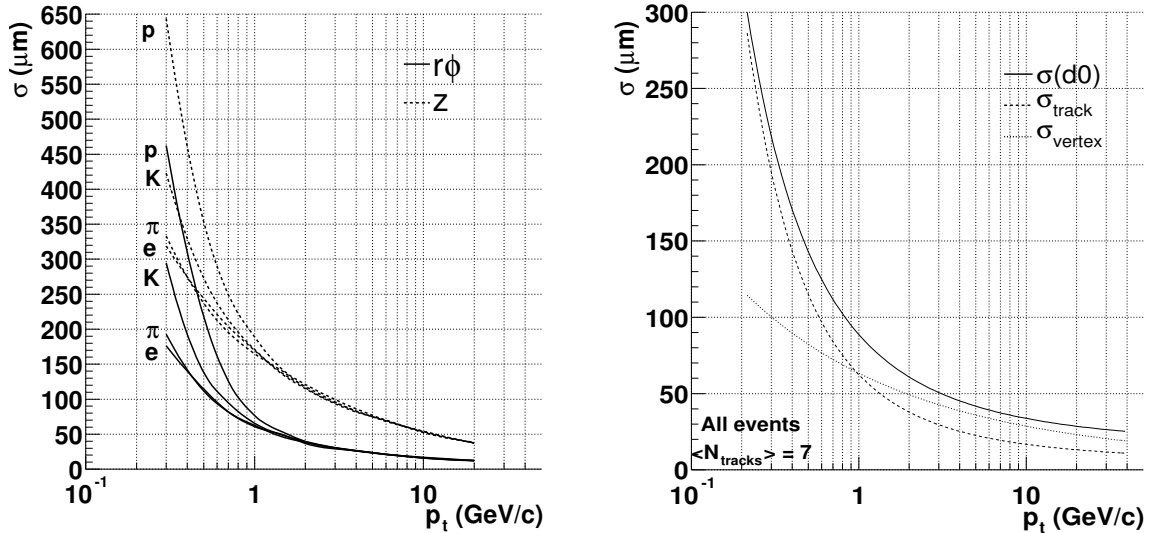


Figure 4.6.: Left: Impact parameter resolution in central Pb-Pb collisions for different particle species as a function of p_t , an assigned cluster in each ITS layer is required. Right: Impact parameter resolution in transverse plane as a function of p_t in pp collisions. The dotted lines display separately the contribution from track extrapolation and the primary vertex accuracy [30].

combined out of matching space points at the outermost pad-rows of the TPC first taking the primary vertex as a constraint. This procedure is repeated several times, each time choosing in addition pad rows closer to the primary vertex. If the track matches any space point this is added to the track and the covariance matrix is recalculated. The tracking is done without assuming the primary vertex as origin again and both parameter sets are kept.

The next step is propagating these tracks (with both parameter sets), starting with the high momentum tracks, to the ITS and then going inwards. As it is possible to assign more than one space point in the ITS with a track coming from the TPC each possibility is calculated separately and then the most probable track is stored after computing the sum of all χ^2 along the track.

Having fitted ITS and TPC together the Kalman filtering is reversed and is going outwards, recalculating the path through the TPC and removing improperly assigned points. Then the tracking follows the track beyond the TPC and assigns space points in the TRD, TOF, HMPID, EMCal and PHOS¹. Finally, a last revision of the Kalman filter is done and the final track parameters are calculated twice, one time assuming the track originating from the primary vertex and the other time without. These parameters are stored in order to allow subsequent studies of short-lived particle decays. The optionally last step is removing all already assigned points from the ITS and fitting the left space points from the ITS again to recover the tracks having went through dead areas of the TPC.

The physical track finding efficiency (see figure 4.4) is larger than 80% for TPC and TPC + ITS, it drops significantly after including the TRD into the fitting, due to additional interactions with the detector material and additional dead regions. On the other hand the p_t resolution improves significantly, as seen in figure 4.5. Therefore the information of the TRD is only used if it improves the resolution. The main performance parameter of such track finding algorithms is the resolution of the impact parameters (distance between the primary vertex and the track prolongation to the point of closest approach to the primary vertex), this depends on both the accuracy in the primary vertex position as well as the track parameters. This resolution was determined with Monte Carlo simulations and the results can be found in figure 4.6.

¹The outer detectors do not contribute to the momentum fit, at the moment in the reconstruction of the data. Once alignment and calibration are finished they will be included again.

4.3. Comparison of ALICE, ATLAS and CMS with respect to the Capability for Photon Measurements

At the LHC three experiments will study both pp and Pb-Pb collisions (ATLAS, CMS and ALICE). As already discussed in section 4.1 only ALICE is dedicated specifically to heavy-ion runs, but all three experiments have a rich physics program for both kinds of runs. In this section a comparison of the photon measurements capabilities of the three experiments is presented.

The ATLAS detector is dedicated to pp collision therefore the main construction issue was full azimuthal coverage over a wide pseudo-rapidity range. Furthermore, ATLAS main feature is calorimetry, composed of several independent longitudinal sampling layers both for electromagnetic as well as hadronic calorimeters. A short summary of the coverage in pseudo-rapidity can be found in figure 4.7 (top). In particular the Liquid Argon electromagnetic calorimeter provides excellent energy and position resolution for electrons and photons. Furthermore, the inner tracking system is equipped with silicon pixel, silicon strips and straw-tube transition radiation trackers being situated in a 2 T solenoidal field.

CMS is also a hermetic detector with a large acceptance for tracking and calorimetry. The tracking system, consisting of silicon pixel and micro-strip tracking detectors, and the calorimeters (electromagnetic and hadronic) are embedded in a 4 T solenoidal field, whereas the muon detectors are situated in the return iron yoke of the magnet. CMS is capable of detecting leptons and both charged and neutral hadrons, as well as photons. A scheme of the coverage in η and ϕ can be found in figure 4.7 (middle).

The ALICE detector is equipped with two calorimeters (discussed in section 4.2.1), in addition photons can be measured via photon conversions in the barrel detectors (see section 3). Therefore photons in a wide transverse momentum range can be observed with ALICE. The momentum resolution at low p_t using the conversion method is much better than that obtained by the calorimeters. On the other hand, calorimeters improve their energy resolution with increasing energy and therefore at some point they will outshine the resolution reached by the conversion method. The momentum resolution of the conversion method is mainly given by the momentum resolution for electrons and positrons (see figure 4.5), by the distance of the conversion from the primary vertex, as well as by the opening angle of the e^+e^- pair. At the moment the ALICE calorimeters only have a small acceptance. In the near future a third calorimeter, the Di-Jet Calorimeter (DCAL), will be installed next to PHOS. It will cover an area of $260^\circ < \phi < 320^\circ$ in ϕ and $0.22 \leq |\eta| < 0.7$ in η as seen in figure 4.7 (bottom). As it consists of the same modules as EMCAL it will have the same resolution. DCAL will enlarge the EMCAL acceptance by 60%.

To demonstrate their direct photon reconstruction capability all three experiments studied their detector response using simulated events. This was done by using different particle generators

Exp	ATLAS		CMS		ALICE		
	LAr Barrel	LArEndCap	ECAL(EB)	ECAL(EE)	PHOS	EMCAL	Barrel
Coverage	$0 < \eta < 1.4$	$1.4 < \eta < 3.2$	$0 < \eta < 1.5$	$1.5 < \eta < 3.$	$0 < \eta < 0.12$	$0 < \eta < 0.7$	$(0 < \eta < 0.9$
	2π	2π	2π	2π	0.6π	0.6π	$2\pi) \cdot 7X/X_0$
Granularity	0.003×0.100	0.025×0.100	0.017×0.017	0.017×0.017	0.004×0.004	0.014×0.014	$3 \cdot 10^{-4} \times$
$\Delta\eta \times \Delta\phi$	0.025×0.025	0.025×0.025		to			$2 \cdot 10^{-4}$
	0.025×0.025	0.025×0.025		0.05×0.05			resolution
Resolution	$10 \%/ \sqrt{E} \oplus$	$10 \%/ \sqrt{E} \oplus$	$2.7 \%/ \sqrt{E} \oplus$	$5.7 \%/ \sqrt{E} \oplus$	$\frac{3.6\%}{\sqrt{E}} \oplus$	$7 \%/ \sqrt{E} \oplus$	2% low pt
	0.5 %	0.5 %	0.55 %	0.55 %	1.12%	1.5 %	5 % high pt

Table 4.2.: Compilation of the different photon detectors in the three LHC experiments, including a brief description of their characteristics and resolutions [31].

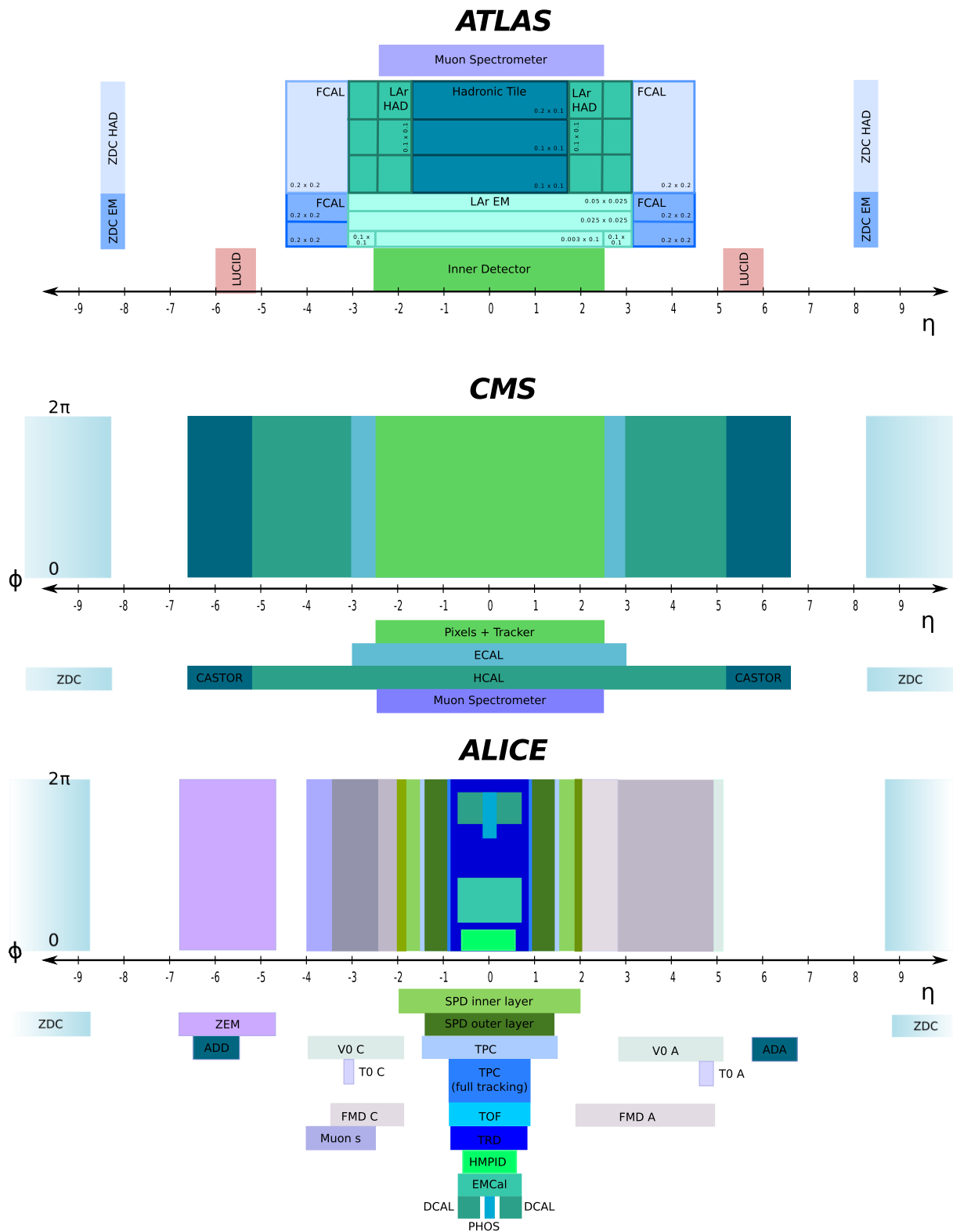


Figure 4.7.: Pseudo-rapidity and azimuthal coverage of the different detector systems ATLAS (top), CMS (middle) and ALICE (bottom).

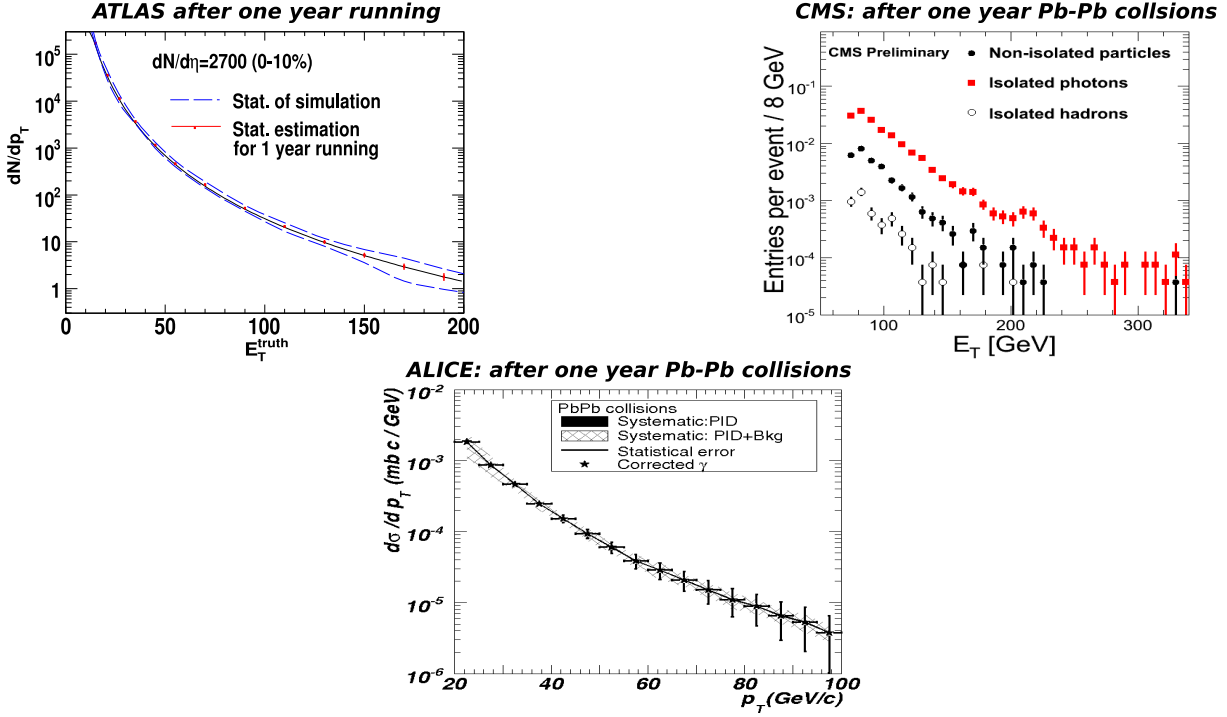


Figure 4.8.: Isolated photon spectrum that can be measured by ATLAS after one year running (upper left), by CMS in one year Pb-Pb collisions (upper right) and by ALICE with 2 PHOS modules in pp - collisions at 14 TeV (lower middle) [31], references there in.

for the jets to trigger on γ (γ -jet events) or π^0 (jet-jet events) and the underlying events in the simulation. Whereas ALICE and ATLAS were using γ -jet events from PYTHIA and heavy-ion events from HIJING, CMS was using PYQUEN and PYTHIA for the γ -jet events and HYDJET for the heavy-ion events. The results obtained from these simulations can be seen in figure 4.8. The spectra show clearly that all 3 detectors are compatible for lower momenta, for higher momenta CMS and ATLAS outreach ALICE due to their wider acceptance. On the other hand ALICE can provide a very precise low transverse momentum measurement with the conversion method, which is a challenge for the ATLAS and CMS experiments due to their much higher conversion probability (ALICE $\sim 7\%$, ATLAS $\sim 20\%$ and CMS $\sim 30\%$). This method will be discussed in detail in the following chapters.

5. Measurement of Photon Conversions in ALICE

In this chapter the measurement of the photons having converted in the detector material will be discussed in detail. Therefore, the V0 reconstruction method and the recalculation of the conversion point will be explained at first. Secondly, the data which was investigated will be discussed in detail. Afterwards, the method to reduce the background will be explained. Finally, the analysis of the resulting photon sample the photon characteristics will be presented.

5.1. The V0 reconstruction method

As already mentioned in section 4.2 the ALICE detector measures high energetic collisions of protons and in the near future heavy ions collisions. The photon signals of interest (discussed in 2.3.3) have large energies, therefore photons will in general interact with the material via pair creation. These photon conversions can be reconstructed through the tracking of the conversion products. As the tracking starts in the TPC, only conversions that happen up to the middle of the TPC can be reconstructed.

On the reconstruction level vertices from different decay particles are searched for, although γ conversions are not decays, they can be treated as such due to the two opposite charged tracks coming from one secondary vertex. The reconstruction of the V0 (unknown particle) choses tracks with a large impact parameter, which are assumed to be secondary tracks. Afterwards, opposite-sign tracks are combined and the distance of closest approach (DCA) is calculated. If the distance is below some predefined value and in addition the point of closest approach is located before any measured points of these tracks, the track pair is retained as a candidate for a secondary decay vertex. From the decay particles the invariant mass is calculated, by which a suggestion of the particle identity can be given for the further analysis. The particles that can be reconstructed using the V0 method are K_s^0 , Λ , $\bar{\Lambda}$ and γ conversions. For photon conversions, obviously, only

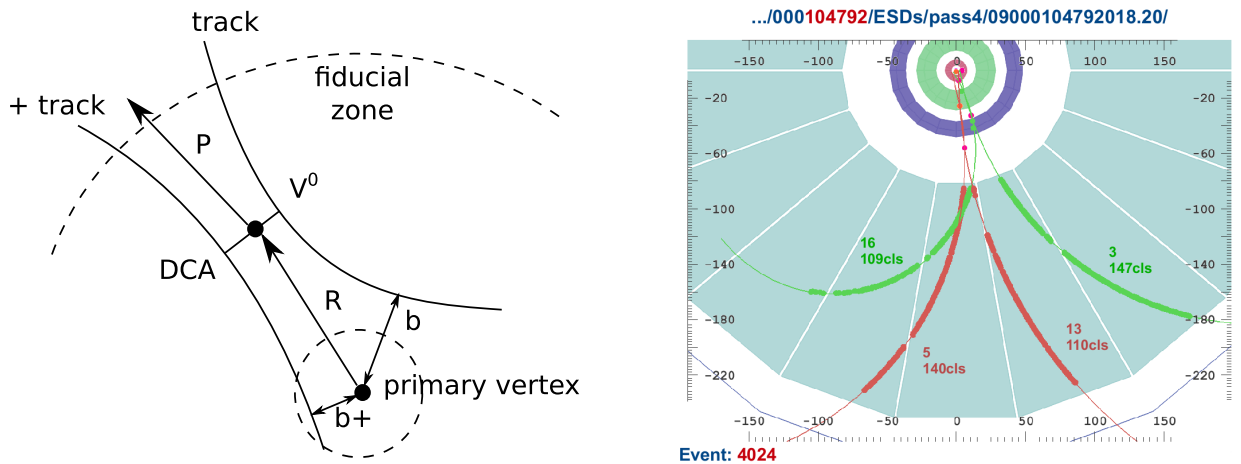


Figure 5.1.: Sketch of the reconstruction of a generic secondary vertex (left) and a reconstructed event from the 2009 data taking campaign (right) showing a π^0 meson candidate from 2 reconstructed photon conversions using the V0 method.

electrons and positrons candidates originating from a photon are chosen for the analysis. In figure 5.1, the general VO reconstruction method as well as a reconstructed γ conversion can be seen. Furthermore, there are 2 photons pointing to the primary vertex with an invariant mass compatible with a π^0 meson.

5.2. Reconstruction of the Conversion Point

Due to the fact that the secondary vertex finding for photons gives just a rough estimate of the photon conversion point, we need to recalculate the position of the secondary vertex [32]. For gamma conversions one additional condition can be defined, that the momenta of the electron and positron at the conversion point have to be parallel, because the photon has no mass which enters in the opening angle. Therefore, it is possible to use the helix of the track, which is given by the first track point (x_{TR}, y_{TR}, z_{TR}) , the momentum components at this track position and the sign of the track. An illustration of the steps of the calculation and their variables is given in figure 5.2. First of all we have to calculate the helix center (x_c, y_c) of the electron and positron tracks from the photon candidate in the xy-plane (figure 5.2 a)):

$$x_c = \pm r_h \text{sign}(B) \cos \phi' \quad \text{and} \quad y_c = \pm r_h \text{sign}(B) \sin \phi' \quad (5.1)$$

Here r_h is the radius of the helix of either the positive or the negative track. It is calculated using the magnetic field, the transverse momentum and the angle ϕ between the transverse momentum direction and the horizontal. To compute this points in addition ϕ' has to be calculated, which is $\phi - \frac{\pi}{2}$. The negative (positive) sign is used if the track is positive (negative). With this information the reconstructed conversion point is found by weighting the helix centers with the two radii in the following way.

$$x_{conv} = \frac{x_{c,pos} \cdot r_{h,neg} + x_{c,neg} \cdot r_{h,pos}}{r_{h,neg} + r_{h,pos}} \quad (5.2)$$

$$y_{conv} = \frac{y_{c,pos} \cdot r_{h,neg} + y_{c,neg} \cdot r_{h,pos}}{r_{h,neg} + r_{h,pos}} \quad (5.3)$$

Where $x_{c,pos(neg)}$ and $y_{c,pos(neg)}$ are the x and y - coordinate of the helix center of the positive (negative) track and $r_{h,pos(neg)}$ is the radius of the helix in the xy -plane. Afterwards, the z -coordinate needs to be recalculated. Therefore, for each track we have to find the points on its helix $(x_{v,pos(neg)}, y_{v,pos(neg)})$, where the line going through the center and the conversion point crosses the helix. This is done as follows and the visualization can be seen in figure 5.2 c).

$$\alpha = \text{atan2}((y_{conv} - y_c), (x_{conv} - x_c)) \quad (5.4)$$

$$x_v = x_c + r_h \cos \alpha \quad (5.5)$$

$$y_v = y_c + r_h \sin \alpha \quad (5.6)$$

For the calculation the of the angle the function atan2 is used, this enlarges the arctan to the range from $-\pi$ to π and is defined as follows:

$$\text{atan2}(y, x) = \begin{cases} \arctan \frac{y}{x} & x > 0 \\ \arctan \frac{y}{x} + \pi & x < 0, y \geq 0 \\ \arctan \frac{y}{x} - \pi & x < 0, y < 0 \\ +\frac{\pi}{2} & x = 0, y > 0 \\ -\frac{\pi}{2} & x = 0, y < 0 \\ 0 & x = 0, y = 0 \end{cases} \quad (5.7)$$

Then the length of the helix trajectory needs to be calculated from (x_{TR}, y_{TR}) to (x_v, y_v) , the sketch of this can be seen in figure 5.2 d), as well as the recalculation of the z -coordinate needs to be done afterwards. One needs to calculate the angle between the two radii from the helix center to (x_{TR}, y_{TR}) and (x_v, y_v) first:

$$\beta = 2 \operatorname{atan2} \left(\frac{d}{2}, r \right) \quad (5.8)$$

$$\text{with} \quad d = \sqrt{(x_v - x_{TR})^2 + (y_v - y_{TR})^2} \quad (5.9)$$

$$\text{and} \quad r = \sqrt{r_h^2 + \frac{d^2}{4}} \quad (5.10)$$

The crossing point (x_v, y_v) then needs to be translated into the 3 dimensional space, which can be achieved by using the dip-angle λ_{dip} and the length of the trajectory:

$$z_v = z_{TR} + U \cdot \tan \lambda_{dip} \quad (5.11)$$

Finally the z -coordinate of the conversion has to be calculated, which is done with the weighting method which was already used for the x and y coordinate.

$$z_{conv} = \frac{z_{v,pos} \cdot r_{h,neg} + z_{v,neg} \cdot r_{h,pos}}{r_{h,neg} + r_{h,pos}} \quad (5.12)$$

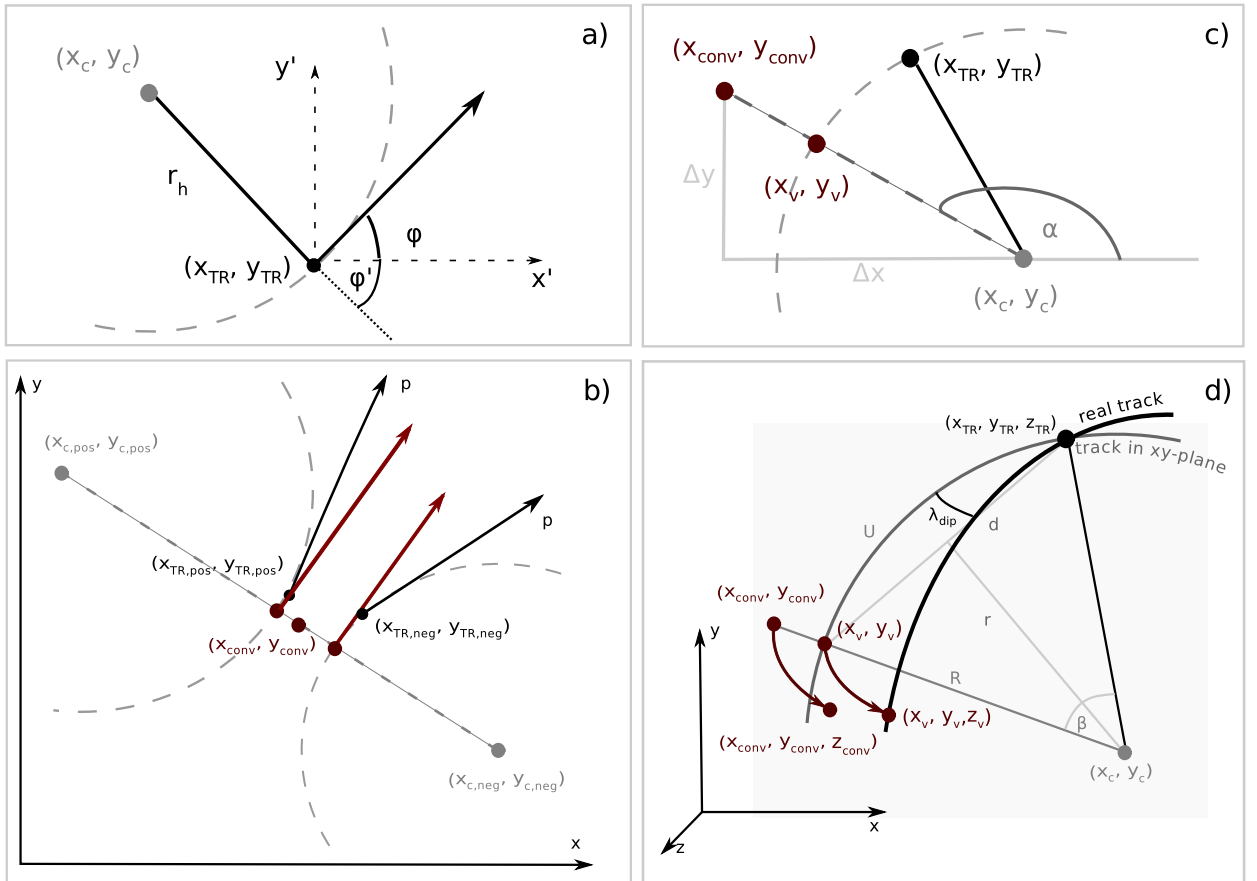


Figure 5.2.: Illustration of the recalculation of the conversion point $(x_{conv}, y_{conv}, z_{conv})$. Beginning with an explanation of the track coordinates (figure 5.2 a)), this figure explains how the conversion point is first reconstructed in the xy -plane (figure 5.2 b)) and then afterwards the z -coordinate is recalculated (figure 5.2 c) and d)). The black points are the given track points with their corresponding momentum vector, the gray points are the helix centers and the red points are the recalculated conversion point and the corresponding points on the helices.

Unfortunately, this method can only be used for γ conversions, as the momenta in the conversion point have to be parallel. With this method we improved our resolution in r , z , x and y . This will be discussed in detail in chapter 7.

5.3. Data set, event selection and Monte Carlo simulations

The analysis was done for pp collisions at 900 GeV from the ALICE data taking in December 2009 and March 2010 as well as for pp collisions at 7 TeV obtained in the ALICE data taking from March to June of the year 2010. For the 900 GeV data we analyzed roughly $3.9 \cdot 10^6$ events. The 7 TeV data sample already exceeds 10^8 events. The data are divided into two samples (see table 5.1). The main emphasis will lie on the studies of the 7 TeV data sample 2.

Furthermore several Monte Carlo simulations were used for this analysis, they are summarized in table 5.2. The iteration tags (ite 0, ite 1, ite 2, ite 3) give the iteration of the material budget, these tags will be used in the studies to characterize the Monte Carlo productions. Monte Carlo ite 1 should be compared to data sample 1 and ite 2 to data sample 2.

The analyses were carried out using the software of the Photon Conversion Group [33] of the ALICE Collaboration, which introduced their own analysis task in AliRoot [34]. Furthermore several scripts and macros were developed for the analysis of the mapping, the photon characteristics, the cut studies, the resolution studies and the systematic error calculation, these are available at [33, 34].

Before the analysis could be carried out a check of the data was needed. Therefore each run needed to be investigated separately, whether the reconstruction was done properly. For the complete 900 GeV data this was done for this thesis as well as for all events of the 7 TeV data.

To be able to compare data and Monte Carlo simulations, having different statistics and different properties, like the multiplicity distributions (see figure 5.3), a method for the absolute normalization and for the event selection needs to be defined. For the analysis presented in this thesis the following method to compare data and Monte Carlo was used:

- The analyzed events have to have passed the Physics Selection task of ALICE.
- Only events where the number of contributors to the vertex is at least 1 are counted for the analysis (N_{ev}^{Vtx}). Afterwards, the distributions are normalized to the N_{ev}^{Vtx} .

Data set	Run number	MonALIsa name	N_{events}	AliRoot version	Triggerrate
1	114918 - 118903	LHC10b, LHC10c	$30 \cdot 10^6$	v4-18-Rev-10 /-14	$\sim < 400$ Hz
2	119837 - 120820	LHC10c	$100 \cdot 10^6$	v4-18-Rev-15 /16	$\sim > 500$ Hz

Table 5.1.: Data sets which were taken for the analyses with their different properties.

MonALIsa name	Particle Generator	Energy $\sqrt{s_{NN}}$	N_{events}	AliRoot version	Iteration #
LHC09d10	Pythia Tune D6T	2×450 GeV	5.302.800	v4-17-Rev-23	ite 0
LHC10b1	Phojet	2×3.5 TeV	4.057.800	v4-18-Rev-10	ite 1
LHC10b2	Pythia Perugia 0	2×3.5 TeV	3.402.600	v4-18-Rev-10	ite 1
GSI local	Pythia Perugia 0	2×3.5 TeV	3.000.200	v4-18-Rev-19	ite 2
–	Pythia Perugia 0	2×3.5 TeV		v4-18-Rev-21	ite 3

Table 5.2.: Monte Carlo events used for the analysis with the particle generators used and the number of events produced, as well as the AliRoot version. The Iteration tag gives the changes of the material and will be used from now on to classify the Monte Carlo productions used. The last iteration including the latest material changes was not yet carried out.

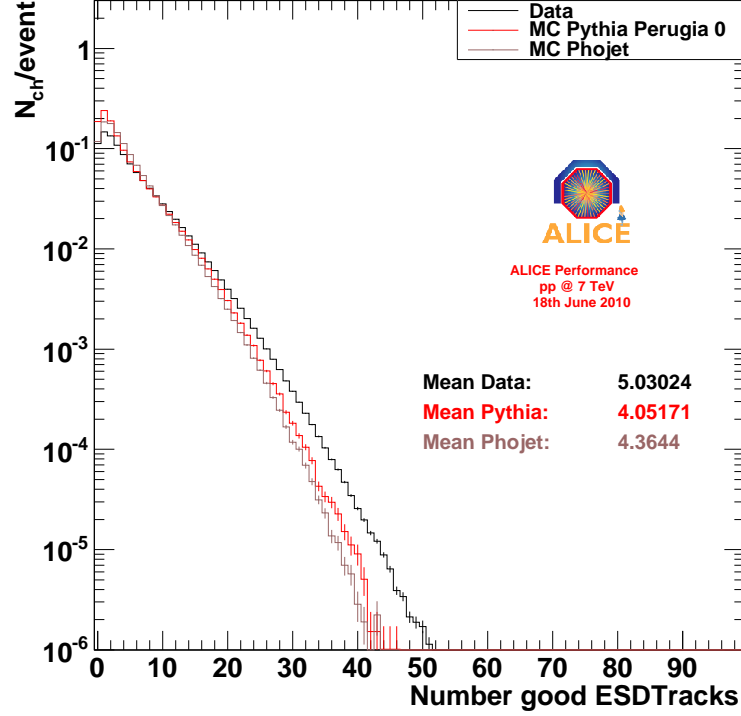


Figure 5.3.: Multiplicity distributions for data and the different particle generator Pythia and Phojet, the means are slightly different. This distributions was obtained using only the tracks which have at least 1 Contributor to the vertex.

- The number of good ESD tracks which passed the Physics Selection task and have at least 1 contributor to the vertex is measured and from this distribution the mean $\langle N_{ch} \rangle$ is calculated.

Up to now the same procedure was done for simulation and data, but for the simulation an additional step has to be performed:

- The Monte Carlo has to be scaled by the factor $\frac{\langle N_{ch,data} \rangle}{\langle N_{ch,MC} \rangle}$ to make it comparable to the data.

Afterwards both distributions are plotted together without any additional scaling and they can be compared.

5.4. Sample of photons

Having now clarified how the comparison between data and Monte Carlo is done, we have to understand where the photons we are measuring originate from and which other factors like reconstruction efficiency and conversion probability enter in our calculations. The number of observed photons is given by

$$N_{\gamma}^{observed} = N_{\gamma}^{produced} \cdot P_{conv} \cdot \epsilon_{\gamma}^{reconstruction} \quad (5.13)$$

$$\text{with} \quad N_{\gamma}^{produced} = N_{\gamma}^{\pi^0} + N_{\gamma}^{\eta} + N_{\gamma}^{\omega} + N_{\gamma}^{\eta'} + N_{\gamma}^{\phi} + N_{\gamma}^{direct} \quad (5.14)$$

As the photon reconstruction efficiency (figure 5.4, left plot) enters in the $N_{\gamma}^{observed}$, we have to be sure that it is as close as possible in data and in Monte Carlo. In our analysis we can not distinguish between the reconstruction efficiency and discrepancies on the material. Additionally, we can calculate the conversion probability using the Monte Carlo as described in equation (3.9). Therefore, we have to apply several conditions to select *all photons* in the Monte Carlo simulation:

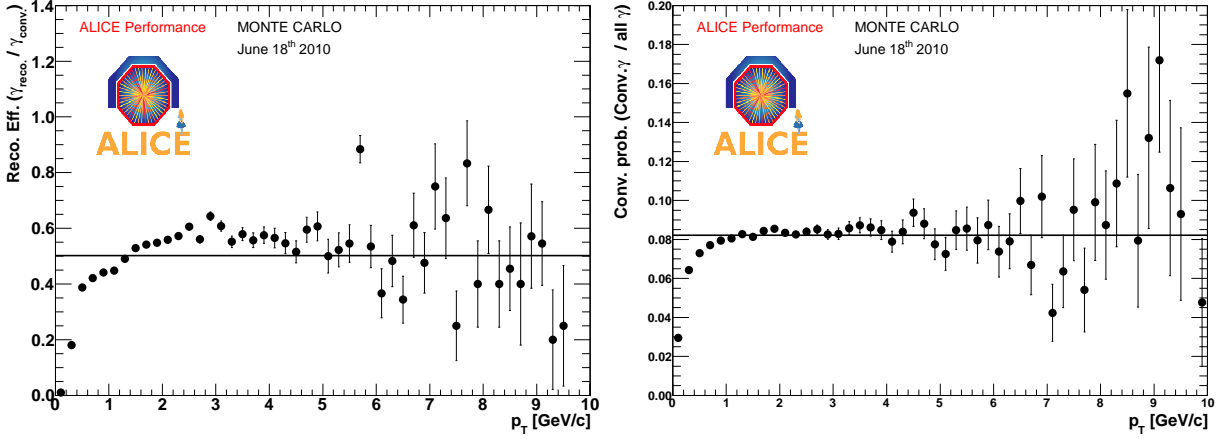


Figure 5.4.: Reconstruction efficiency (left) and conversion probability (right) for the cuts used for the material studies obtained with the Monte Carlo production carried out at GSI.

- An $|\eta|$ cut is used, either $|\eta| < 0.9$ for the fiducial region or $|\eta| < 1.4$ for the extended pseudo rapidity range.
- A maximum for the R coordinate is requested, which is usually 180 cm, as we need a part of the TPC to reconstruct the tracks properly.
- The photon should be a primary particle or have a mother that is a primary particle different from a photon. This condition will select photons from π^0 , η , η' , ω , ϕ and direct photons. Other mothers are seen as well with masses of 0 GeV/ c^2 and 0.9404 GeV/ c^2 , this issue is still under investigation.

Additionally some conditions have to be applied to the *converted photons* as well:

- The photon should have at least 2 daughters, one electron (PDG code -11) and a positron (PDG code 11). It might be, that GEANT stores more than two daughters for a conversion.
- The unique ID of the process should be 5, which corresponds to the photon conversion process in GEANT.
- The e^\pm should be within the η cut.
- The conversion point should be within the maximum of $R_{conv} < 180$ cm and $|Z_{conv}| < 200$ cm.
- The conversion point should fulfill the condition $(Z_{conv} \cdot ZR_{slope} - Z_0) > R_{conv}$ where ZR_{slope} depends on the η cut and Z_0 depends on the beam spread in Z . This condition is the line cut mentioned in section 5.5.

Following these steps the conversion probability, shown in figure 5.4 (right), is obtained. This gives a conversion probability of about 8% for an η cut of $|\eta| < 0.9$ (fiducial region), which corresponds to a radiation length of 10.7%. Assuming now, that the reconstruction efficiency is quite well known and the same for data and Monte Carlo, we can provide a check of the material budget and its current implementation in the GEANT simulations. For this analysis around 10^7 photons from pp collisions at 7 TeV delivered by the LHC during spring 2010 were reconstructed and taken into account for the test of the simulations.

5.5. Creating pure photon samples

In order to estimate the ALICE material budget it is essential to create a clean sample of electrons and positrons, which will afterwards lead to a pure photon sample. Due to this fact we are setting very strict conditions during data analysis. The remaining background coming from contamination of other particles or random combinations is not subtracted. In this section, the reduction of the complete spectrum to the clean photon sample will be described briefly, which will be investigated in the following steps. In figure 5.5 the invariant mass spectrum of the photon candidate, calculated using the mass of the electron and positron, can be seen before and after the cuts (left). In addition, the remaining number of V0's after each cut is shown (right) for data (sample 2) as well as for MC.

For the reduction we start with the complete reconstructed data of ALICE, then we select a V0-finder, which filters out the V0 candidates, which were identified during the reconstruction. We have the possibility to switch between the onfly V0 finder, which searches for V0 candidates at the reconstruction level with all the tracking information still available, and the offline V0 finder, searching for V0 particles on the level of the reconstructed tracks. The selection of the V0 finder reduces the sample by $\sim 50\%$, as expected. Afterwards, we apply several conditions on the track and on the vertices. At first a non like sign condition, rejecting vertices having tracks with the same sign, and secondly, the TPC refit condition, rejecting all tracks which could not be refitted through the TPC. Additionally, we reject tracks with kinks, as our electrons and positrons can not have a kink due to their kinematics. After having now reduced the sample to roughly 40% of the whole event statistics, we try to select particles based on the specific characteristics of electrons and positrons. Therefore several cuts on the specific energy loss signal in the TPC are applied, like a strict cut around the Bethe-Bloch electron line (-3σ , $+5\sigma$) and a rejection of the entries below 1σ above the pion line for pions with a momentum larger than 0.5 GeV/c. In addition, for the studies of the material budget a low momentum rejection of the kaons, protons and pions was applied, rejecting entries in the dE/dx -distribution which are 1σ around the Bethe-Bloch curves of these particles. After having deployed all these cuts the sample is fairly clean as you can see from figure 5.6. Just at the bottom of the distribution for the case of $|\eta| < 1.4$ there might still be some contamination of pions. The σ around the different lines is based on the measured dE/dx resolution, which was improved a lot through calibration of the TPC. But one can clearly see that for low momenta ($p < 0.150$ GeV/c) there is still deviation from the expected value. At the

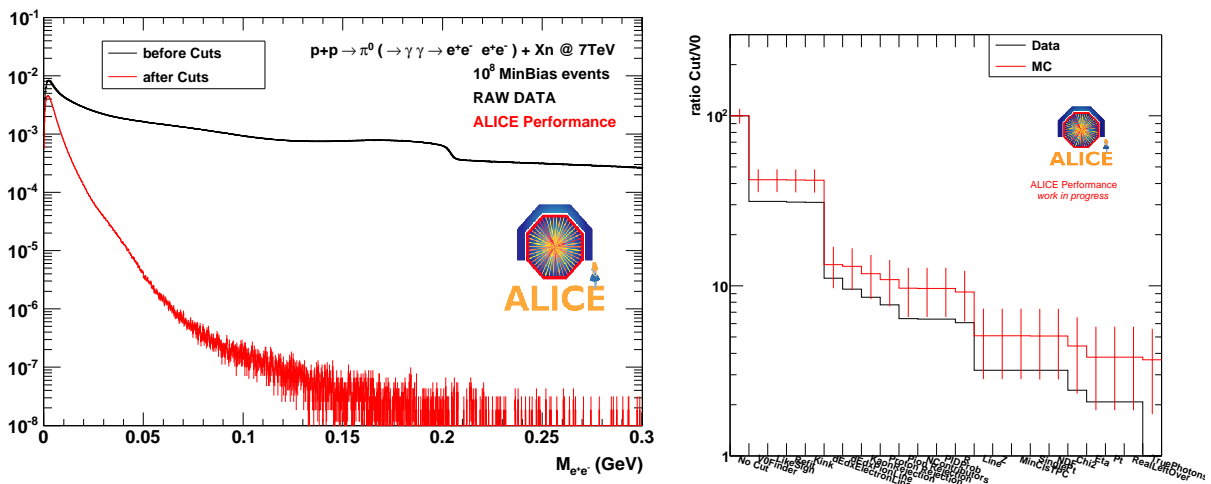


Figure 5.5.: The left plot shows the invariant mass distribution of the photon candidates before the cuts (black) and after the cuts (red). In addition on the right hand side the remaining photon candidates after all cuts with the different influence of the cuts for data (black) and montecarlo (red) are displayed.

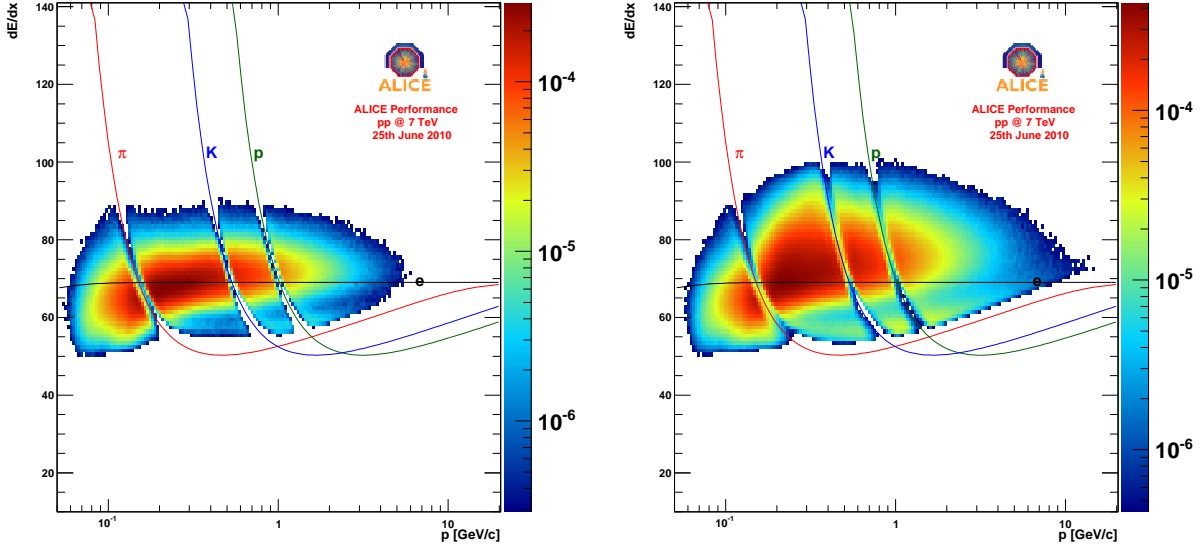


Figure 5.6.: dE/dx distribution in the TPC as a function of momentum for positrons from photon candidates for $|\eta| < 0.9$ (left) and $|\eta| < 1.4$ (right) with very strict cuts, rejecting the entries below 1σ above the pion line from $p > 0.5$ GeV/c on, as well as, a 1σ rejection around the crossing lines of K , p and π .

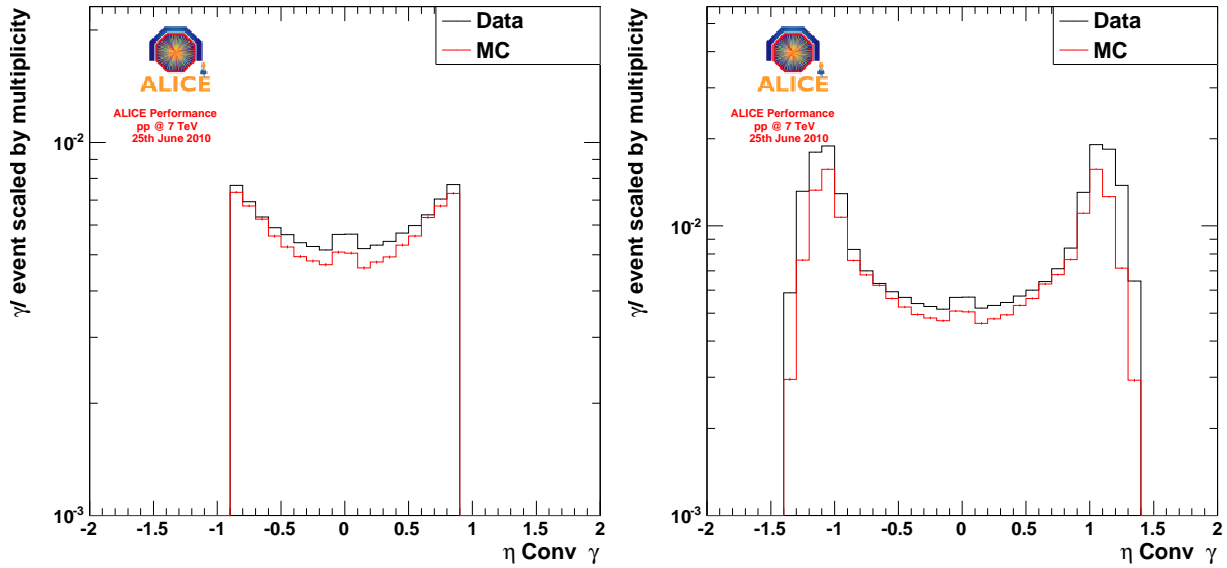


Figure 5.7.: Reconstructed photon pseudo-rapidity distributions for $|\eta| < 0.9$ (left) and for $|\eta| < 1.4$ (right) in data compared to Monte Carlo.

moment the lines are optimized for particles originating from the primary vertex, which is not the case for electrons from photon conversions. Therefore the lines do not fully agree. However by choosing -3σ and $+5\sigma$ around the electron line as the lower and upper border for the signal, we do not lose the signal.

Having now a rather clean sample, we apply some additional cuts on the geometry, like the vertex of the collision needs to be reconstructed with at least 1 contributor condition and a restriction of the R coordinate as well as the Z coordinate. Furthermore a line cut is used, rejecting all tracks beyond a line which is determined by the pseudo rapidity cut. Together with the η cut they restrict the analysis either to the main area of the detector or to the area which we are capable of and, therefore, can provide precise measurement of the material distributed in this area. In figure 5.7, the pseudo rapidity distribution is displayed for both cases. As one can clearly see in the area of

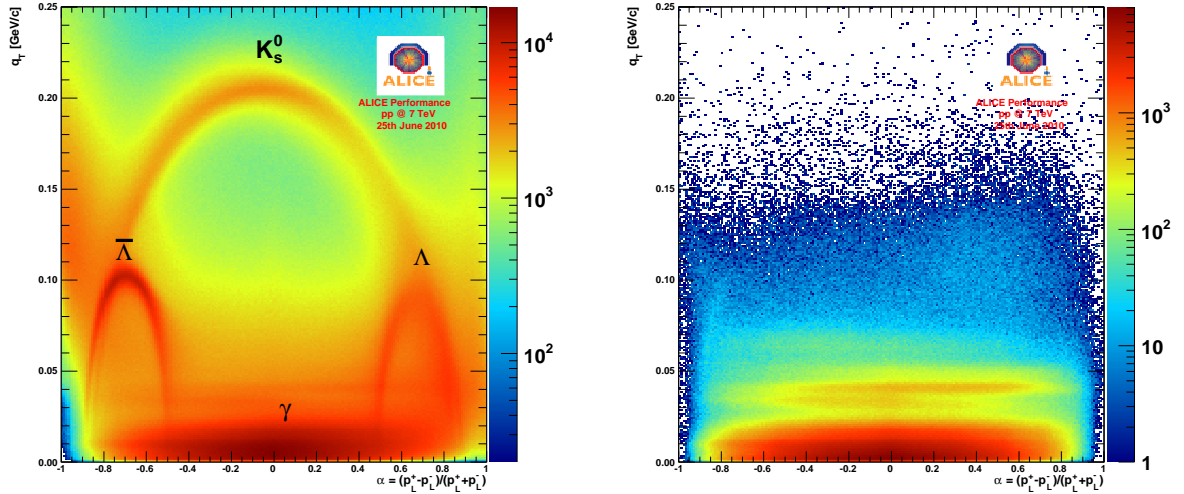


Figure 5.8.: Armenteros-Podolanski-Plot before any cut (left) and after all cuts (right) with the onfly V0-finder, this makes clear that the photon sample is very clean.

$|\eta| < 0.9$ data and Monte Carlo fit nearly perfectly, whereas in the outer parts they differ a lot. There is the possibility to apply cuts on the minimum number of clusters in the TPC, the probability of being an electron, the single p_t of the electron as well as a cut on the p_t of the photon momentum, but these are not used in this analysis. One could use several cuts on the kinematics of the photon conversion or use a Kalman filtering for this selection. For this analysis we chose to use the Kalman filtering as default, which is implemented in the AliKF package of AliRoot [35,36]. As a cross check the photon characteristics are constantly under investigation, they will be discussed in the next part. A detailed list of the cut values used for this analysis will be given in table D.1.

To prove the purity of our sample one can compare the Armenteros-Podolanski plot¹ before, where K_s^0 , Λ , $\bar{\Lambda}$ and γ are clearly visible, and after all cuts are applied, displaying the measured V0-particles. From the plots in figure 5.8 it can be concluded, that the contamination of the resulting sample is very little. The bottom distribution (figure 5.8 right) describes the distribution of the photons, whereas the line directly above might be a remnant of the reconstruction, this is still under investigation. In addition, one can obtain the purity from the Monte Carlo reconstruction, as there the true particles are known and can be related to the reconstructed, this is done in figure 5.9. The purity seems to be more than 95% for nearly all p_t .

5.6. Characteristics of selected photons

Having now proven that the purity of the photon sample is quite high, a detailed investigation of the conversion products and of the photon reconstructed from these can be done.

The normalized pair production cross section σ_{LPM}/dx versus the fractional positron energy E/k (as already discussed in subsection 3.1.3) is one of the most important distributions to look at, as it directly gives a hint, whether we are measuring the correct properties. In figure 5.10 this plot is shown for different energies as a comparison between data (black), Monte Carlo reconstructed (red) and Monte Carlo truth (blue). The Monte Carlo truth shows the expected behavior as described before (figure 3.4), while the curves for data and Monte Carlo reconstructed are different because they are convoluted with the reconstruction efficiency and the acceptance. From this plot it can

¹Method developed in 1954 by J. Podolanski and R. Armenteros to distinguish between different hadrons using the transverse and longitudinal momenta q_T and q_L of the decay particles relative to the flight direction of their mother particle. In an Armenteros-Podolanski plot the transverse momentum q_T is plotted against the asymmetry variable $\alpha = \frac{q_L^+ - q_L^-}{q_L^+ + q_L^-}$, which is a combination of the longitudinal momentum of the positive and negative decay particle. In this plot each type of decay particles describes an individual ellipses in the q_T plane.

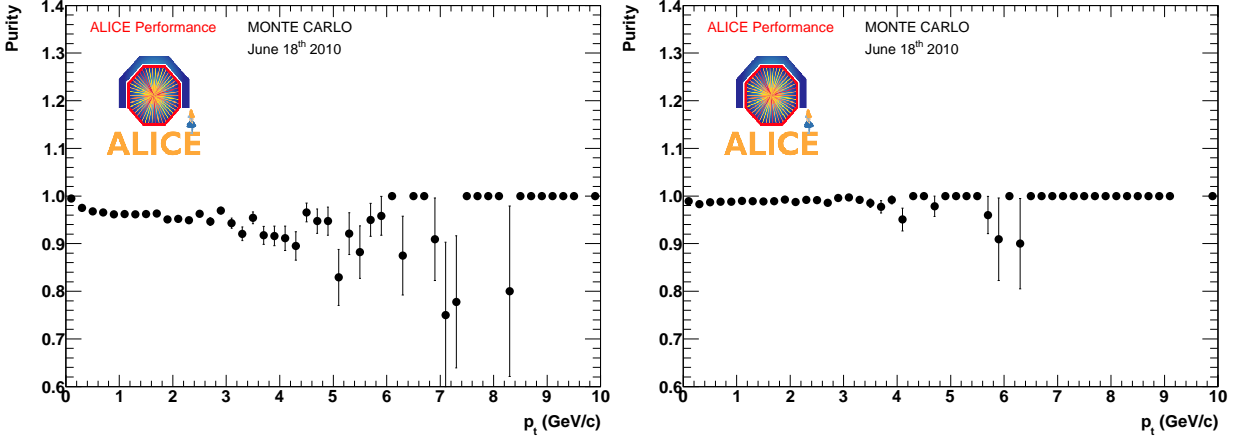


Figure 5.9.: Purity obtained with the onfly (left) and offline (right) V0 finder measured with the Pythia Monte Carlo production.

be obtained that for lower energies our acceptance plays quite an important role. The fact that the symmetry for x and $(1 - x)$ is preserved shows that the reconstruction does not introduce a bias.

After having confirmed that the measurement is correct, we will now have a look at the geometry of the conversions. Therefore we will look at the distance of closest approach (DCA) of the electron and positron tracks (figure 5.11 left plot) as well as their $\cos \theta_{pointing}$ (figure 5.11 right plot). The DCA distribution gives a hint, how good the reconstruction of the photon is. The distributions for the DCA are in quite a good agreement for data (black) and Monte Carlo (red). The pointing angle is defined as the angle between the mother momentum and the vector joining the primary vertex and the conversion point. The majority of it should be measured at ≈ 1 as the pointing angle should be nearly 0. This can be seen in the distribution (figure 5.11, right), however Monte

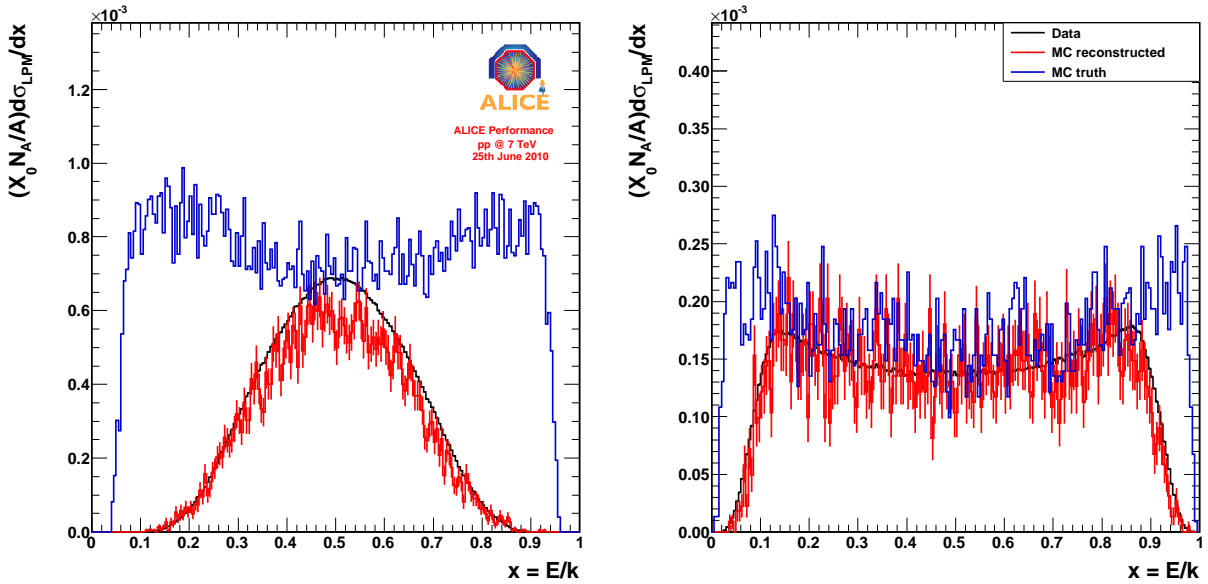


Figure 5.10.: The normalized pair production cross section σ_{LPM}/dx , versus the fractional positron energy $x = E/k$, with k the incident photon energy. Displayed are the different distributions for data (black), Monte Carlo reconstructed (red) and Monte Carlo truth (blue) at different energie ranges for which the mean energy is 0.4 GeV (left) and 3 GeV (right). The curves for data and Monte Carlo reconstructed are convoluted with the reconstruction efficiency and the acceptance, therefore they do not agree with the Monte Carlo truth. For this studies the cuts rejecting the crossing lines of pions, kaons and proton where not used, as they produce some additional structures.

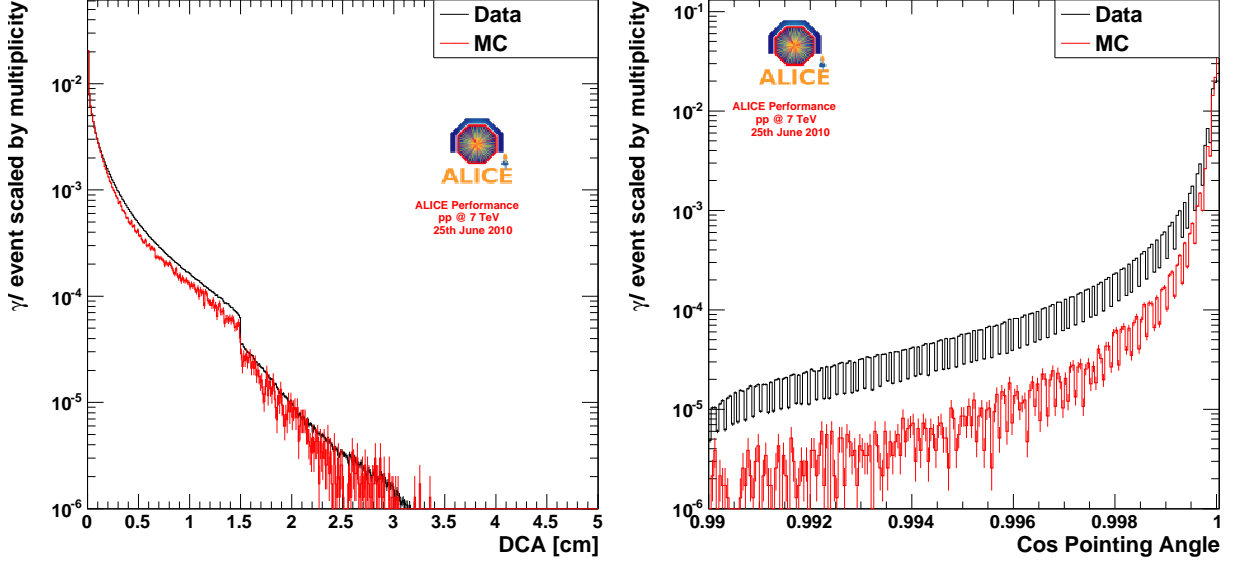


Figure 5.11.: Distribution of the distance of closest approach of the electron and positron tracks originating from the photon (left) and of the cosine of the pointing angle for the γ (right).

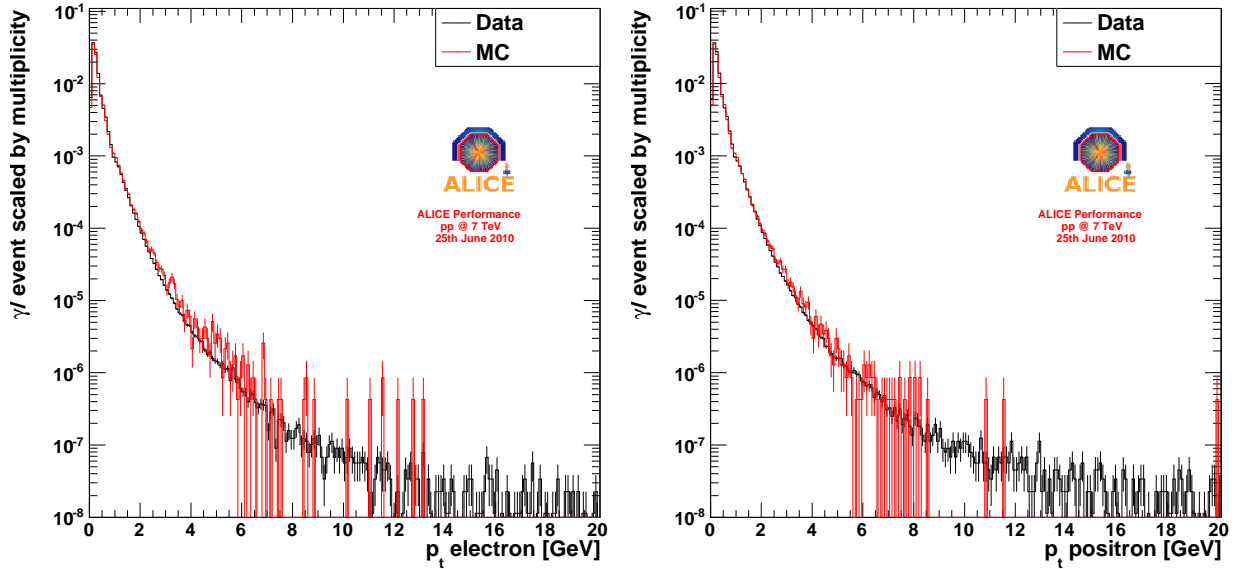


Figure 5.12.: Transverse momentum distribution of the electrons (left) and positrons (right) coming from photon conversions.

Carlo and data differ a lot, which is still an open question and needs to be investigated.

The next point to be checked is, whether the p_t distributions of the electron and positron are reasonable, as this will directly translate to the p_t distribution of the photons from which we in the end want to obtain the spectra. Therefore, the electron and positron transverse momentum spectra are compared to the distributions expected from Monte Carlo simulations in figure 5.12. Both distributions agree within the errors of the Monte Carlo distribution, which has much less statistics ($\sim 3 \cdot 10^6$ events compared to $\sim 100 \cdot 10^6$ events in data). Moreover the highest p_t we reach in the data with sufficient statistics is roughly 20 GeV.

This analysis can then be repeated for the photon p_t as well (figure 5.13). In agreement with the p_t reach of the electron and positron we reach 40 GeV with the same statistical error. Furthermore our invariant mass distribution of the reconstructed photon is quite narrow. The invariant mass of the e^+e^- should be 0 MeV, but due to the reconstruction resolution the distribution widens to

6. The Material Budget of the ALICE Detector

This chapter will be dedicated to the main result of this thesis the measurement of the material budget of ALICE with the conversion method. It provides a cross check of the real detector geometry and chemical composition of the material compared to the implemented ones in the simulation. Moreover an estimation of the systematic error of the material budget at the present level of understanding will be given.

6.1. Mapping of the different detectors

As already discussed in section 3.1.3 conversions are very sensitive to the material in which they are converting and not only to the amount and geometry of the material but to its chemical composition as well. This is the reason why with this method the implementation of the different detectors in the GEANT simulations can be tested. Using this method several mistakes in the simulations were found since the first data taking and the discrepancies could be decreased to approximately $\pm 4\%$ in the pseudo rapidity range of $|\eta| < 0.9$. But there is still work ongoing to improve the knowledge of the material in all rapidity regions. In the following, I will give an overview about the detectors that can be tested as a whole, whereas the individual detectors and their improvements will be addressed in the next sections.

In figures 6.1 and 6.2, the Y versus X -plot and the R versus Z -plot of the reconstructed photon conversion points in the fiducial region $|\eta| < 0.9$ are presented, which could be obtained with the conversion method (explained in chapter 5). The same distributions are displayed for the extended η range of $|\eta| < 1.4$ in the figures 6.3 and 6.4, respectively. These plots show the sensitivity of this method, as even the smallest structures (ladders) in the ITS can be seen and especially in the YX plots the individual parts of the detectors can be separated. For instance in the YX -plot the segmentation of the TPC in 18 chambers is clearly visible in parts of the drift gas, as well as, the TPC rods at the outer parts of the TPC inner field cage vessel. In both two dimensional plots the several layers of the ITS and the TPC are clearly separated. Moreover in the RZ plot the central electrode of the TPC is visible, with a significant red structure corresponding to the central electrode holder. Even the segmentation of the SPD, with its 10 sectors, is visible in the high resolution plots. In the fiducial region, most of the material is contained in the sensitive areas of the detector (red parts in the RZ -plots). This changes in the case of the extended pseudo rapidity range, where most of the material can be located either in the support structures and services or in the sensitive detector areas. In the region of the support structures the analysis is difficult as no tracking is possible and the tracks can only be extrapolated to these points. Therefore most analysis of primary and secondary particles are done in the fiducial pseudo rapidity range. Nevertheless the material in the outer parts of the central barrel needs to be known as well, due to the fact that for example the FMD and other forward detectors will be affected by the interactions of particles in this region. With the method we can provide a cross check of the material up to an η of ± 1.4 . Afterwards the reconstruction of tracks is not possible anymore due to the acceptance of the detectors used for the analysis.

The analysis started in December 2009 with the first collision data from the LHC measured with the ALICE detector. The measured R -distribution can be seen in figure 6.5 (left), where the data and the Monte Carlo distributions (ite 0) are scaled to the number of events. From this first analysis a discrepancy of roughly 20% was obtained. The right plot of figure 6.5 displays the same distribution for the 7 TeV data obtained up to May 2010 and the Monte Carlo production

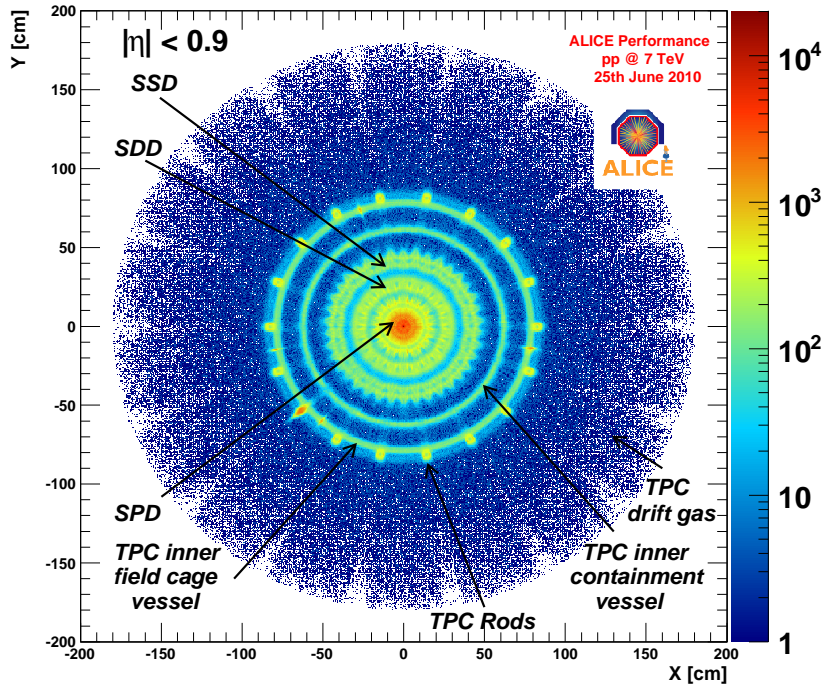


Figure 6.1.: Y versus X distribution of the reconstructed photon conversion point for $|\eta| < 0.9$ (fiducial area) in the different detectors of ALICE measured with the conversion method. The structures in the material of the different detectors can be clearly seen, as well as their ϕ distribution.

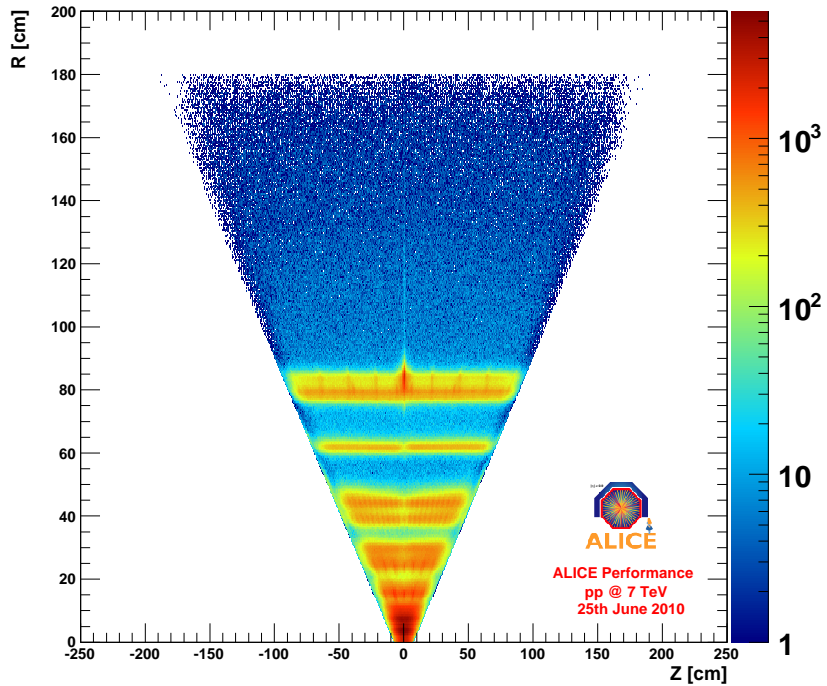


Figure 6.2.: R versus Z distribution of the reconstructed photon conversion point for $|\eta| < 0.9$ (fiducial area) in the different detectors of ALICE measured with the conversion method. The different layers from ITS to the inner parts of the TPC and the TPC drift gas are clearly visible, even some smaller structures can be seen in the layers.

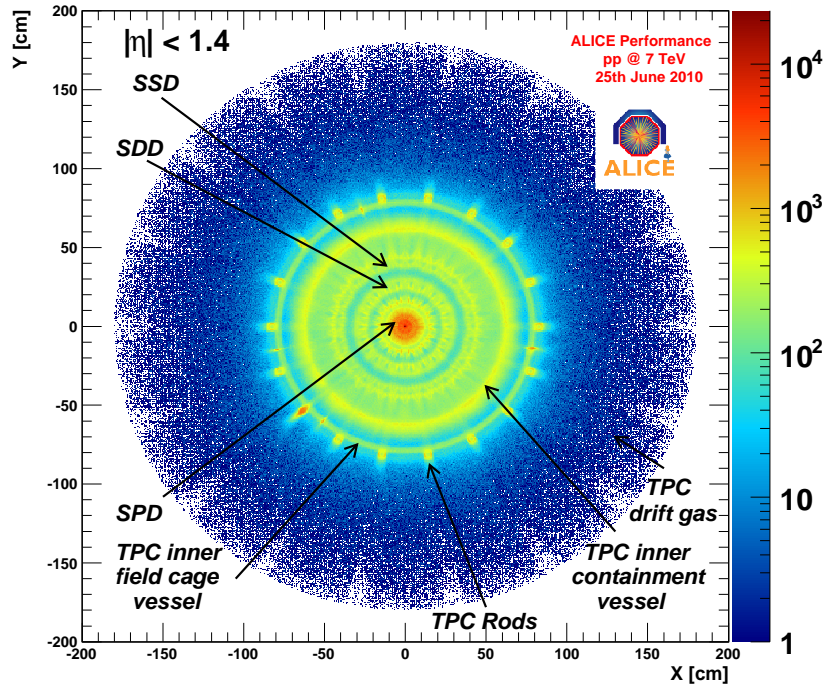


Figure 6.3.: Y versus X distribution of the reconstructed photon conversion point for $|\eta| < 1.4$ (extended area) in the different detectors of ALICE measured with the conversion method. The structures in the material of the different detectors can be clearly seen, as well as their ϕ distribution.

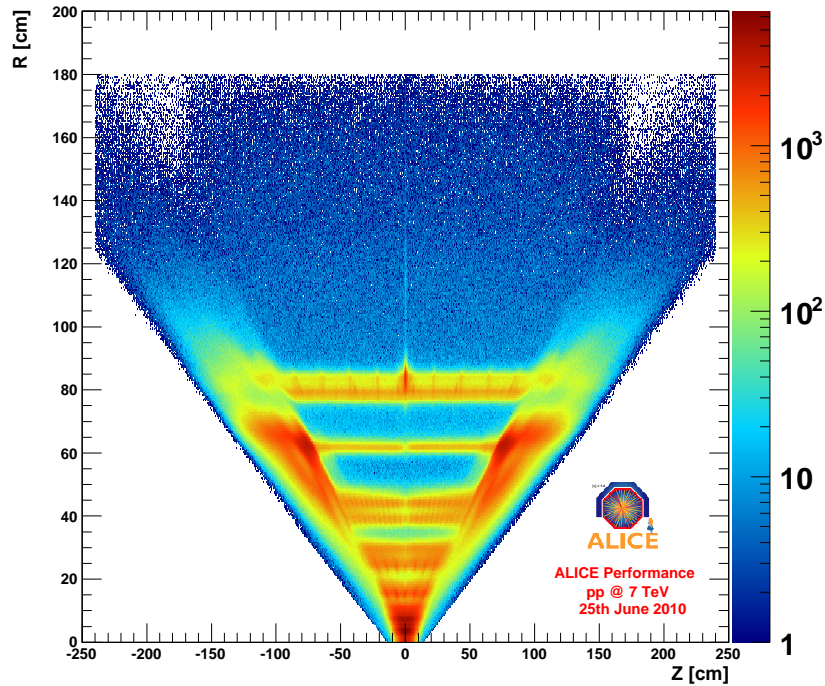


Figure 6.4.: R versus Z distribution of the reconstructed photon conversion point for $|\eta| < 0.9$ (fiducial area) in the different detectors of ALICE measured with the conversion method. The different layers from ITS to the inner parts of the TPC are clearly visible. Also the material corresponding to the support structures and services of the ITS can be seen and even some smaller structures in the layers.

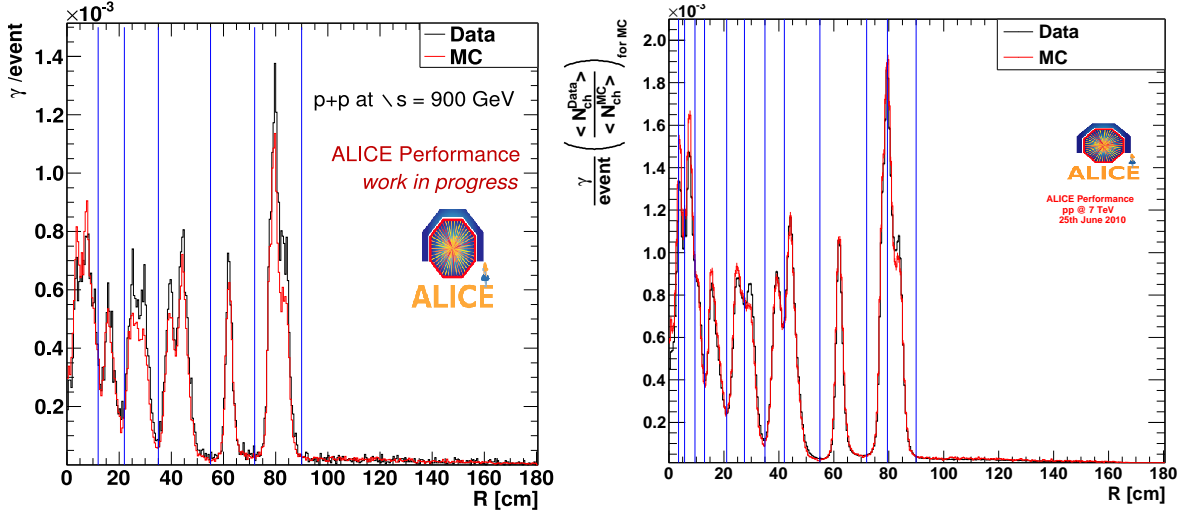


Figure 6.5.: R-distribution for the 900 GeV data of December 2009 (left) and for the 7 TeV data from the beginning of the year 2010 (right) compared to Monte Carlo simulations done with Pythia (ite 0 and ite 1). The improvements in the implementation of the material are clearly visible.

LHC10b2 (ite 1), which used Pythia as particle generator. The improvements in the detector implementation are obvious. These distributions were scaled by the number of events and the Monte Carlo distribution was in addition scaled by the factor $\frac{\langle N_{ch,data} \rangle}{\langle N_{ch,MC} \rangle}$. This was done as the multiplicity distributions for data and the different Monte Carlo event generators differ considerably, which was already discussed in section 5.3. To be able to give a detailed description of the missing material in the different detectors we divided the R and Z distribution in several bins and analyzed the differences in these bins separately. The limits of the bins can be seen in table 6.1 for the R -distribution and Z -distribution. For the R distribution these bins were chosen concerning the aspect, that in each bin only one detector part should be contained, therefore the size of the bins is quite different.

The R -distribution (figure 6.5 right) shows that in the region of the TPC a significant amount of material is still missing, as well as there are some discrepancies in the ITS parts even for $|\eta| < 0.9$

R bin	R range (cm)	Detectors	Z bin	Z range (cm)
00	0–3.5	beam pipe	00	–500, –200
01	3.5–5.75	SPD1	01	–200, –100
02	5.75–9.5	SPD2	02	–100, –50
03	9.5–13	Thermal shield/ Support	03	–50, –30
04	13–21	SDD1	04	–30, –15
05	21–27.5	SDD2	05	–15, 0
06	27.5–35	Thermal shield / Support	06	0, 15
07	35–42	SSD1	07	15, 30
08	42–55	SSD2	08	30, 50
09	55–72	Air + TPC inner containment vessel + CO ₂ (+ITS services at $ \eta < 1.4$)	09	50, 100
10	72–79.5	CO ₂ + TPC inner field cage vessel + Ne:CO ₂ :N ₂ (+ITS services at $ \eta < 1.4$)	10	100, 200
11	79.5–90	TPC rods + Ne:CO ₂ :N ₂	11	200, 500
12	90–180	Ne:CO ₂ :N ₂		

Table 6.1.: Definition of the bin in which the R -distribution (left) and Z -distribution (right) of the conversion points is divided in order to be able to give precise measurements of the deviation in the different detectors.

(ite 1). The detailed description of the missing material will be given in the next sections. After the detectors looked in detail into their implementations of the geometry in AliRoot a new Monte Carlo simulation (ite 2, see table 5.2) was performed at GSI, the distributions are shown in figure 6.6 and figure 6.7 for different η ranges. It is clearly visible that the material matches now a lot better than before. Here in some cases the structures were even overestimated. Furthermore, the TPC particle identification was improved, which affects our analysis as well. The R and Z distributions for $|\eta| < 1.4$ are not yet that well described in the Monte Carlo as for the fiducial area, but they improved as well. Combining the information from the R and Z distribution for the wider η range, it seems like especially in the outer layers of the ITS, with their support structures and services, material is still missing or underestimated. Some other discrepancies might not be visible due to this major contributions. When these are fixed some other discrepancies might be seen in addition. The ITS experts did already improve the services, but simulations of ite 3 have not yet been done.

After having now discussed the overall distribution I will concentrate on the individual distributions of the detectors and will present the detailed findings and improvements which were already done. The list of changes might not be complete, but the important ones will be mentioned. Several experts of the ITS [37] and TPC [38] worked on the open issues pointed out by this analysis and improved the geometry and the chemical composition of the individual parts quite a lot. Without these detailed investigations these improvements would not have been possible.

It was mentioned that the data sets for the comparison to MC ite 1 and MC ite 2 are not the same, the cuts on the reconstruction level were changed during the run and are slightly different, the data taking conditions (luminosity and trigger rate) were also different. Furthermore, the MC iteration 2 was done with the cuts for the second part of the run. The quality of the 2 sets of data maybe different because we are still using pass 1 of the reconstruction, as pass 2 is not yet available.

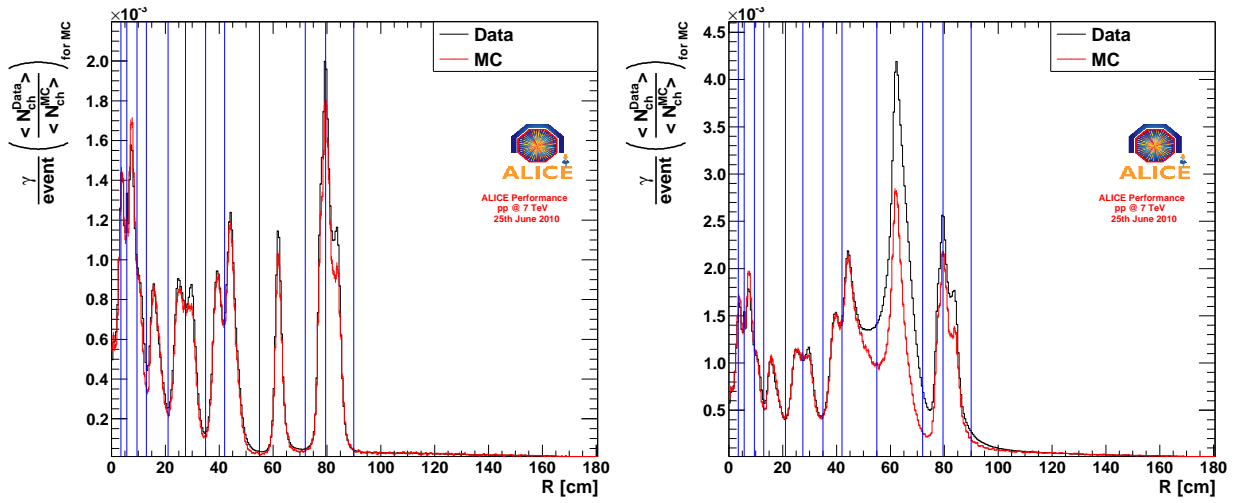


Figure 6.6.: R -distributions obtained with the Monte Carlo production (ite 2) to study the material for $|\eta| < 0.9$ (left) and $|\eta| < 1.4$ (right).

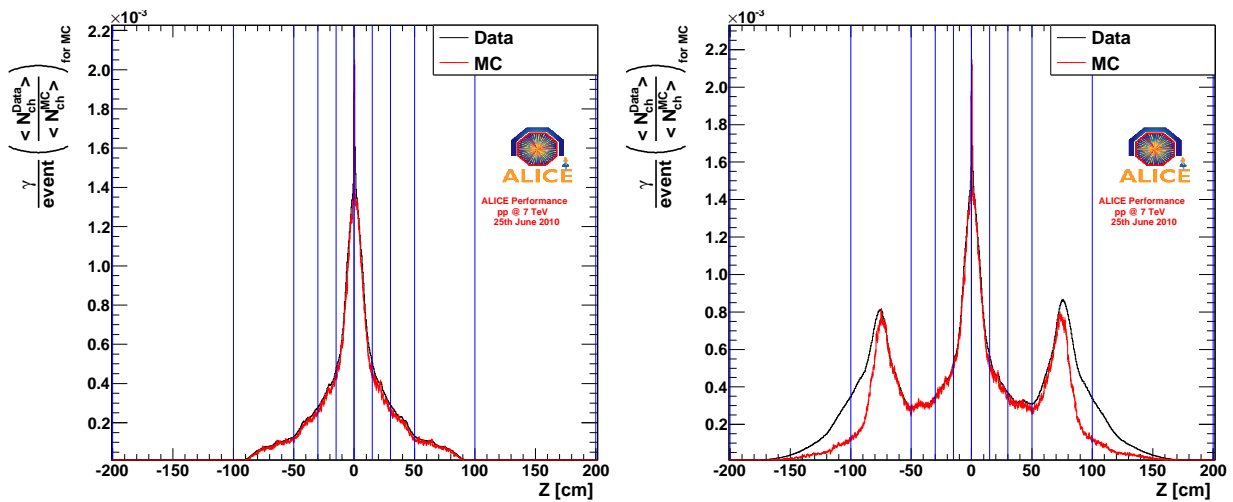


Figure 6.7.: Z -distributions obtained with the Monte Carlo production (ite 2) to study the material for $|\eta| < 0.9$ (left) and $|\eta| < 1.4$ (right).

6.2. Material Budget of the ITS

The comparison of the ITS material was done in several slices, as the ITS consists of several parts namely SPD, SDD and SSD (see section 4.2.1). Furthermore there are several structures in between like thermal shields and support structures, which needed to be investigated. In the figures 6.8 and 6.9 two of these comparisons are shown for the support structures and thermal shields between the individual detectors. In both cases the ϕ in R distribution as well as the ratio plots for the Z distributions at different R are presented for the Monte Carlo (LHC10b1 - ite 1) on the left hand side and for the Monte Carlo production carried out at GSI (ite 2) on the right hand side. In both cases for the new MC the structures are better described and match the data considerably better, however there might be an overall shift in the distributions (see tables in chapter D and the detailed plots including ratios in chapter B). Furthermore, the distributions for Z at different R are now symmetric. The large error bars in these plots are due to a lack of statistics in the Monte Carlo in the outer areas, however the trend is still visible.

In the plots in figure 6.10 the R distribution in two Z bins is displayed, one reaching from -100 to -50 cm and the other from -50 to -30 cm, it becomes obvious that structures in the center of the fiducial volume of the ITS and TPC are much better understood than the outer parts. One can see, that at least for the bin reaching from -100 to -50 cm the description improved in the parts of the SSD.

The ITS detector experts [37] spent a lot of time in searching for the missing material and checking the composition of the individual parts of the detector. Finally they found some not properly implemented parts and fixed them. Especially for the SSD there were a lot of changes which are already included in the iteration 2:

- Some metalization at the ends of the capacitors mounted on the hybrids was missing, which made nearly 4% to the total radiation length of the detector.
- The capacitors contain Palladium, which was not yet included in their chemical composition.
- Many structures in the space frame, consisting of several individual volumes, were simplified, which are now implemented correctly.
- The thickness of the thermal shield was changed for the carbon fiber skin from 0.6 mm to 0.625 mm. Furthermore the cable trays were moved to their actual position in R .
- A mismatch of the ladder cables was corrected.
- The ITS forward services at the C side were changed considerably.

In general the ITS improved their geometry by adding not only the amount of material in one piece but the real structures like cable trays and the cables inside this trays, the cooling tubes and the gas or liquid within them. As well as the differences on the A and C side for the cooling substance, which is liquid on the C side and gaseous on the A side, which will be included in iteration 3. By all these changes the material description improved, but there are still some open issues. Like the peak in the middle of figure 6.8, which should be broadened in the Monte Carlo. Furthermore, the ITS experts need to work on their implementation of the forward services. As this is the crucial region for the FMD, which measures a discrepancy in the multiplicity distribution of 200% compared to the measurement in the central barrel. For this reason there is still work ongoing and we will provide several distributions restricted to an R of 30 cm displaying the ϕ distribution at several Z positions in this region. This might help the ITS experts to search for the missing material.

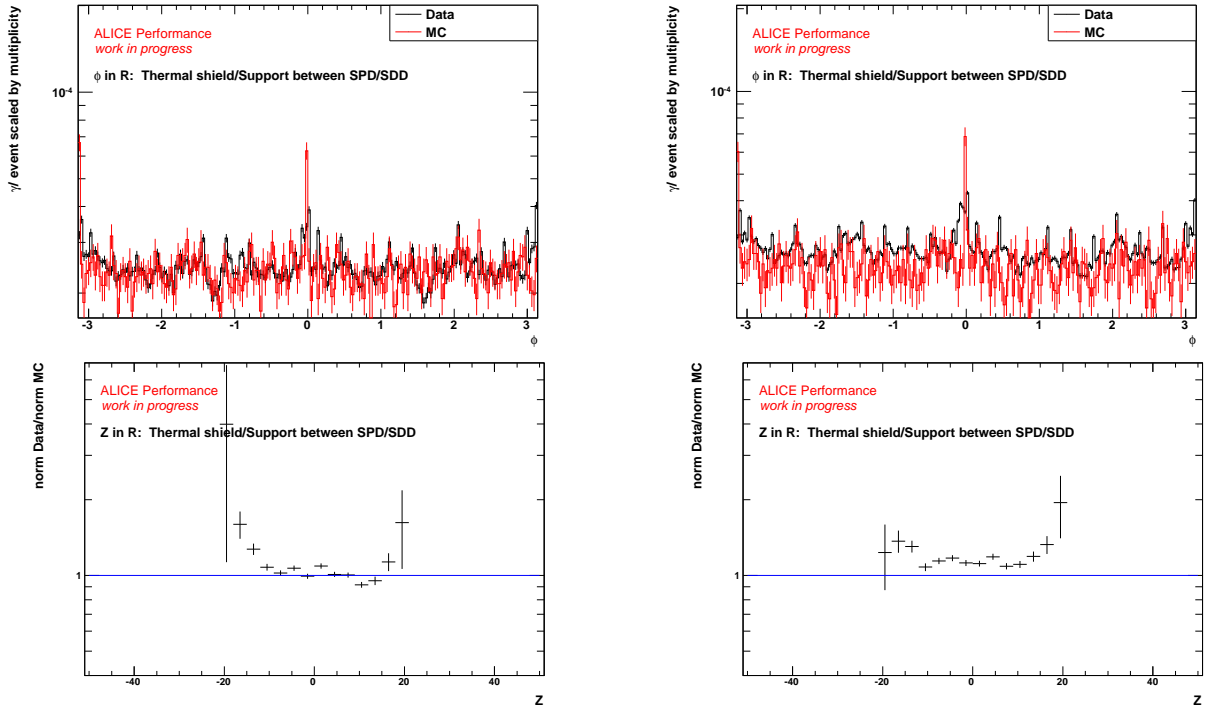


Figure 6.8.: Comparison between the Monte Carlo production ite 1 (left) and the Monte Carlo production ite 2 (right) for the thermal shield and the support structures between the SPD and SDD.

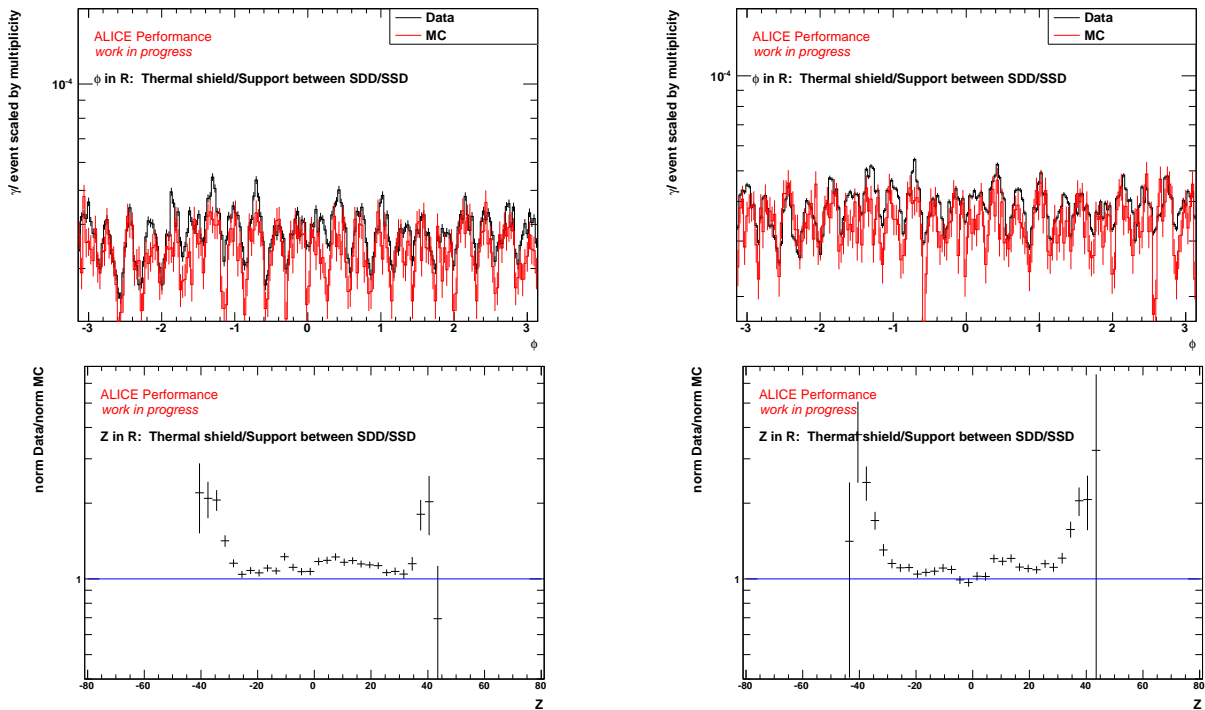


Figure 6.9.: Comparison between the Monte Carlo production ite 1 (left) and the Monte Carlo production ite 2 (right) for the thermal shield and the support structures between the SDD and SSD.

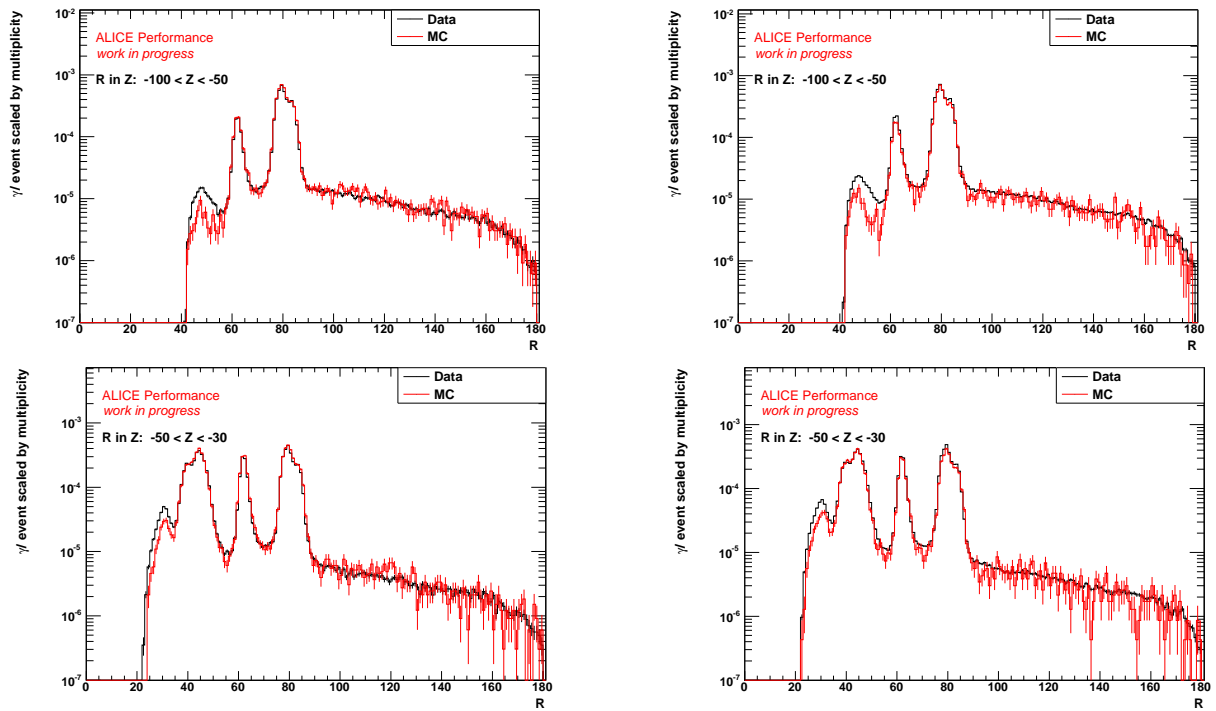


Figure 6.10.: Comparison between the Monte Carlo production ite 1 (left) and the Monte Carlo production ite 2 (right) for the R distribution measured at different Z .

6.3. Material Budget of the TPC

Not only the ITS experts invested a lot of their time in checking the implementation of their geometry, the TPC experts [38] had to do this as well, as there were large discrepancies in some of their structures. They improved their description of the material in some bin from a discrepancy of more than 40% down to 10%. In the first iteration they included some geometrical changes mainly to the inner field cage and the central drum:

- The inner field cage thickness was corrected from $7.3 \cdot 10^{-3}$ instead of $5.1 \cdot 10^{-3}$ cm. Furthermore the prepreg in the field cage was changed to $2 \cdot 0.25$ mm instead of $3 \cdot 0.1$ mm.
- The composition and the position of the resistor rods was updated.
- An epoxy film of $2 \cdot 0.1$ mm was added to the central drum.
- The segmentation and joints of the inner field cage as well as of the central drum were missing.
- The guard ring resistors were missing.

After this iteration there were still discrepancies of roughly 20% in some areas, but the mean was decreased to 14%. The investigations started again, and much finer structures were identified, which were covered before by the larger discrepancies. In the next iteration the following was corrected:

- The central electrode and its holders are shifted in R by some centimeters.
- The gas composition was updated from Ne-CO₂-N (85 : 10 : 5) to Ne-CO₂-N₂ (85.7 : 9.5 : 4.8), especially the weight for nitrogen was changed from 1 to 2.
- An update of the Ne density was done with the newest value from the particle data group.
- The pressure and temperature, that influence the gas density, were not taken at the actual value. They were changed from $T = 273 + 20$ K and $P = 1013$ mbar to $T = 273 + 18.5$ K and $P = 960$ mbar.

These changes were included in the Monte Carlo production and can now be investigated again. In figure 6.11 the ϕ distribution in several R bins of the TPC are shown: the bin for the inner containment vessel, the inner field cage and the TPC rods. It is visible, that some of the structures in the bin of the inner containment vessel were moved to the next bin (first row). Furthermore, the gas contribution reduced a little in this bin (lower parts). In the second row the valleys are now much better described, but in the peaks there are still some missing parts. The same accounts for the bin containing the TPC rods.

In figure 6.12 the Z distribution in the R bins of the TPC is presented. It is visible that the central electrode (Peak in the middle in the second row) was shifted towards a larger R in the new Monte Carlo simulation (ite 2), which matches now quite well. However, the central electrode might still be a little thicker than expected. This might explain the broader peak in the middle of the bin with the TPC rods. Furthermore we see some structure of the central electrode and holders left over in the gas bin, which are present in the Monte Carlo but not in the data. This might be due to our resolution and a difficult R binning, but it needs to be investigated.

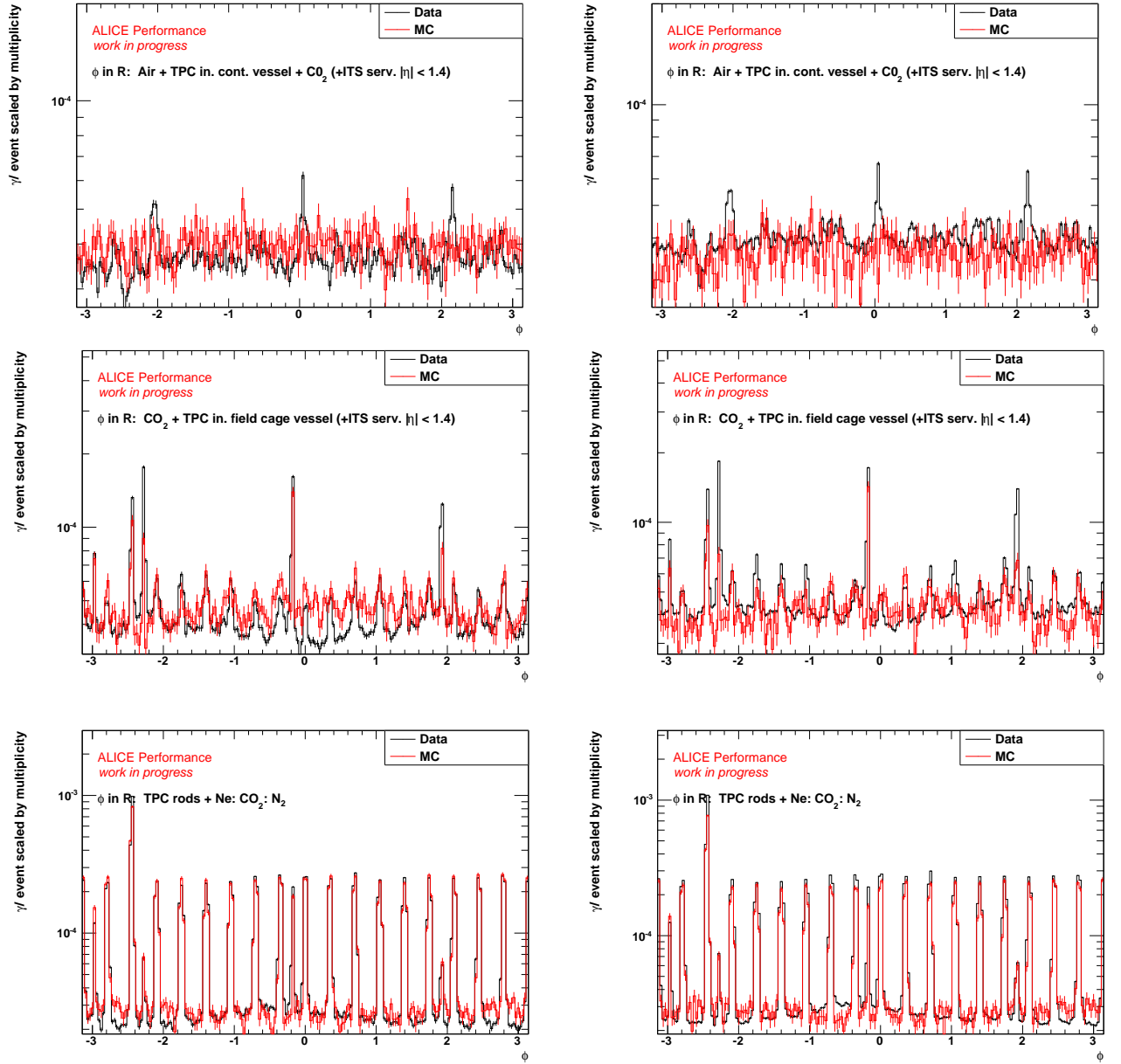


Figure 6.11.: Investigation of the changes done in the Monte Carlo simulation for the TPC in the ϕ distribution in the different R ranges, MC ite 1 on the left hand side and MC ite 2 on the right hand side compared to data.

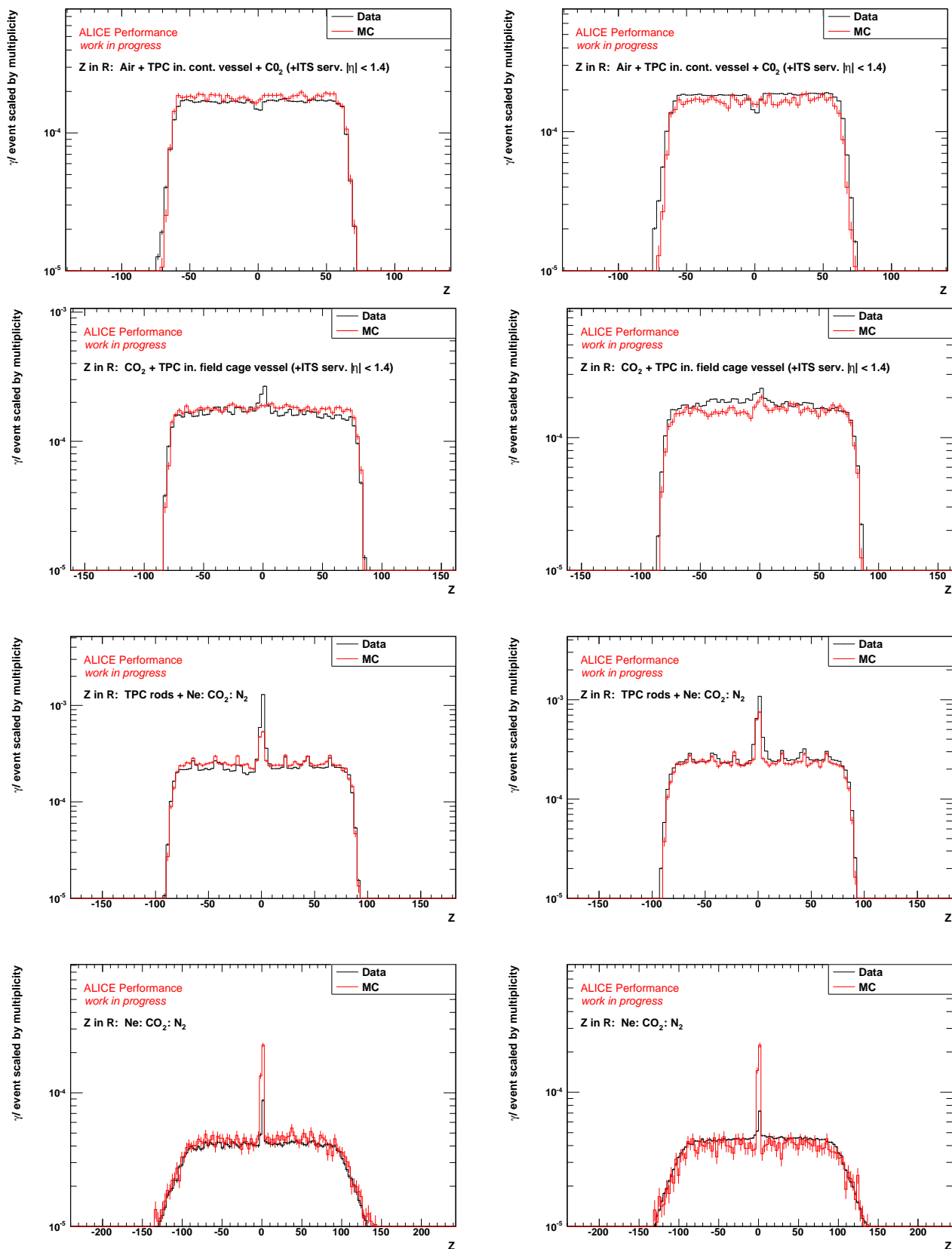


Figure 6.12.: Investigation of the changes done in the Monte Carlo simulation for the TPC in the Z distribution in the different R ranges, MC ite 1 on the left hand side and MC ite 2 on the right hand side compared to data.

6.4. Systematic Error Estimation for the Material Budget

To obtain the systematic error of the material the analysis was done for the two different V0 finders, giving an independent selection of the photons. Moreover, two different Monte Carlo productions were checked, LHC10b1 using Phojet as particle generator and LHC10b2 using Pythia. The deviations were calculated in the different bins and afterwards the systematic error was assumed in two different ways:

- Taking all deviations where Monte Carlo simulation is higher than the data and summing then separately from them where the deviation is in the other direction. This takes into account that the deviations are not independent of the R were they are sitting and enter in the over all deviation with a different amount. In the end out of the four comparisons the biggest deviation for each type was taken as the systematic error. This is a rather conservative choice of the error.
- The second possibility is to give the summed deviation and take the highest values for the different comparisons as the total error.

Both methods were used in taking the full p_t range or a limited p_t range, where the conversion probability and reconstruction efficiency are not changing significantly anymore. With this method a systematic uncertainty to the material could be assumed which is either

$$-4.69\% \text{ and } +5.18\%$$

taken from the separated differences or

$$-3.90\% \text{ and } +4.15\%$$

assumed by the total deviation. The detailed table for the error calculation can be found in table 6.2. Furthermore, the tables for the deviations in each bin for the four different combinations can be found in the appendix in chapter D.

These studies were carried out with the Monte Carlo productions ite 1, where the changes of the ITS and TPC were not yet fully in. Furthermore the data sample used included only 30 Mio events (sample 1), as afterwards some cuts at the reconstruction level were changed.

V0finder	Phojet			Pythia Perugia 0		
All p_t	Error neg [%]	Error pos [%]	Error sum [%]	Error neg [%]	Error pos [%]	Error sum [%]
offline	-4.12	1.60	-2.51	-4.69	-0.79	-3.90
onfly	-3.40	2.47	-0.93	-4.55	1.61	-2.94

V0finder	Phojet			Pythia Perugia 0		
Mid p_t	Error neg [%]	Error pos [%]	Error sum [%]	Error neg [%]	Error pos [%]	Error sum [%]
offline	-1.77	3.43	1.65	-4.17	1.29	-2.89
onfly	-1.04	5.18	4.15	-3.17	2.05	-1.12

Table 6.2.: Error calculation for different particle generators, which were used as well as the two V0-finders. The differences are always Data - MC. The upper table is photons in the full p_t range, whereas the lower one displays the same for a middle p_t range (0.4 – 1.5 GeV) of the photons, where the conversion probability and reconstruction efficiency are not changing significantly anymore.

V0finder	Pythia Perugia 0		
All p_t	Error neg [%]	Error pos [%]	Error sum [%]
offline	0.00	14.90	14.90
onfly	-0.26	7.19	6.93

V0finder	Pythia Perugia 0 mid p_t		
Mid p_t	Error neg [%]	Error pos [%]	Error sum [%]
offline	-0.11	10.86	10.75
onfly	-0.12	6.97	6.85

Table 6.3.: Error calculation for different V0 finder for the Monte Carlo production ite 2 with the new material budget. The differences are always Data - MC. The table shows photons taken in the full p_t range (left) and taken in a middle p_t range (0.4 – 1.5 GeV), where the conversion probability and reconstruction efficiency are not changing significantly anymore.

This analysis was repeated with for the Monte Carlo production ite 2, which used Pythia as particle generator. A different data set with the new more open cuts at the reconstruction level was chosen, to be comparable to the Monte Carlo, which already used these open cuts. For the onfly V0 finder, loose cuts were applied, the possibility of being a pion or muon for a given track was changed from being smaller than 0.7 to 0.9. On the other hand the cuts for the offline V0 finder were opened significantly, to understand the K_s^0 yield at low p_t . These changes affect the γ reconstruction as well and the characteristics of the photon especially for the offline V0 finder do not match that nicely anymore. Moreover, the data taking conditions (luminosity and trigger rate) were also very different. The new errors estimated from this comparison are presented in table 6.3. The calculated errors are larger which is due to different statistics as well as the different data sets. It is not yet clear how much of the discrepancy comes from contamination and how much from the difference in the photon characteristics. This needs to be investigated again after Pass 2 of the reconstruction is available. Therefore the Monte Carlo production with iteration 2 will not be used for the error estimation, until these changes are understood. To asses the systematics of the data, the two data sets were compared to each other. For this discrepancies of 12.27% (see table D.15) for the onfly V0 finder (minor changes in efficiency) and 36.80% (see table D.14) for the offline V0 finder (mainly due to larger efficiency) were revealed.

The error on the material budget is therefore estimated with the productions of ite 1. However the MC ite 2 was used to check the already implemented improvements in the different detectors and for a further investigation before a new central simulation will be carried out at CERN.

7. Studies of the Resolution of the Conversion Method

Up to now we only claimed that the resolutions for the conversion point are quite good, to prove this, a resolution study was carried out and will be presented in this chapter. Furthermore, this study is a first step towards an investigation of the possibility to define a L1 trigger for high p_t photons using the TRD by measuring the properties of the resulting high p_t electrons and positrons from the photon conversion. At first the spatial resolution of the calculation of the conversion point will be discussed. Afterwards the emphasis will lie on the p_t resolution obtained with this method. For these studies a Monte Carlo production with flat p_t was used, that means that the transverse momentum spectrum for the π^0 is not steeply falling, but is flat for all p_t . The transverse momentum distributions for corresponding electrons, positrons and photons are shown in figure 7.1. These are quite different compared to the p_t distributions in the real data shown in chapter 5.6. This simulation was used to reach high p_t without creating a huge amount of Monte Carlo events. Due to the fact, that we recalculate the conversion point using the transverse momentum the resolution of the transverse momentum enters in the spatial resolution as well. Therefore the results obtained with the flat p_t simulation might be worse than the actual ones, as the spatial resolution is getting worse with higher transverse momenta.

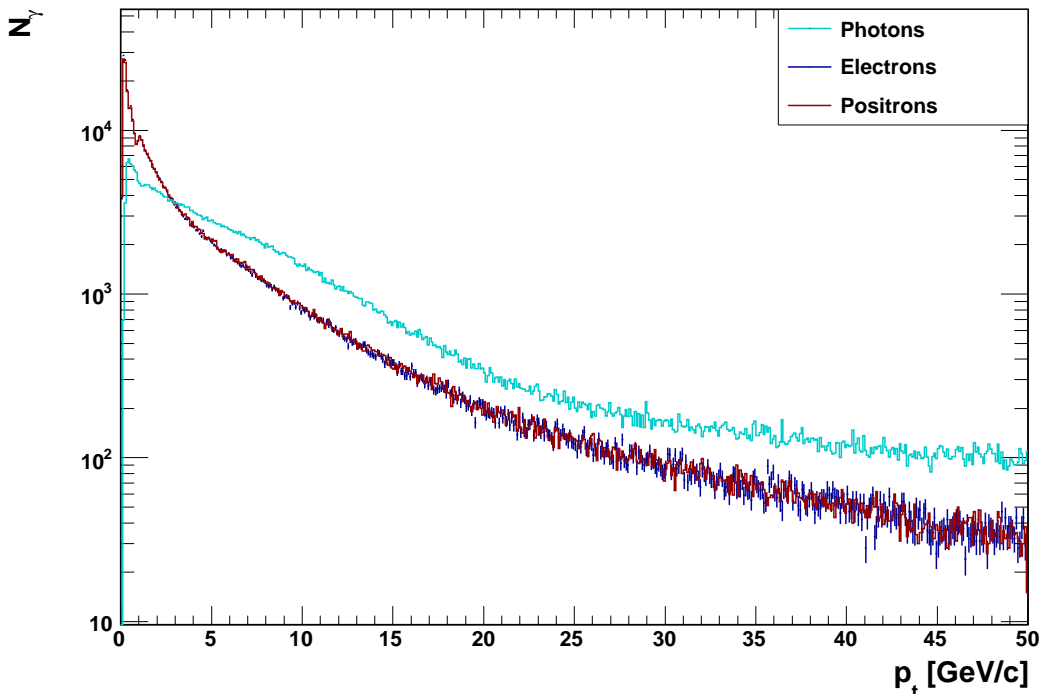


Figure 7.1.: Transverse momentum distribution for the different particle species: electrons (blue), positrons (red) and photons (cyan) for a flat p_t distribution.

7.1. Spatial Resolution of the Conversion Point

In the Monte Carlo simulation each particle is stored at least twice, once with the real track propagated through the detectors, which is done by GEANT, and the second track is the reconstructed one, which is reconstructed with the same conditions as the real data. Furthermore, both tracks have a unique identification (ID) number, by which they can be matched afterwards. This gives the possibility to calculate the deviation from the real coordinate to the reconstructed coordinate, calculated with the conversion method.

This was used to obtain the resolutions in ϕ , R and Z versus the radial position. The distributions are shown in figure 7.2, 7.3 and 7.4 on the following pages.

The fitting was done with a Gauss function defined as:

$$f(x) = \frac{1}{\sqrt{2\pi}\sigma} \exp\left(-\frac{1}{2}\left(\frac{x-\mu}{\sigma}\right)^2\right) \quad (7.1)$$

where μ is the mean (or Peak position) of the distribution and σ is the standard deviation, which gives us the resolution of this coordinate. The simple Gauss function can be used, as the deviation from the means is statistically distributed. However the Gaussian does not describe the whole distribution. For the outer parts a second Gaussian convoluted with an exponential function would be needed to fully reproduce the observed distribution.

To be able to use a single Gaussian nonetheless, a restriction of the fit range needs to be done. This was done for these resolution studies with a recursive fitting restricting in each step the fit range to $\pm 2\sigma$ around the mean μ . This fitting will either stop because the sigma does not change anymore to a given precision or because the fit did not converge within 100 iterations. The fitting is done trying to minimize the χ^2 . Furthermore, the binning in R is not homogeneous. It was chosen with very fine bins for the areas where we have material and with large bin in the regions where there should be no material.

Even with this method the fits in the R and Z distribution are not the best. Here a second iteration with a modified function will be necessary. With the method which was used for this studies we can only give a lower limit for the resolution in these coordinates, due to the fact, that we are missing the tails. The ϕ -resolution on the other hand can be described with this approach quite well. The absolute resolution in ϕ can be seen in figure 7.2. We have a resolution within 1.7 mrad and 2.5 mrad, in some parts of the SPD and SDD the resolution is even better. Furthermore, the mean deviates just very little from 0 mrad. This proves how precise measurements in ϕ are possible.

The resolution in Z is presented in figure 7.3. Here the mean varies mostly within ± 0.1 cm, which is quite good as well. The resolution is for most R ranges between 0.8 cm and 1.5 cm. With this measurement, we prove that misplacements in this coordinate can be located very precisely.

The last part of the spatial resolution is the resolution in R which can be seen in figure 7.4. For this distribution the mean is shifted a little towards positive values and the resolution is depending on the R between 1.5 and 3 cm, which is not as precise as we expected. The problem with this distribution is that for lower R the distributions are highly asymmetric, due to the fact that R is not defined for negative values, which makes the fitting somehow problematic.

Nevertheless with this resolutions we can provide a very good cross check for the material implemented in the simulations and several real findings of missing material prove the importance of this method for the improvement of the simulations.

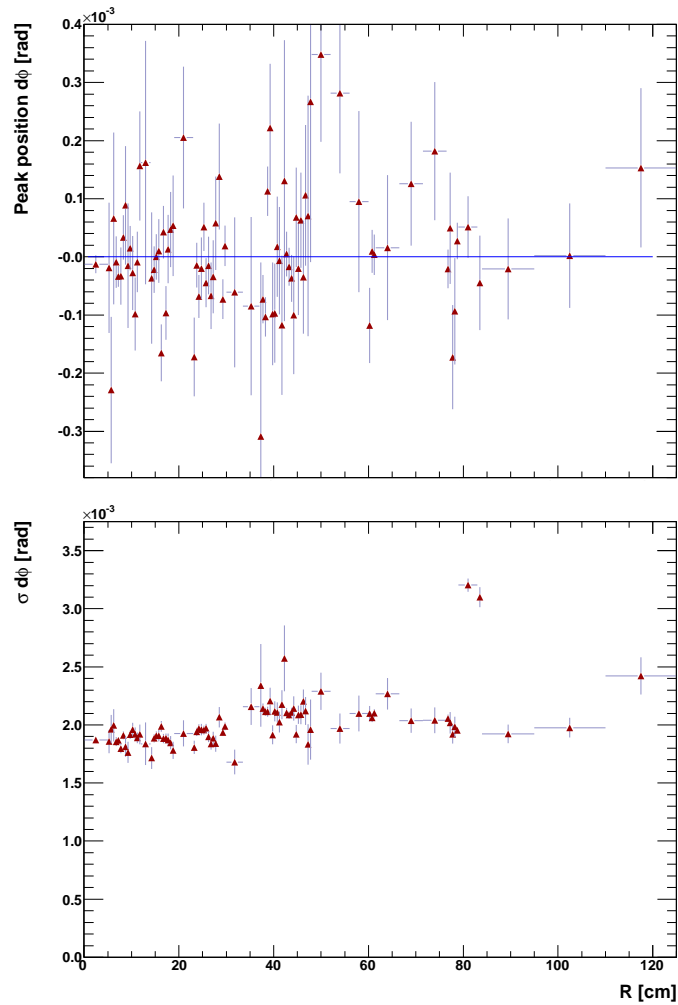


Figure 7.2.: Spatial resolution of the conversion point in ϕ versus the radial position R . Upper plot; mean of the different slices in R and lower plot: ϕ -resolution at given R .

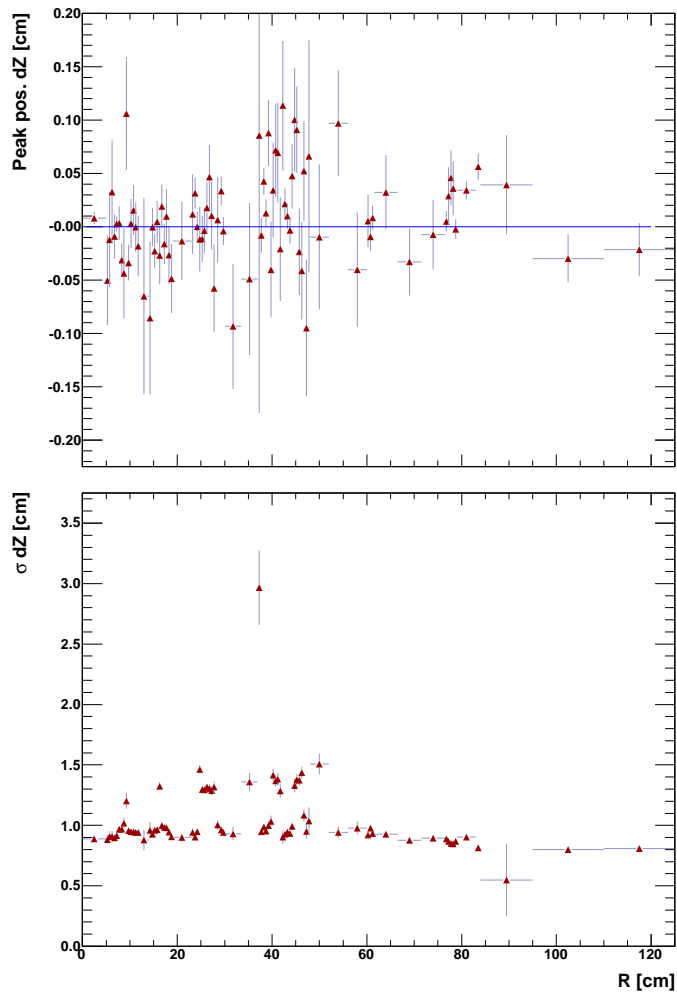


Figure 7.3.: Spatial resolution of the conversion point in Z versus the radial position R . Upper plot: mean of the different slices in R and lower plot: Z -resolution at given R .

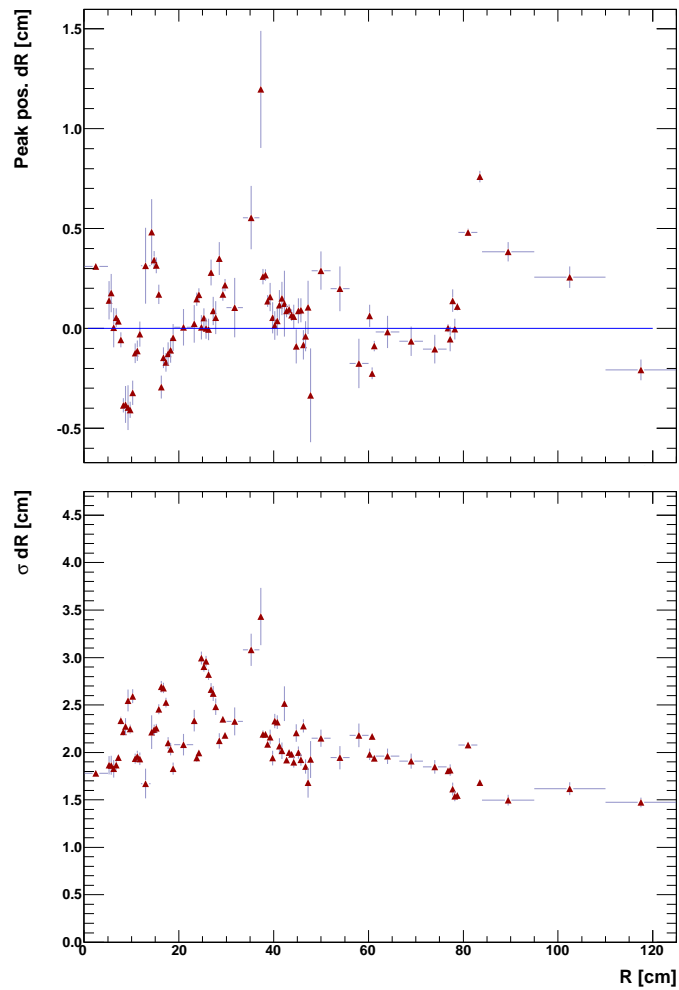


Figure 7.4.: Spatial resolution of the conversion point in R versus the radial position R . Upper plot: mean of the different slices in R and lower plot: R -resolution at given R .

7.2. Momentum Resolution of the Conversion Method

Not only the spatial resolution is important for our analysis, as already mentioned the transverse momentum resolution is even more important. Due to the fact, that this will influence the spatial resolution as well. Therefore the momentum resolution was checked in ϕ and R . Additionally the p_t -resolutions for the different particles (electrons, positrons and photons) were inspected. For the investigation of the possibility to introduce a L1 trigger at the level of the TRD the cluster and tracklet distributions were checked for the conversion electrons and positrons.

For the fitting the same method as for the spatial resolution was used. In the case of the electrons and positrons the Gauss function should be convoluted with an exponential function due to energy loss via Bremsstrahlung, this was not yet implemented.

Firstly, we want to investigate the momentum resolution for the photons versus R , which is shown in figure 7.5. As you can see from the upper plot the mean is not centered at 0 and in addition it shows a systematic slope. This behavior is not yet explained and needs to be corrected in the reconstruction. Nevertheless the resolution, seen in the lower plot, seems to be within 1% and 2% precision at a given p_t .

The next step is to look at the resolution of p_t in ϕ slices. This distribution can be seen for

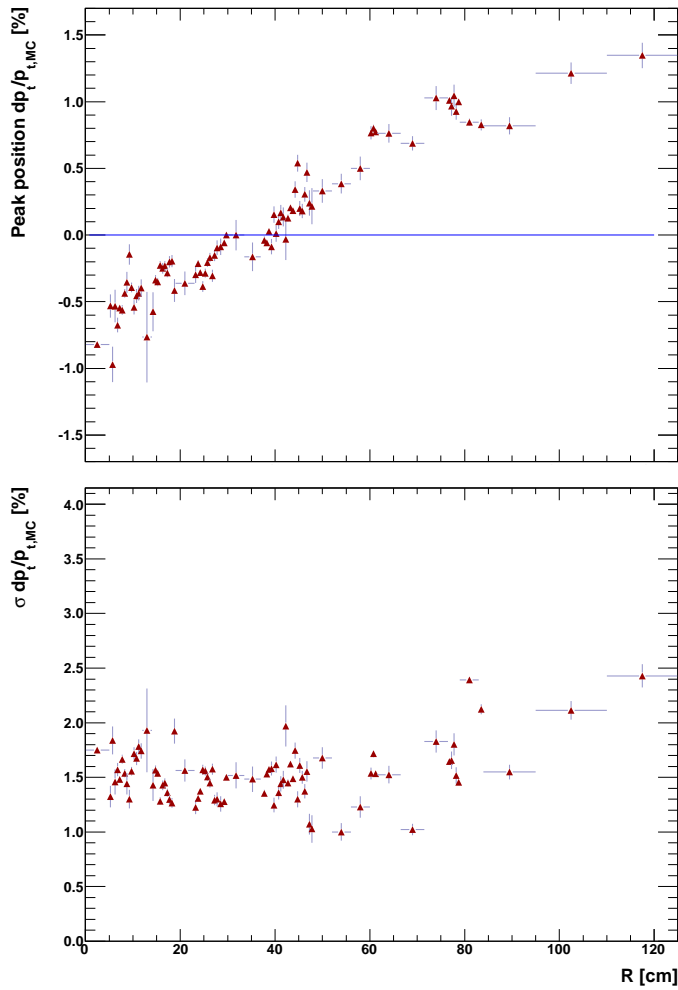


Figure 7.5.: Transverse momentum resolution dp_t/p_t for the photons versus the radial position R of the conversion point. Upper plot: mean of the different slices in R and lower plot: dp_t/p_t resolution at a given R .

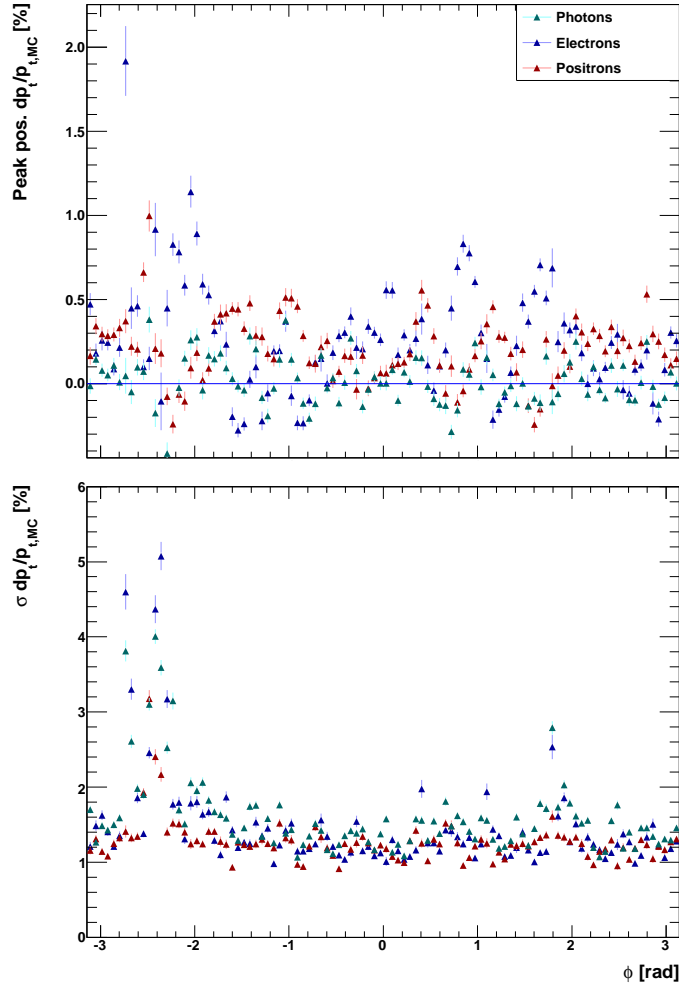


Figure 7.6.: Transverse momentum resolution dp_t/p_t for electrons (blue), positrons (red) and photons (cyan) versus the ϕ . Upper plot: mean of the different slices in ϕ and lower plot: obtained resolution for dp_t/p_t at a given ϕ .

the different particle species in figure 7.6. Here the mean for all particle species seems to be distributed statistically around 0% within a $\pm 0.5\%$ precision. Only for around a ϕ of 2.5 rad there are significant differences, which show up in the resolution as well. This chamber has less precision of the momentum resolution in the TPC, which is reflected in our p_t distribution as well. In this chamber the momentum resolution lies at roughly 4% at a given momentum, whereas in all other chamber the resolution is mostly better than 1.8% at a given p_t . This momentum resolution leads to such good result in the spatial resolution in ϕ of the conversion point.

Additionally, the resolution of $\frac{dp_t}{p_t}$ versus p_t was inspected for conversion electrons, positrons and photons. The result are presented in figure 7.7. For transverse momenta up to 20 GeV/c the mean seems to have a slope, afterwards no statement can be made due to a lack of statistics. Moreover, a dependence of the resolution in $\frac{dp_t}{p_t}$ on the transverse momentum is seen in the lower plot. The measured momentum resolution for the conversion method reflects the charged particle momentum resolution, which is getting worse for higher momenta. In the case of the calorimeters it is other wise around, the resolution is worse for low momenta, but improving with higher momenta. It has to be considered that due to smaller statistics a variable binning was used, joining bins for higher p_t to be able to fit the distribution. The resolution of the individual particles is worse than the momentum resolution of the reconstructed photon. This can be explained on the one hand by the combination

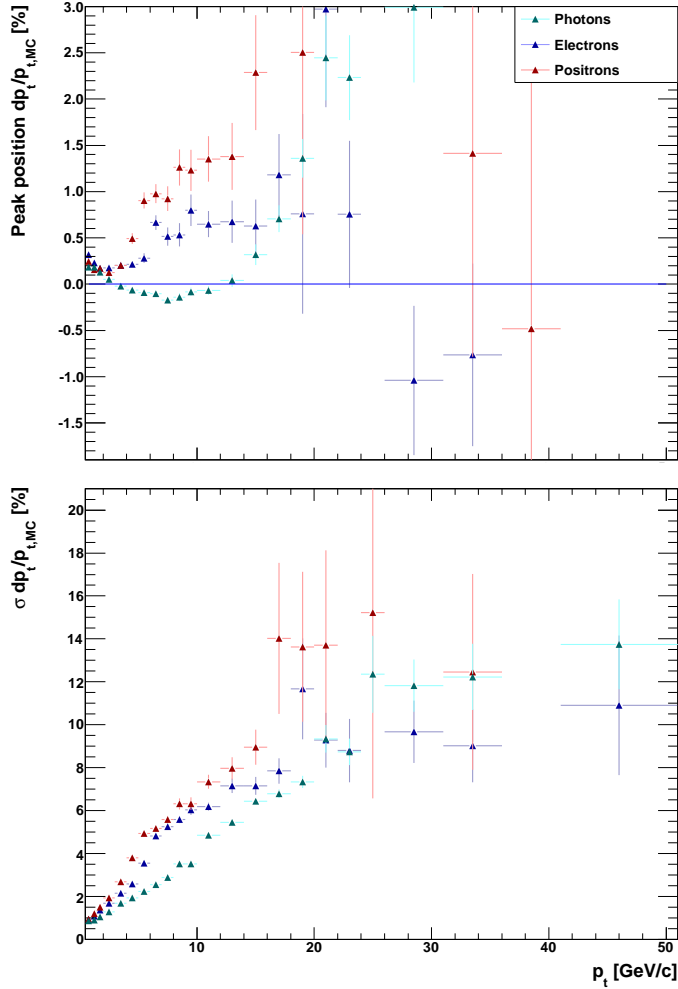


Figure 7.7.: Transverse momentum resolution dp_t/p_t for electrons (blue), positrons (red) and photons (cyan) versus the transverse momentum p_t . Upper plot: mean of the different slices in p_t and lower plot: obtained resolution for dp_t/p_t at a given p_t .

of two particles (electron and positron) with roughly half of the transverse momentum of the photon, which are more precisely measured, to one photon and by the more precise measurement after combining both particles and their constraints. Furthermore the resolution of the positron resulting from the conversion seems to be slightly worse than the resolution of the conversion electron at large momenta. But this trend is not yet conclusive and might be due to a lack of statistics as well, as the error bars are quite large.

The same analysis was repeated for conversion positrons and electrons reconstructed with a different number of clusters in the ITS. For this study one has to be keep in mind, that all conversions happening after $R \simeq 42$ cm will not have any ITS cluster, as a minimum of 2 ITS clusters is required on the reconstruction level to reduce the background. Considering this condition nearly half of our tracks will have no ITS clusters at all, because nearly 43% of the conversions happen after an R of 42 cm. In figure 7.8 the results for the different cases, only TPC, 2 ITS clusters, 4 ITS clusters, 5 ITS clusters and 6 ITS clusters are presented for positrons and electrons. This separation seems to be valid for a p_t up to 8 GeV/c with an acceptable error, afterwards the fits seem to be very bad due to few entries in these bins. For this studies at higher p_t it will be necessary to produce a flat p_t Monte Carlo Simulation with significantly higher statistics. But still the results up to 8 GeV/c show that the resolution improved for tracks which had at least 2

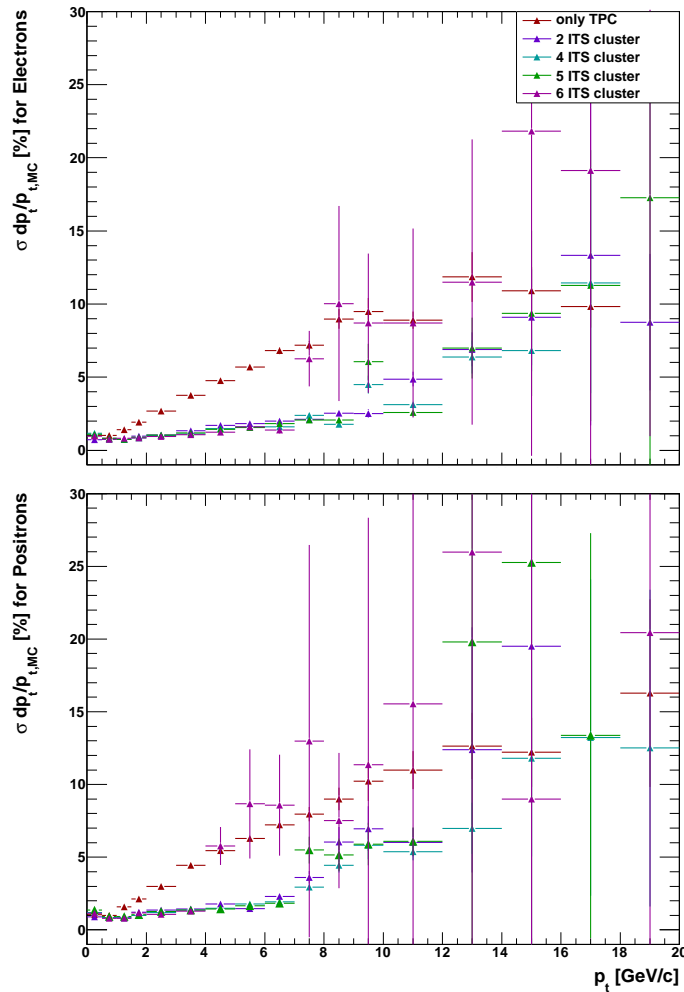


Figure 7.8.: Transverse momentum resolution for different characteristics of the track, only TPC and with a different number of ITS clusters (not all are displayed). The upper plot shows the resolution in p_t for electrons and the lower one for positrons.

ITS clusters and even more with 4 and 5 clusters. For the case of 6 ITS clusters the conversion has to happen very close to the primary vertex, which might cause some side effects, therefore the resolution with 6 ITS clusters worsens compared to the case where only TPC is used again from some p_t on. To improve the p_t resolution for all tracks one would need to include the TRD in the tracking and the momentum calculation, which is foreseen in the future AliRoot version, as then for the tracks, where only TPC information is available, the p_t resolution could be improved (see figure 4.5).

7.3. TRD characteristics for electrons (positrons) from conversions

After having now discussed the transverse momentum resolution, a detailed investigation of the TRD needs to be done to check, whether it is possible to introduce a high p_t photon trigger on the level of the L1. Therefore in the Monte Carlo simulation electrons and positrons from the photon conversions going through the whole TRD were selected and for them the distributions of the number of clusters and tracklets in the TRD at a given p_t were studied. The results of the analysis are presented in figure 7.9, on the left hand side the distributions for the electrons are shown, whereas on the right hand side the distributions for positrons are investigated. In the

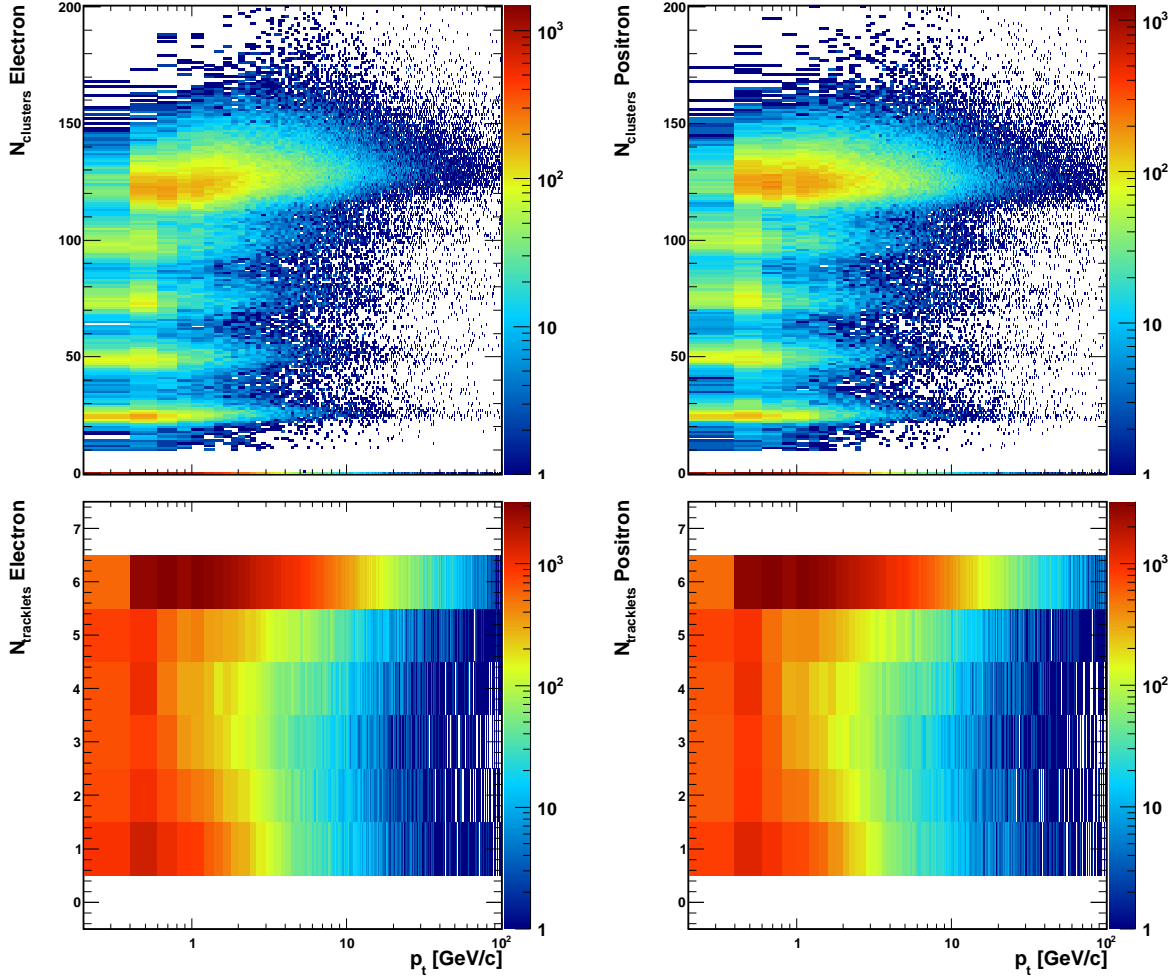


Figure 7.9.: Distribution of the number of clusters $N_{cluster}$ and the number of tracklets $N_{cluster}$ in the TRD for electrons (left) and positrons (right) versus the transverse momentum p_t of the electron (positron).

first row the number of clusters versus the p_t of the electron/positron is presented, whereas in the second row the number of tracklets for these particles is displayed. It is visible that for p_t higher than 10 GeV/c the number of clusters is mostly higher than 100 and the number of tracklets is mostly 6 clusters, which means, that in all TRD layers the particle could be reconstructed.

This studies showed that particles coming from conversions at higher p_t , can be detected with the TRD with a large number of clusters. The next step towards a high p_t trigger would be to study the properties of this electrons and positrons, like their opening angle and up to which p_t the tracks for the positron and electron originating in one conversion can be separated. Furthermore, the relation between the offline reconstructed transverse momentum and the momentum measured with the Global Tracking Unit (GTU) of the TRD needs to be studied in detail; namely as a function of the momentum and R position of the conversion point.

8. Conclusions and Outlook

In this thesis the conversion method for the measurement of photons in a huge detector system was presented. With the conversion method it is possible to investigate the material budget of the ALICE detector with a very good precision. In addition, it was shown that the spatial resolution is better than 3 cm in the R -coordinate, better than 1.5 cm in the Z coordinate and better than 2.5 mrad for the ϕ coordinate. Due to this very good resolution small structures in the detector can be resolved and due to the sensitivity of the method the chemical composition can be tested as well. This allows a detailed γ -ray tomography of the detectors. The results of the work presented here were essential for the detector experts to locate the discrepancies on the detector material between real life and the implementation in GEANT simulations. Due to this common effort the systematic uncertainty could already be reduced to approximately $\pm 4\%$. This systematic uncertainty enters in nearly all physics analysis, as particles can be absorbed in the material, or their properties can be modified due to interactions with the material. Therefore the studies on the material budget will continue to decrease this systematic uncertainty even more. The results for $|\eta| < 1.4$ do not show yet the same precision because a lot of simplification and omissions were done in the implementation of the material. This region is important for the forward detectors in ALICE.

Additionally, in this thesis it was proved that the conversion method is a viable method in ALICE to study photon physics at the LHC. Therefore all physics analysis concerning photons can be performed with this method. The first attempts to do physics with the method were already undertaken and the first π^0 and η spectra could be extracted from the data by combining two photons from conversions. Furthermore, the work for extracting a direct photon spectrum has started.

For the future, I plan to reanalyze the data as soon as pass 2 of the reconstruction is available. Especially the photon characteristics need to be investigated for the new reconstruction to check the data quality. Afterwards we might have to tighten the χ^2 -cut on the conversion photon and use the cut on the TPC clusters requiring for example at least 70 clusters. This would improve the momentum resolution of the single tracks. Additionally, we will check the influence of cut on the invariant mass of the electrons and the positrons at 10 MeV and a q_T cut at 0.025 to remove the not yet understood structure in the Armenteros-Podolanski-Plot directly above the γ -distribution. Furthermore, the first tests for using a different technique of recalculating the photon conversion point were carried out. This technique will calculate the conversion point with the helix-center but will update the momentum vector as well. It is provided by an update of the AliKF-package, but it is not yet fully tested.

For a better understanding of the resolution another iteration of the fitting will be necessary. This will be carried out with different fitting algorithms and different fitting functions, which should match the distributions better and not neglect the tails, and use the new AliKF-package.

Moreover, the studies towards a high p_t conversion trigger will continue. The next step is to estimate the bias of the momentum calculated at the trigger level due to the fact that the tracks do not come from the vertex. The final step then would be to implement a simulation of the trigger and check the expected trigger rates for the photon conversion trigger and the level of the fakes.

In the future the physics results obtained with the conversion method can be compared with the results obtained with calorimeters and will provide an independent measurement of the same physics observables.

A. Acronyms and Technical Terms

AGS	Alternating Gradient Synchrotron
ALICE	A Large Ion Collider Experiment
ATLAS	A Toroidal LHC Apparatus
BNL	Brockhaven National Laboratory
CERN	Conseil Européen pour la Recherche Nucléaire
CMS	Compact Muon Solenoid experiment
CTP	Central Trigger Processor
DAQ	Data Acquisition
DCA	Distance of closest approach
DCal	Di-jet Calorimeter
EMCal	Electromagnetic Calorimeter
FEE	Front End Electronics
FMD	Forward Multiplicity Detector
FPGA	Field Programmable Gate Array
GEANT	Geometry and Tracking Software
GTU	Global Tracking Unit
HG	Hadron Gas
HIJING	Heavy Ion Jet Interaction Generator
HLT	High Level Trigger
HMPID	High Momentum Particle Identification Detector
HYDJET	Monte Carlo event generator for heavy ion collisions
ITS	Inner Tracking System
L3	High Energy Physics Experiment at LEP
LEIR	Low Energy Ion Ring
LEP	Large Electron Positron Collider
LHC	Large Hadron Collider
LHCb	LHC beauty experiment
LINAC2/3	Linear Accelerator
LTU	Local Trigger Unit
MC	Monte Carlo simulation
MRPC	Multigap Resistive Plate Chamber
MWPC	Multi Wire Proportional Chamber
PDF	Parton distribution function
PHOS	Photon Spectrometer
RICH	Ring Imaging Cherenkov detector
PDG	Particle Data Group
PID	Particle Identification
PS	Proton Synchrotron
PSB	Proton Synchrotron Booster
PYQUEN	Monte Carlo event generator for pp-collisions
PYTHIA	Monte Carlo event generator for pp-collisions
QCD	Quantum Chromodynamics
QFT	Quantum Field Theory
QGP	Quark Gluon Plasma

RHIC	Relativistic Heavy Ion Collider
SDD	Silicon Drift Detector
SPD	Silicon Pixel Detector
SPS	Super Proton Synchrotron
SSD	Silicon Strip Detector
T0	Timing and Trigger detector at ALICE
TOF	Time-Of-Flight detector
TPC	Time Projection Chamber
TR	Transition Radiation
TRD	Transition Radiation
TRG	Trigger System
V0	Unknown Particle
ZDC	Zero Degree Calorimeter
ZEM	Zero Degree Electromagnetic Calorimeter
ZN	Zero Degree Neutron Calorimeter
ZP	Zero Degree Proton Calorimeter

B. Mapping Figures of the different Detectors only V0 finder

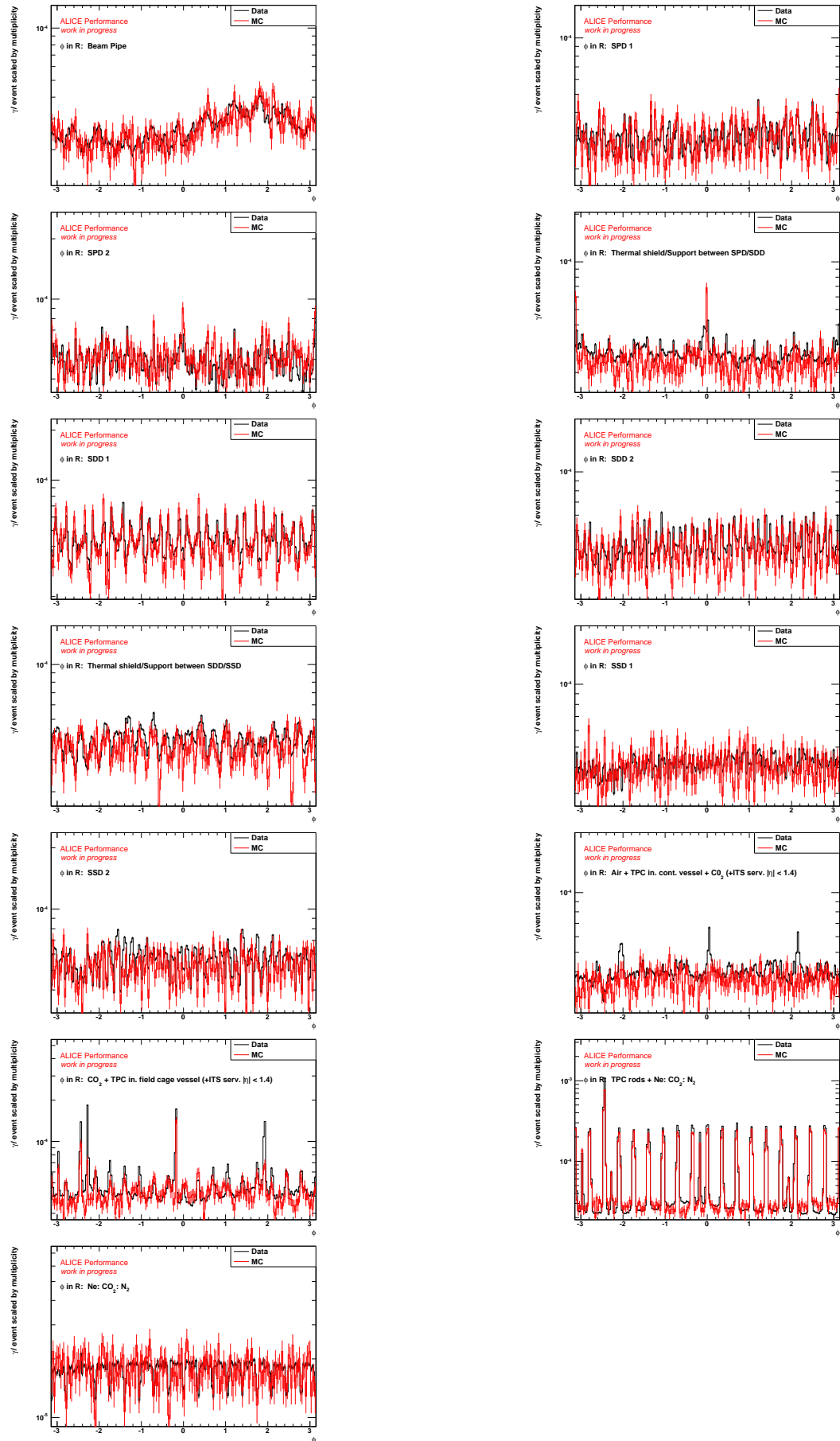


Figure B.1.: ϕ -distribution in R -bins for the onfly V0 finder obtained with the Monte Carlo Production of iteration 2.

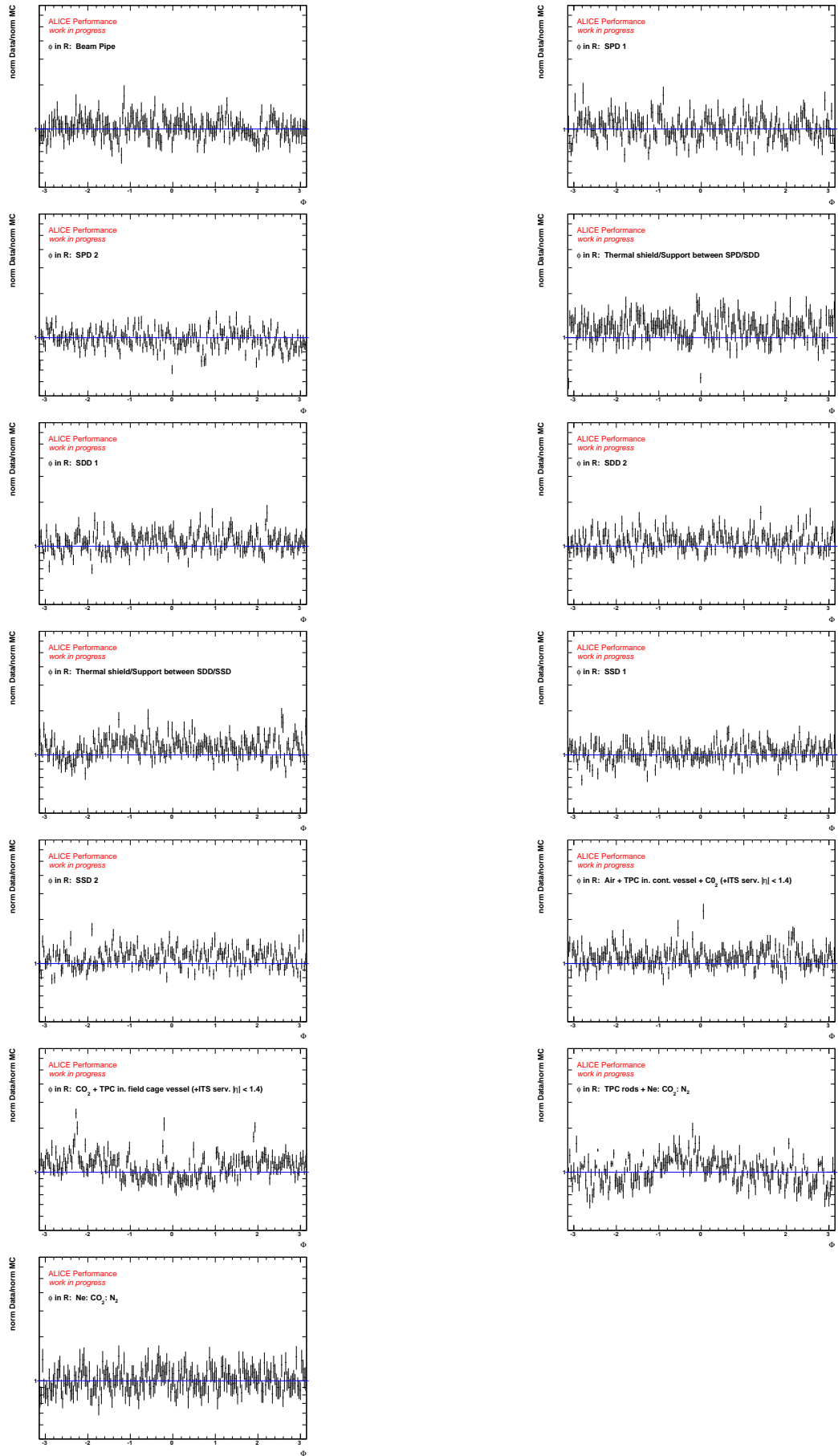


Figure B.2.: Ratio plots for ϕ -distribution in R -bins for the onfly V0 finder obtained with the Monte Carlo Production of iteration 2.

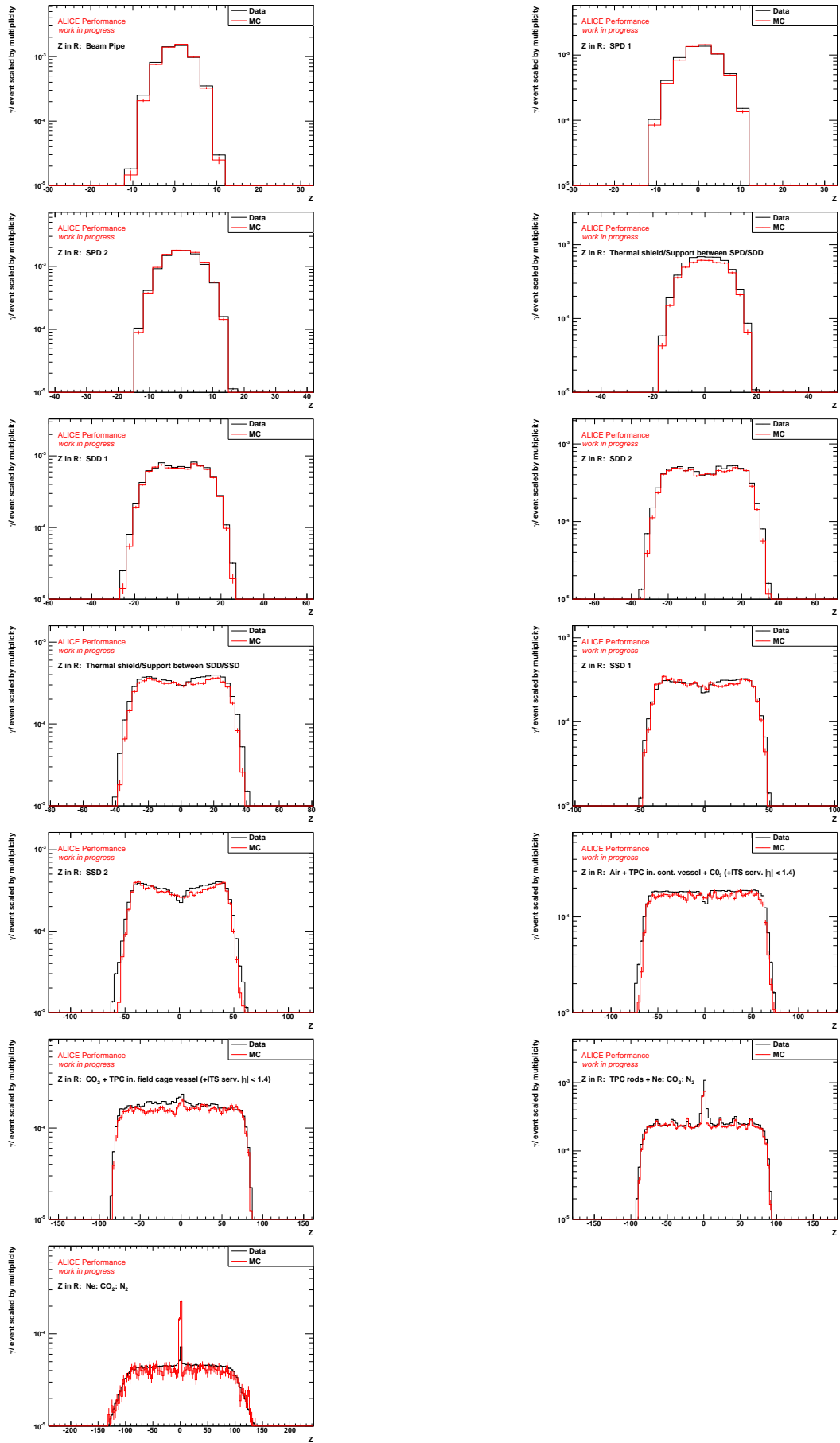


Figure B.3.: Z-distribtion in R -bins for the onfly V0 finder obtained with the Monte Carlo Production of iteration 2.

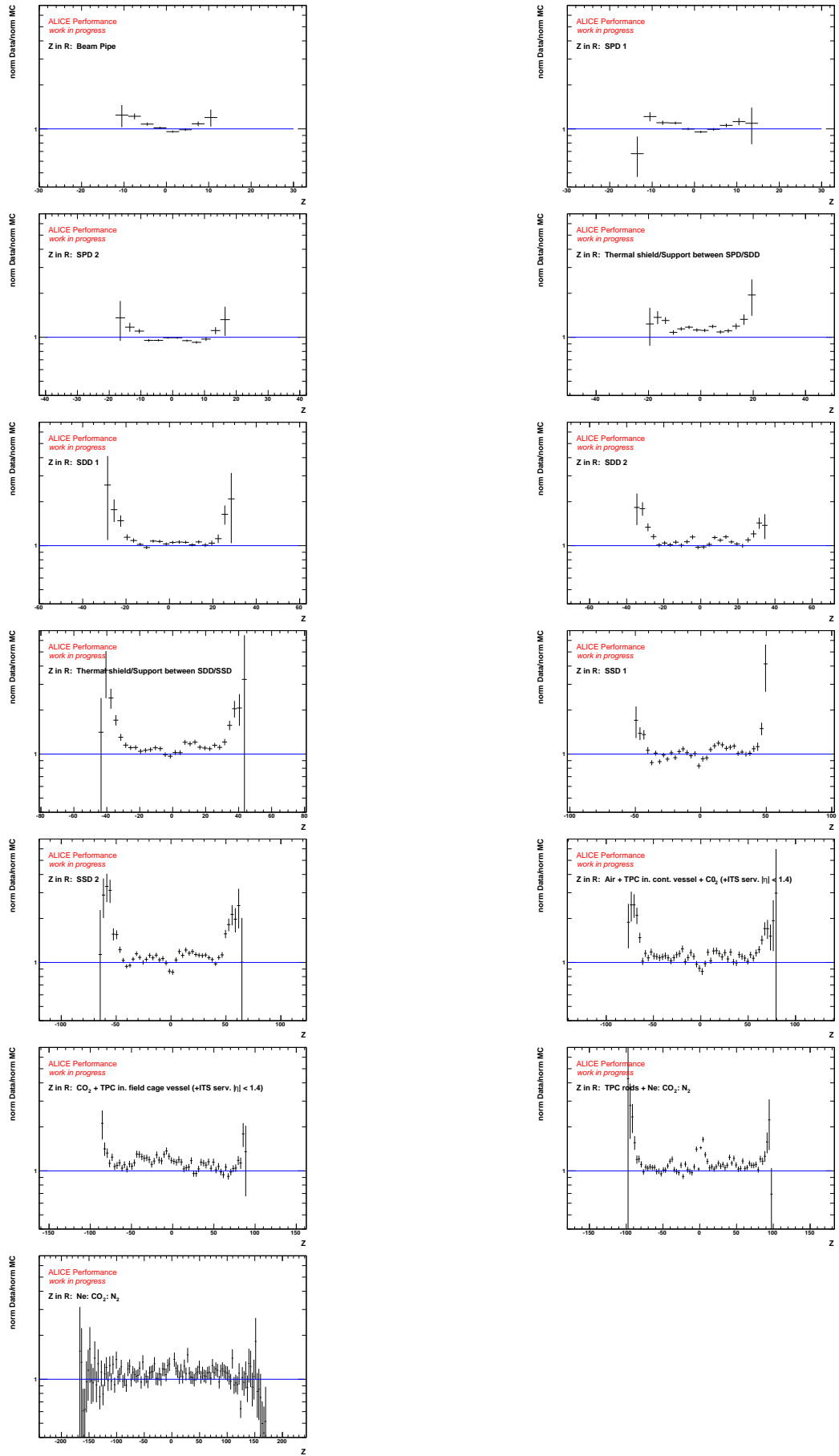


Figure B.4.: Ratio plots for Z -distribution in R -bins for the only V0 finder obtained with the Monte Carlo Production of iteration 2.

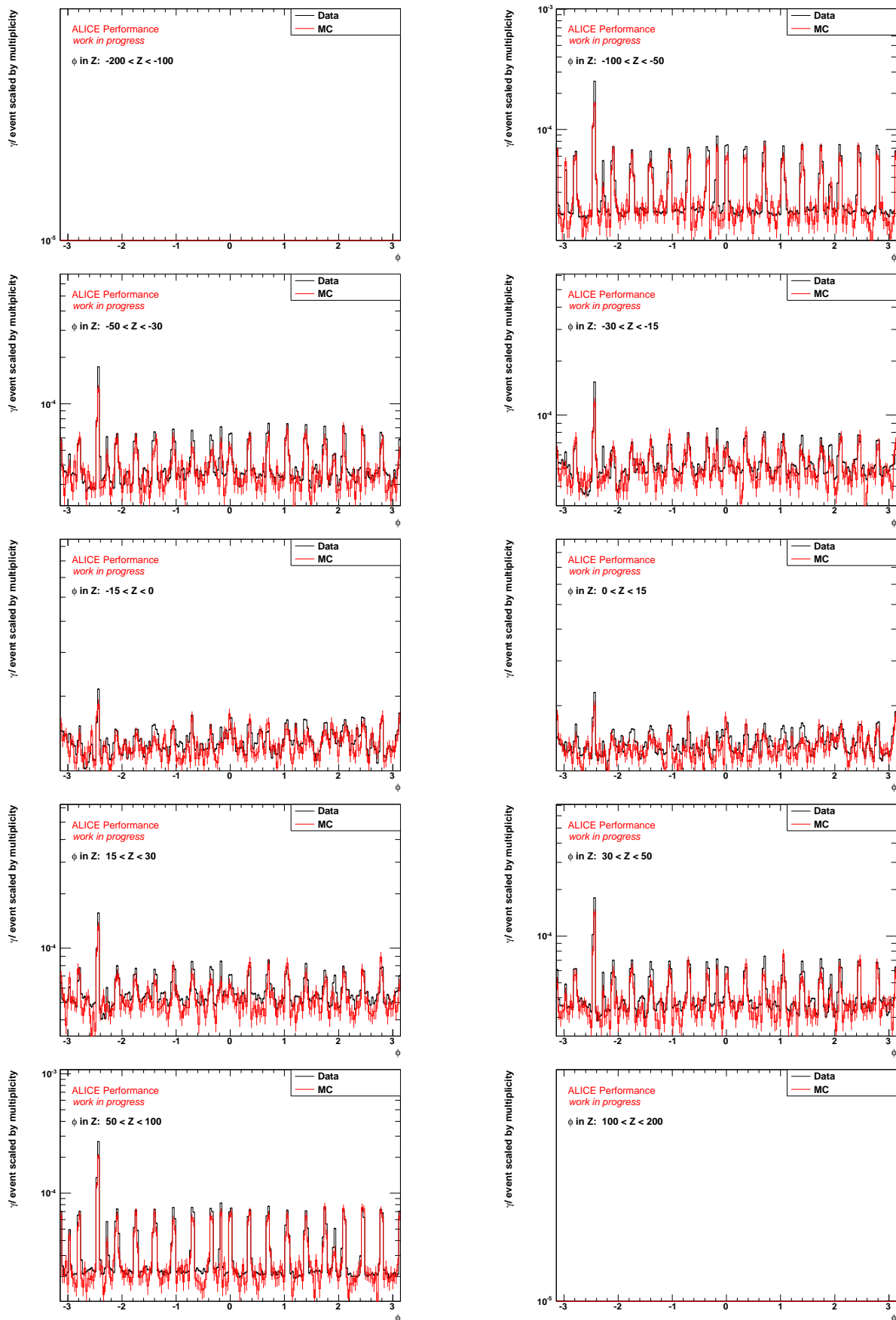


Figure B.5.: ϕ -distribution in Z -bins for the onfly V0 finder obtained with the Monte Carlo Production of iteration 2, empty bins were left out.

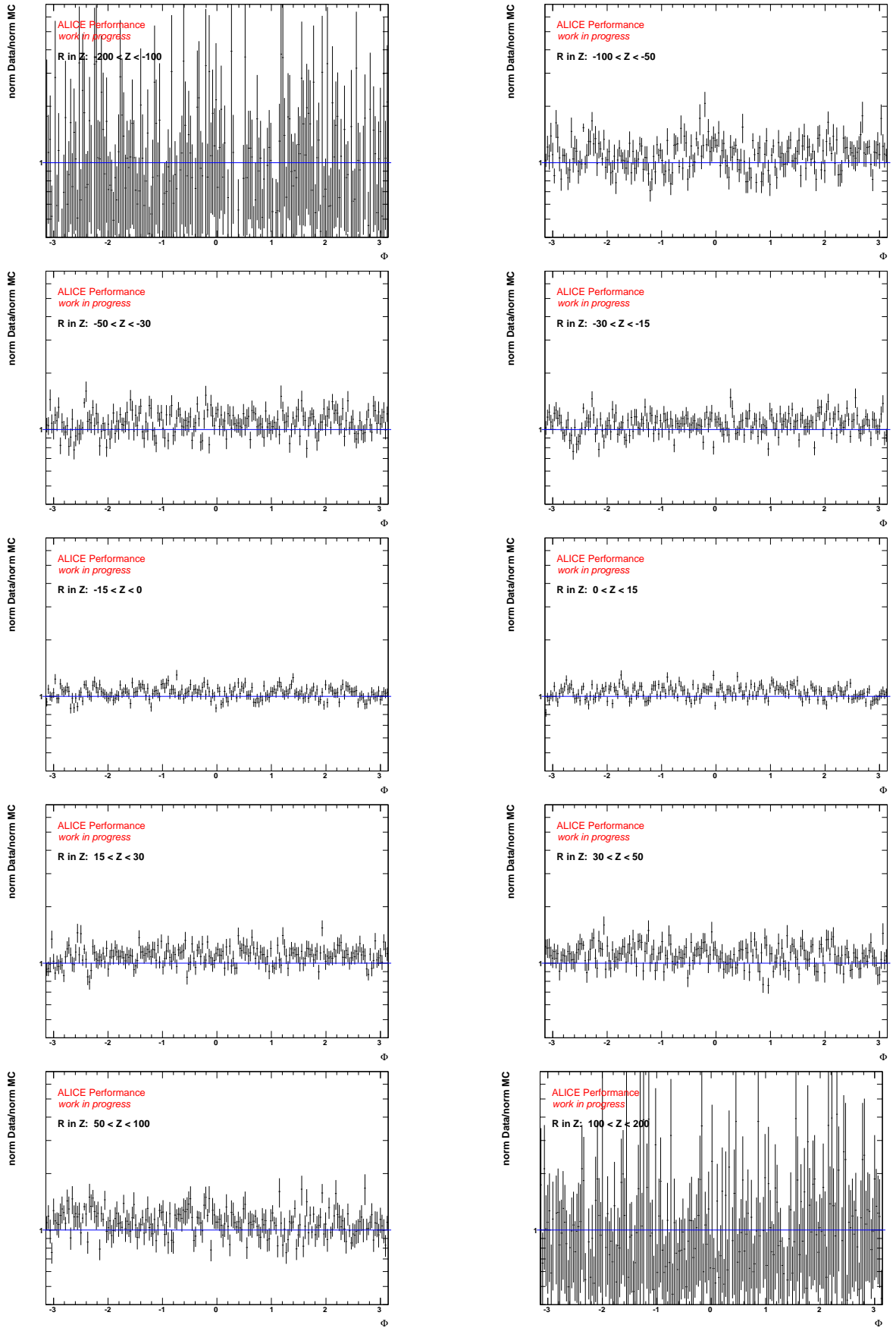


Figure B.6.: Ratio of the ϕ -distribution in Z -bins for the onfly V0 finder obtained with the Monte Carlo Production of iteration 2, empty bins were left out.

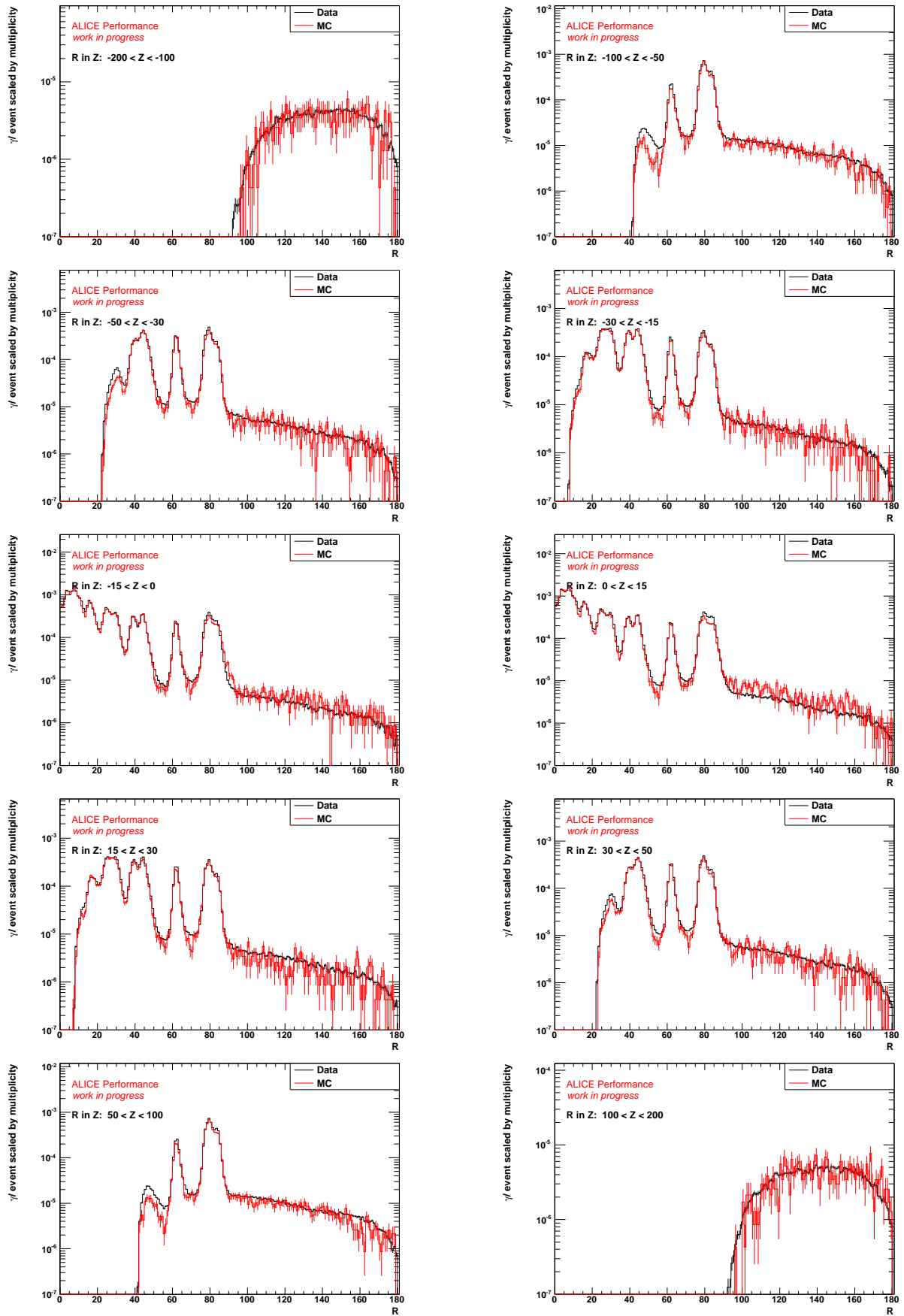


Figure B.7.: R -distribution in Z -bins for the only V0 finder obtained with the Monte Carlo Production of iteration 2, empty bins were left out.

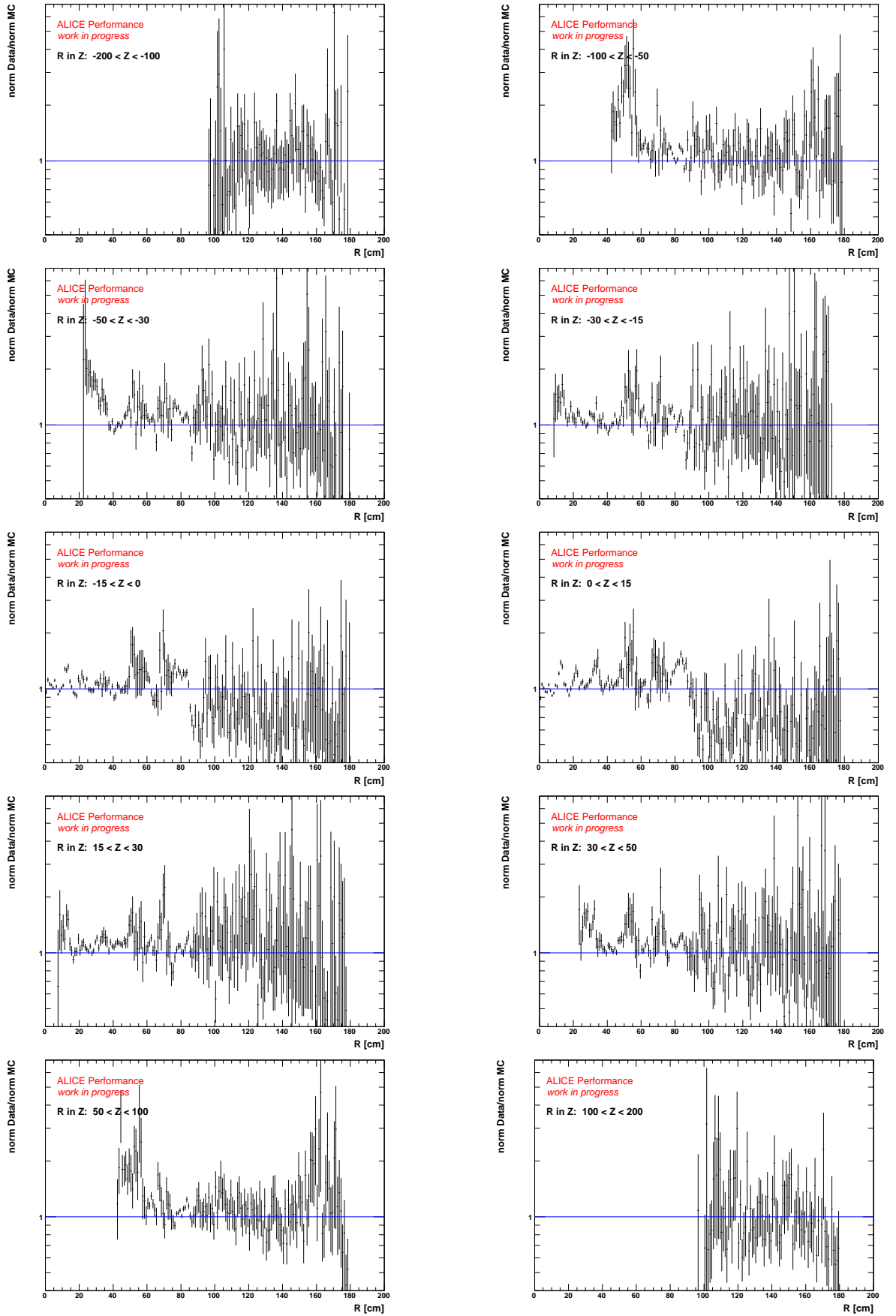


Figure B.8.: Ratio of the R -distribution in Z -bins for the onfly V0 finder obtained with the Monte Carlo Production of iteration 2, empty bins were left out.

C. Mapping Figures of the different Detectors offline V0 finder

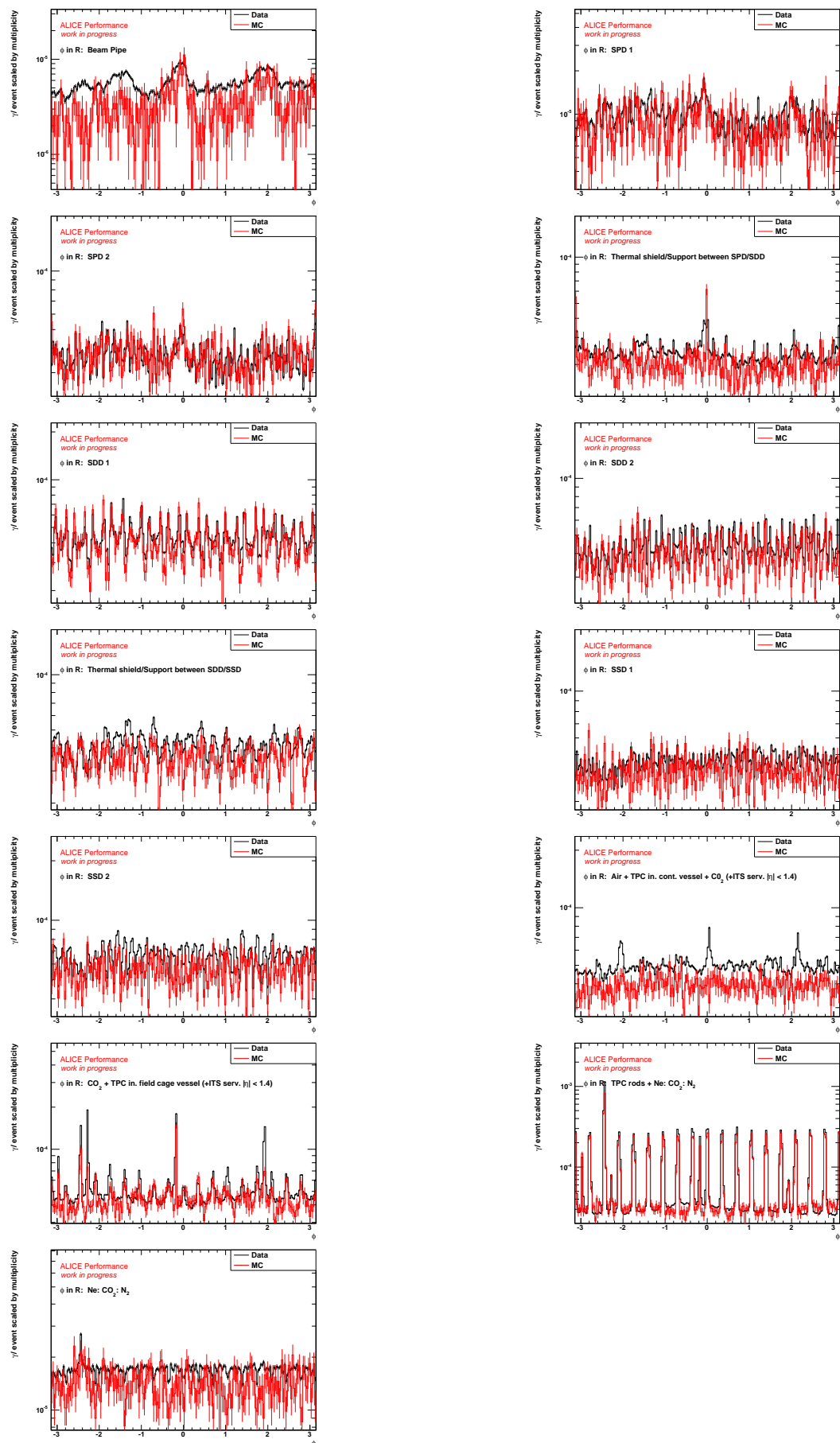


Figure C.1.: ϕ -distribution in R -bins for the offline V0 finder obtained with the Monte Carlo Production of iteration 2.

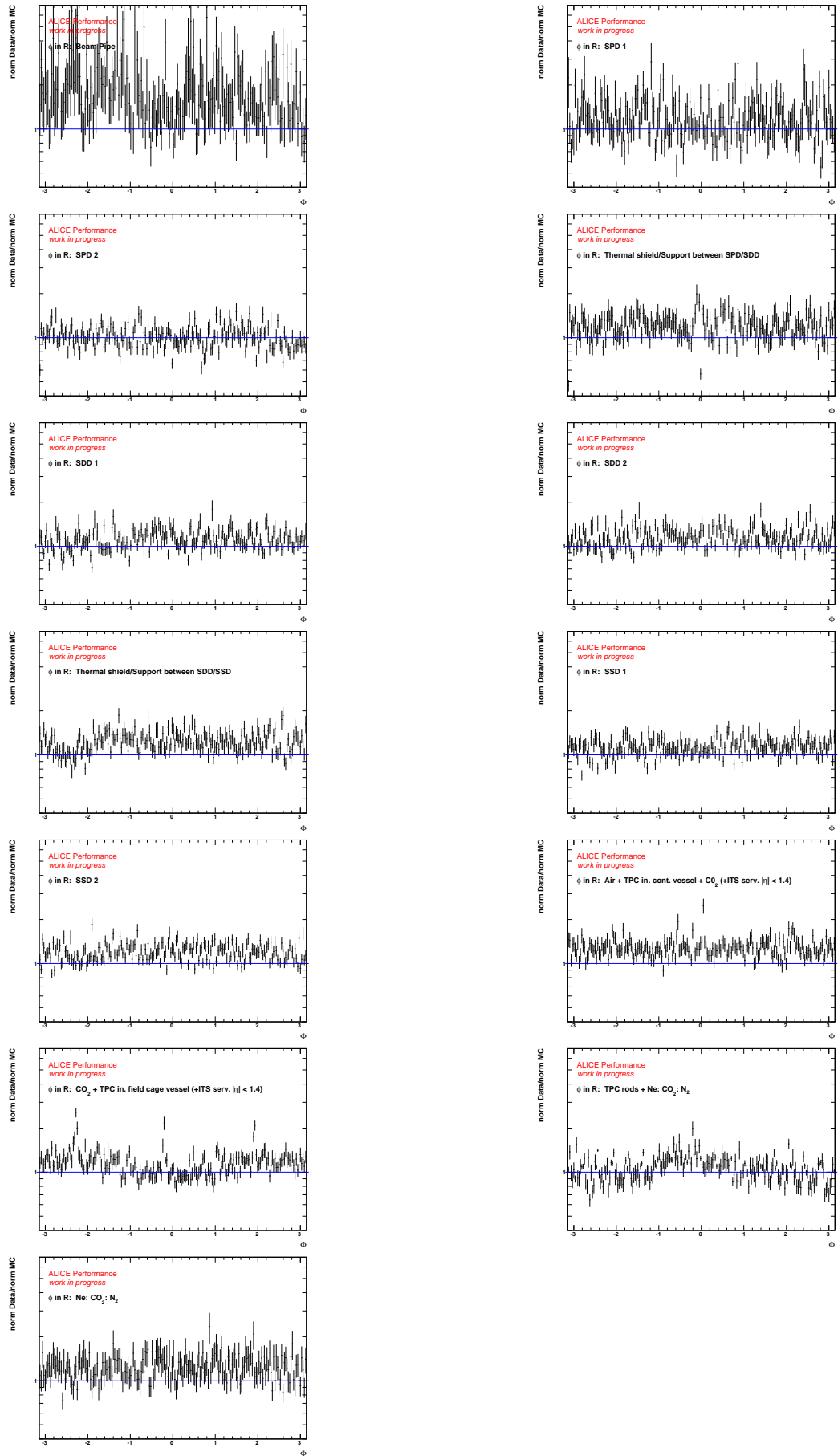


Figure C.2.: Ratio plots for ϕ -distribution in R -bins for the offline V0 finder obtained with the Monte Carlo Production of iteration 2.

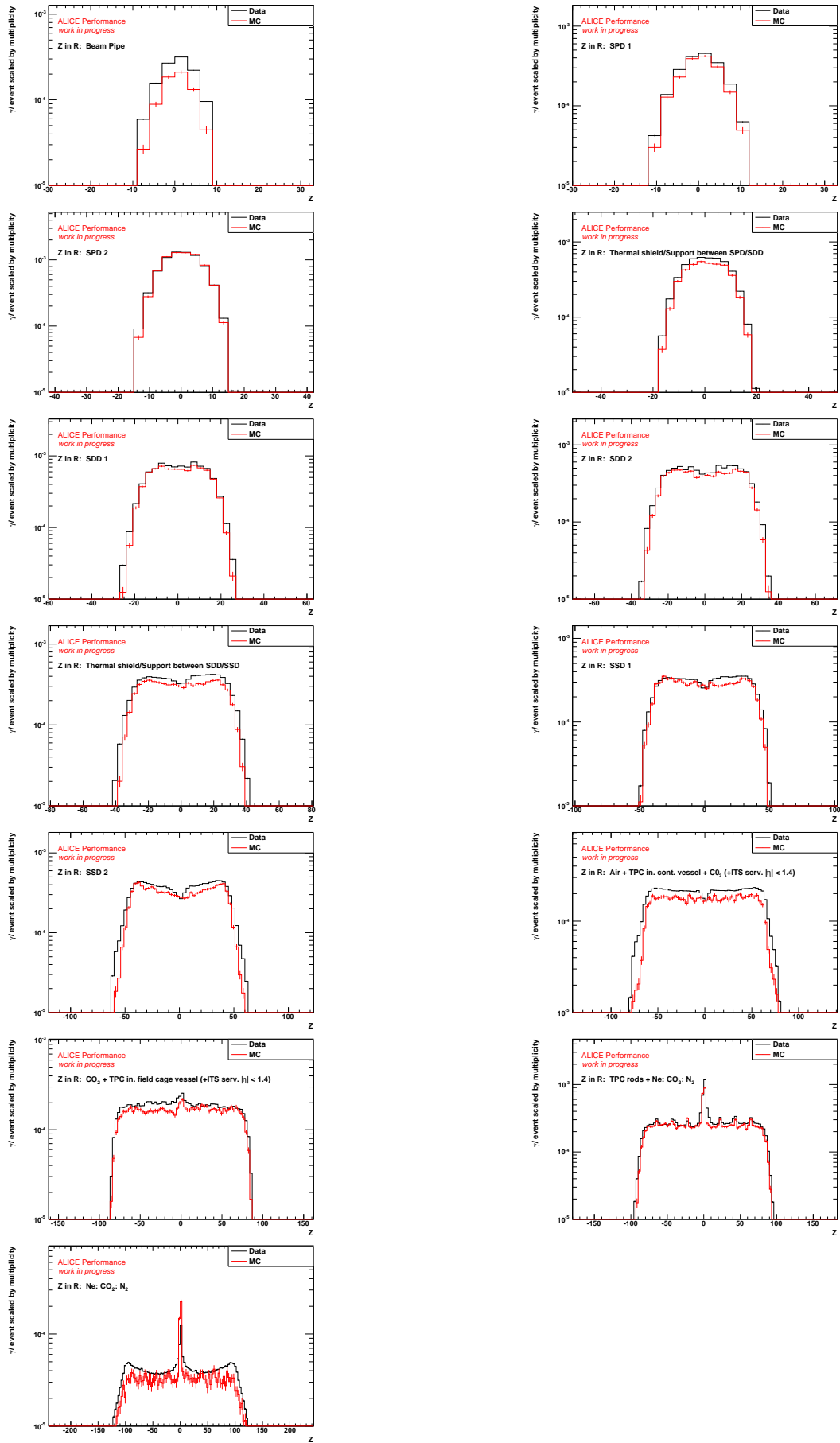


Figure C.3.: Z -distribtion in R -bins for the offline V0 finder obtained with the Monte Carlo Production of iteration 2.

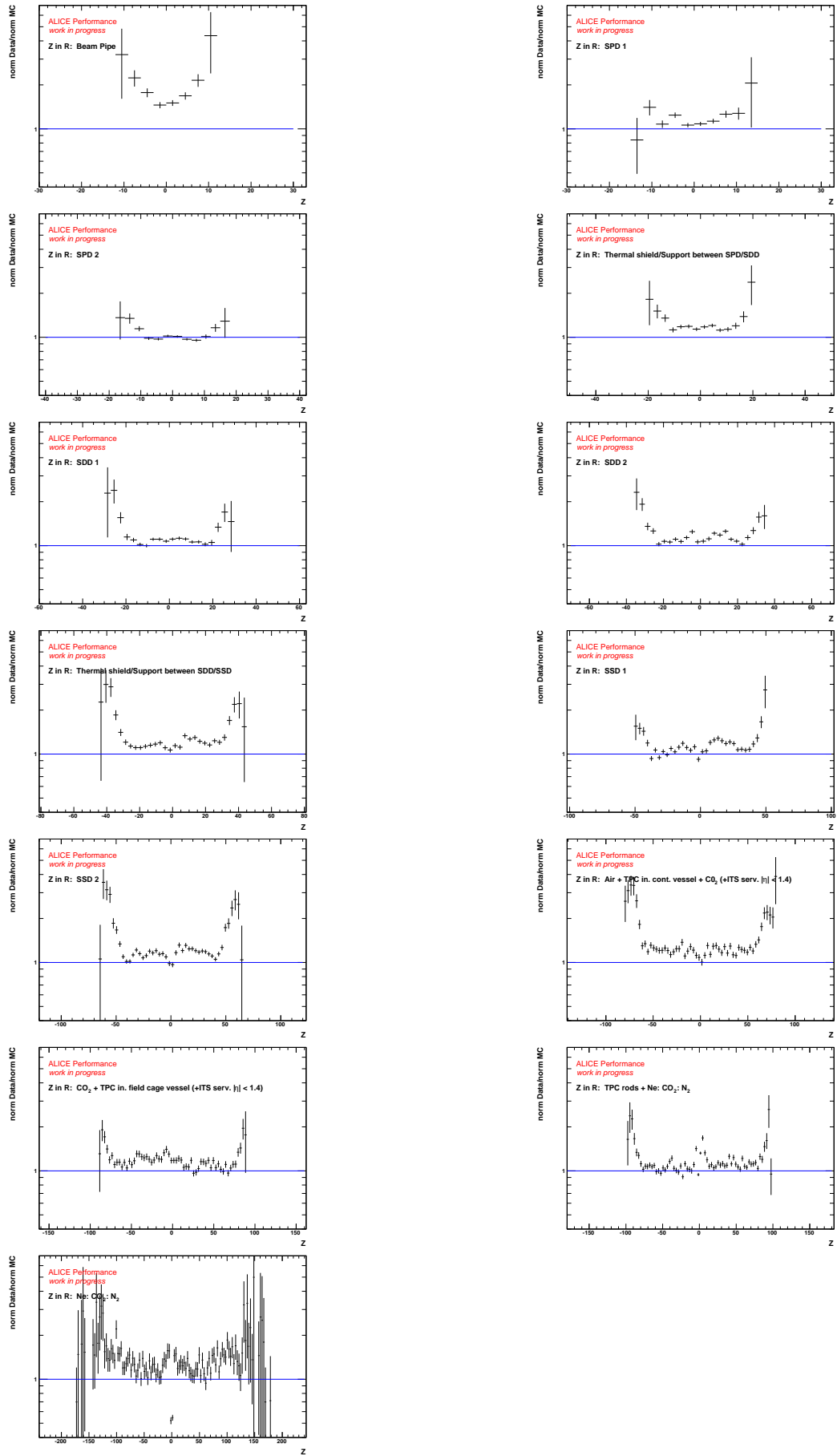


Figure C.4.: Ratio plots for Z -distribution in R -bins for the offline V0 finder obtained with the Monte Carlo Production of iteration 2.

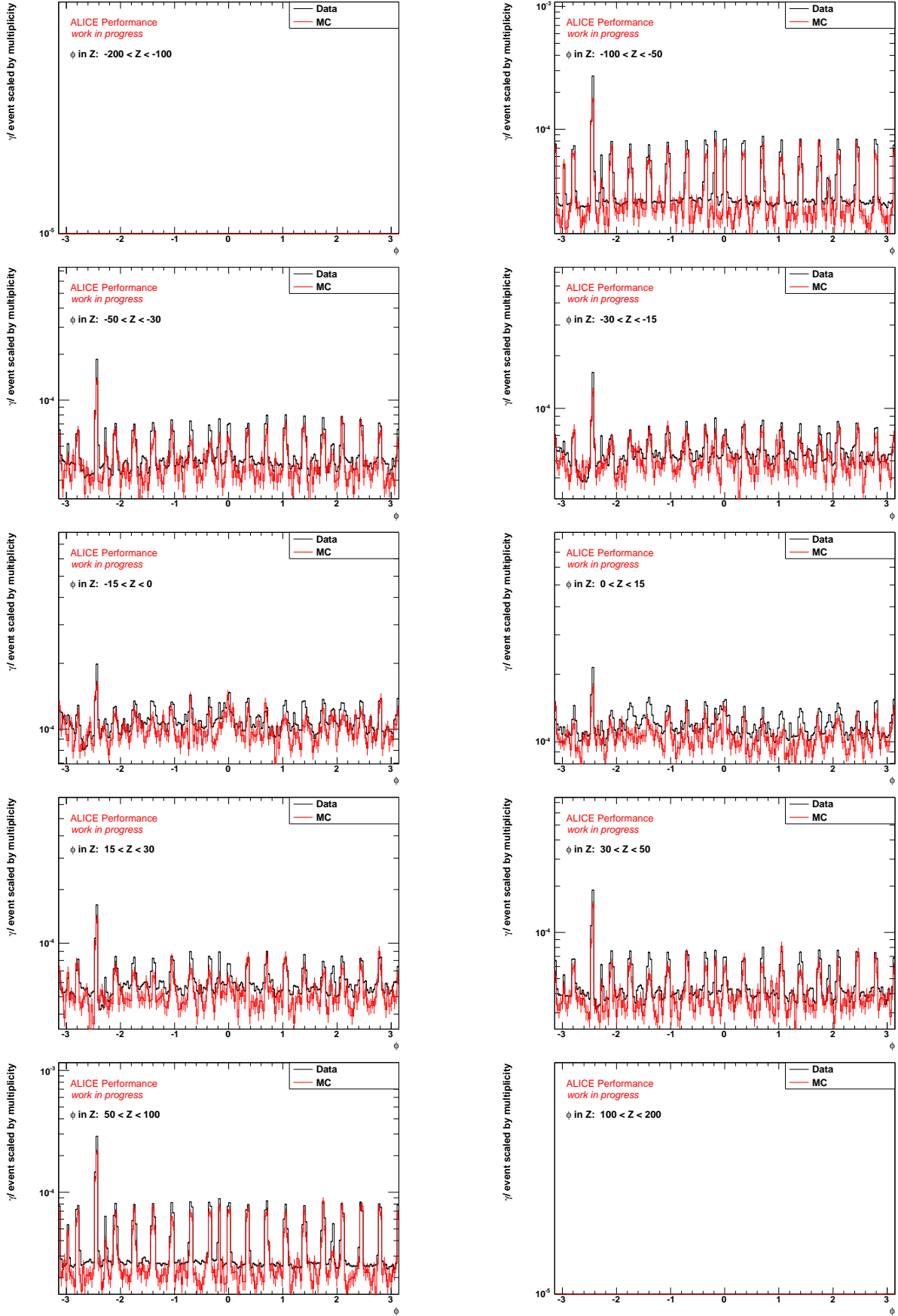


Figure C.5.: ϕ -distribution in Z -bins for the offline V0 finder obtained with the Monte Carlo Production of iteration 2, empty bins were left out.

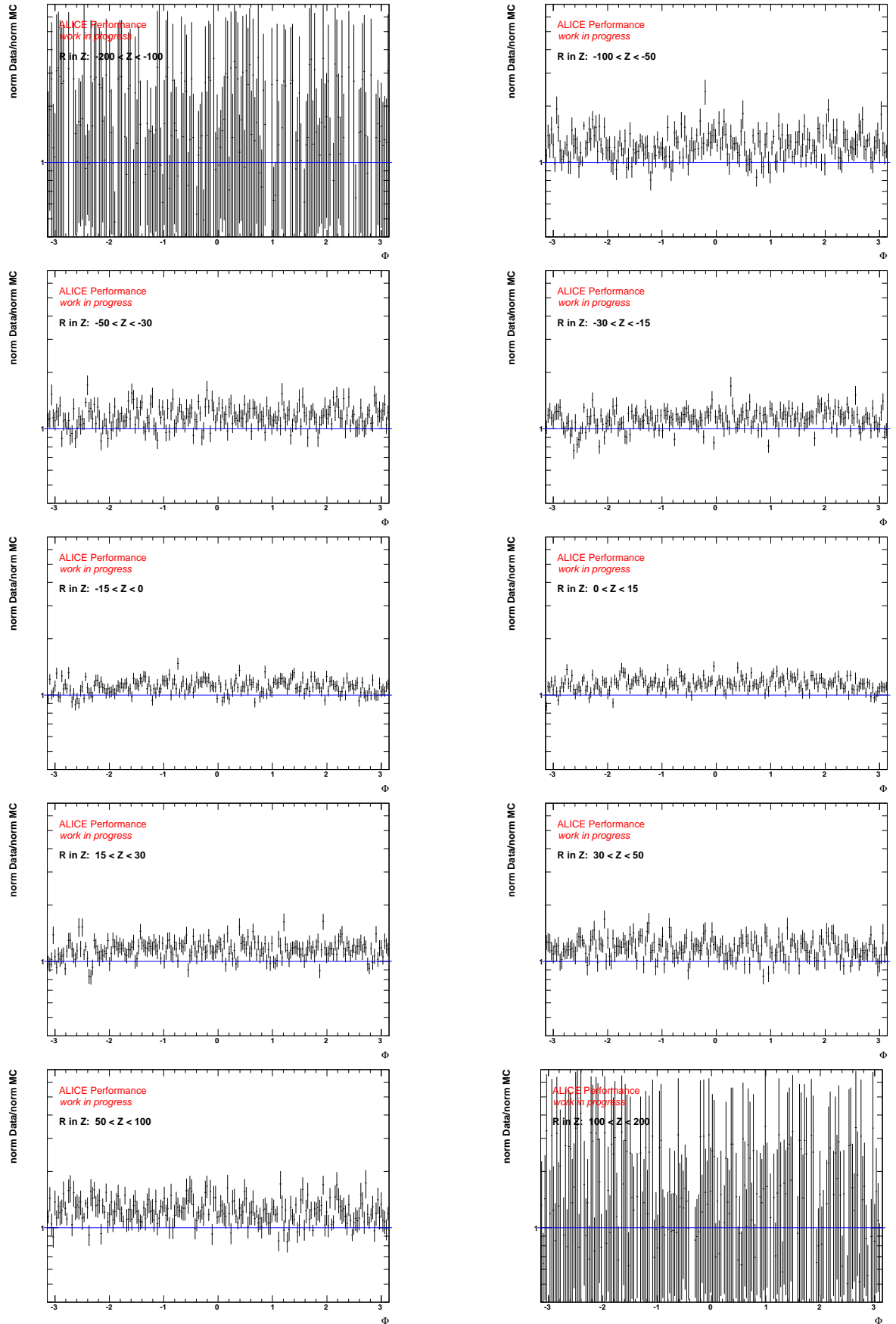


Figure C.6.: Ratio of the ϕ -distribution in Z -bins for the offline V0 finder obtained with the Monte Carlo Production of iteration 2, empty bins were left out.

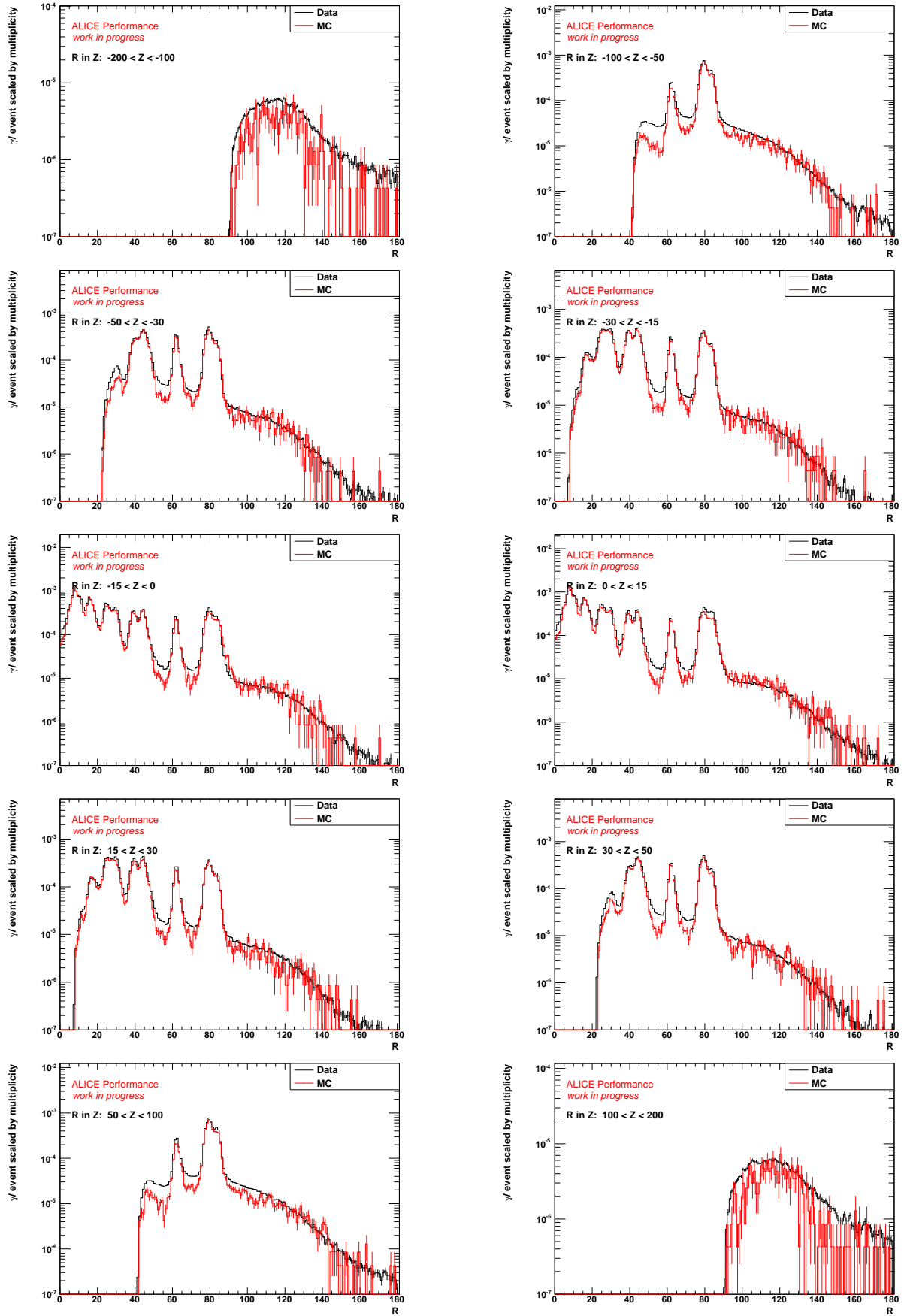


Figure C.7.: R -distribution in Z -bins for the offline V0 finder obtained with the Monte Carlo Production of iteration 2, empty bins were left out.

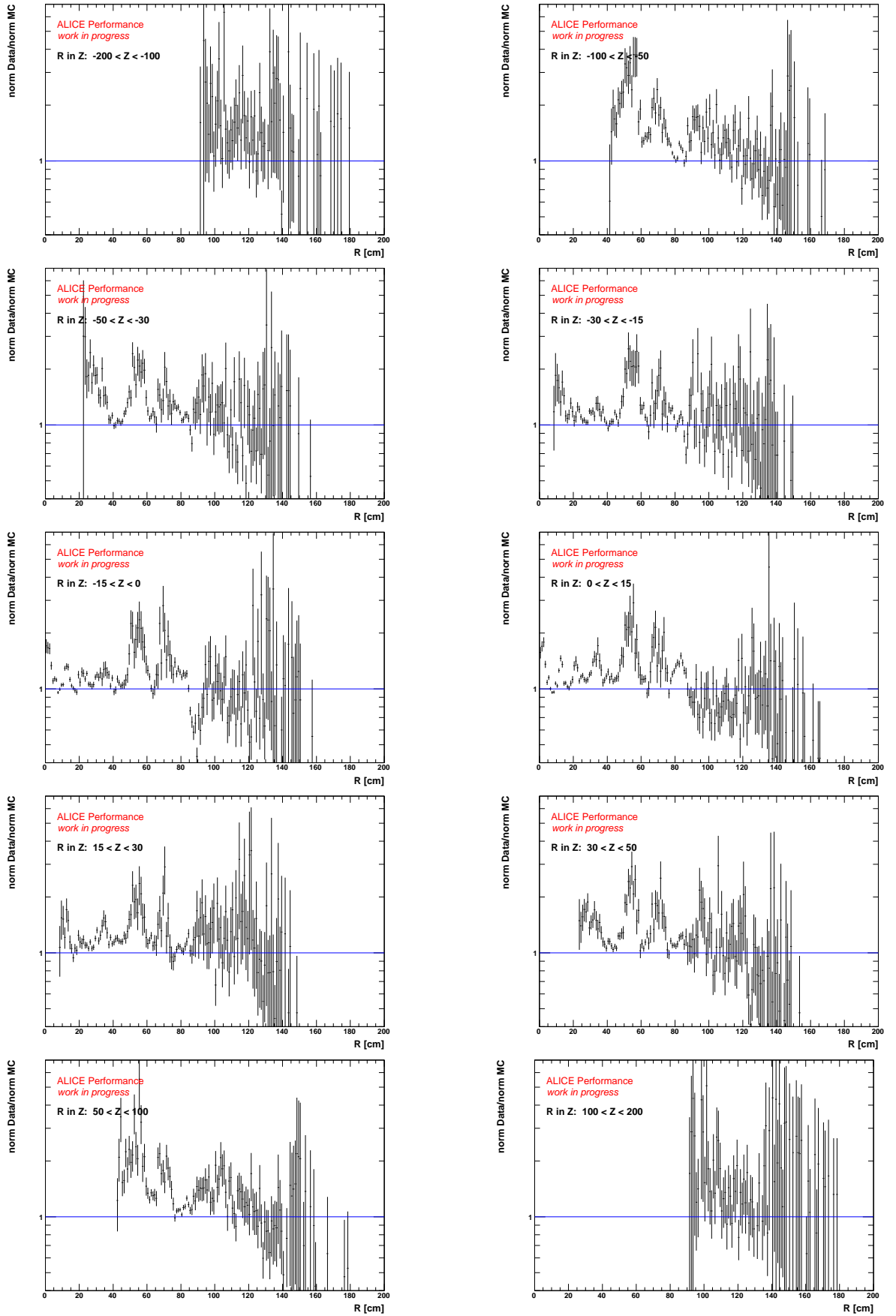


Figure C.8.: Ratio of the R -distribution in Z -bins for the offline V0 finder obtained with the Monte Carlo Production of iteration 2, empty bins were left out.

D. Tables

applied cut	
V0 finder	onfly V0 finder or offline V0 finder
Number of contributors	≥ 1
dE/dx electron line	$dE/dx_{e-line} + 3\sigma < dE/dx_{meas} < dE/dx_{e-line} + 5\sigma$
dE/dx pion line	$dE/dx_{meas} > dE/dx_{\pi-line} + 1\sigma$ for $p > 0.5$ GeV
Kaon rejection low p	$dE/dx_{meas} > dE/dx_{K-line} + 1\sigma$ or $dE/dx_{meas} < dE/dx_{K-line} - 1\sigma$ in line crossing area
Proton rejection low p	$dE/dx_{meas} > dE/dx_{p-line} + 1\sigma$ or $dE/dx_{meas} < dE/dx_{p-line} - 1\sigma$ in line crossing area
Pion rejection low p	$dE/dx_{meas} > dE/dx_{\pi-line} + 1\sigma$ or $dE/dx_{meas} < dE/dx_{\pi-line} - 1\sigma$ in line crossing area
PID prob electron	$P(e) > 0$
R	$R < 180$ cm
Z	$ Z < 240$ cm
pseudo rapidity	$ \eta < 0.9$ or < 1.4
Minimum number TPC clusters	$N_{TPCcls} > 0$
Single p_t electron	$p_{t,e} > 0.020$ GeV
χ^2/NDF γ	$\chi^2 < 30$
p_t γ	$p_{t,\gamma} > 0.02$ GeV

Table D.1.: Cuts used for the analysis in this thesis.

The following tables show the R -bin number (column 1), the number of photons per event in a given R bin (column 2,4) and the relative contribution of the given bin for data and Monte Carlo (column 3, 5). The absolute (column 6) and relative (column 7) differences are also given.

bin	data	%	MC	%	data-MC	%
0	0.00066	0.96	0.00053	0.75	0.00013	24.66
1	0.00146	2.11	0.00146	2.05	0.00001	0.35
2	0.00624	9.02	0.00633	8.92	-0.00009	-1.49
3	0.00368	5.32	0.00335	4.72	0.00033	9.87
4	0.00564	8.15	0.00598	8.42	-0.00034	-5.64
5	0.00441	6.37	0.00485	6.84	-0.00044	-9.11
6	0.00345	4.98	0.00323	4.55	0.00022	6.68
7	0.00511	7.38	0.00506	7.13	0.00005	0.93
8	0.00721	10.41	0.00680	9.57	0.00041	6.03
9	0.00666	9.62	0.00702	9.89	-0.00036	-5.15
10	0.00882	12.75	0.00938	13.21	-0.00056	-5.96
11	0.01408	20.34	0.01473	20.75	-0.00065	-4.43
12	0.00179	2.59	0.00227	3.20	-0.00048	-20.97
sum	0.06920	100.00	0.07098	100.00	-0.00178	-2.51

Table D.2.: Deviation for the Offline V0 finder and Phojet (ite 1)- ϕ in R in the several R bins.

bin	data	%	MC	%	data-MC	%
0	0.00066	0.96	0.00054	0.75	0.00012	22.13
1	0.00146	2.11	0.00143	1.98	0.00003	2.31
2	0.00624	9.02	0.00642	8.91	-0.00018	-2.75
3	0.00368	5.32	0.00345	4.79	0.00023	6.65
4	0.00564	8.15	0.00613	8.52	-0.00049	-8.05
5	0.00441	6.37	0.00514	7.14	-0.00073	-14.28
6	0.00345	4.98	0.00339	4.71	0.00005	1.52
7	0.00511	7.38	0.00521	7.23	-0.00010	-1.93
8	0.00721	10.41	0.00707	9.82	0.00013	1.87
9	0.00666	9.62	0.00719	9.98	-0.00053	-7.37
10	0.00882	12.75	0.00942	13.08	-0.00059	-6.31
11	0.01408	20.34	0.01445	20.06	-0.00037	-2.56
12	0.00179	2.59	0.00217	3.01	-0.00038	-17.30
sum	0.06920	100.00	0.07200	100.00	-0.00281	-3.90

Table D.3.: Deviation for the Offline V0 finder and Pythia Perugia - 0 (ite 1) - ϕ in R in the several R bins.

bin	data	%	MC	%	data-MC	%
0	0.00486	4.78	0.00552	5.38	-0.00066	-11.94
1	0.00534	5.26	0.00569	5.54	-0.00034	-6.06
2	0.00919	9.04	0.00964	9.40	-0.00045	-4.64
3	0.00496	4.89	0.00460	4.48	0.00037	7.98
4	0.00846	8.33	0.00866	8.45	-0.00020	-2.31
5	0.00831	8.17	0.00827	8.06	0.00004	0.45
6	0.00763	7.51	0.00656	6.39	0.00107	16.34
7	0.00793	7.81	0.00758	7.39	0.00036	4.70
8	0.01058	10.41	0.00988	9.63	0.00070	7.10
9	0.00735	7.24	0.00777	7.58	-0.00042	-5.41
10	0.00902	8.88	0.00947	9.23	-0.00045	-4.71
11	0.01469	14.46	0.01491	14.53	-0.00022	-1.45
12	0.00327	3.22	0.00402	3.92	-0.00075	-18.74
sum	0.10160	100.00	0.10255	100.00	-0.00095	-0.93

Table D.4.: Deviation for the Onfly V0 finder and Phojet (ite 1) - ϕ in R in the several R bins.

bin	data	%	MC	%	data-MC	%
0	0.00486	4.78	0.00573	5.47	-0.00087	-15.22
1	0.00534	5.26	0.00592	5.66	-0.00058	-9.78
2	0.00919	9.04	0.01003	9.59	-0.00084	-8.42
3	0.00496	4.89	0.00483	4.61	0.00014	2.88
4	0.00846	8.33	0.00904	8.63	-0.00057	-6.35
5	0.00831	8.17	0.00869	8.30	-0.00039	-4.43
6	0.00763	7.51	0.00673	6.43	0.00089	13.29
7	0.00793	7.81	0.00783	7.48	0.00010	1.29
8	0.01058	10.41	0.01012	9.67	0.00046	4.55
9	0.00735	7.24	0.00791	7.55	-0.00055	-7.00
10	0.00902	8.88	0.00951	9.08	-0.00048	-5.08
11	0.01469	14.46	0.01459	13.94	0.00009	0.65
12	0.00327	3.22	0.00374	3.58	-0.00048	-12.72
sum	0.10160	100.00	0.10468	100.00	-0.00308	-2.94

Table D.5.: Deviation for the Onfly V0 finder and Pythia Perugia - 0 (ite 1) - ϕ in R in the several R bins.

bin	data	%	MC	%	data-MC	%
0	0.00043	0.96	0.00033	0.74	0.00010	31.74
1	0.00095	2.09	0.00086	1.93	0.00009	10.05
2	0.00486	10.68	0.00467	10.44	0.00019	4.04
3	0.00292	6.43	0.00256	5.73	0.00036	13.95
4	0.00430	9.46	0.00440	9.84	-0.00010	-2.29
5	0.00343	7.55	0.00366	8.18	-0.00023	-6.21
6	0.00258	5.68	0.00242	5.40	0.00017	6.85
7	0.00377	8.30	0.00365	8.15	0.00013	3.48
8	0.00513	11.28	0.00469	10.48	0.00044	9.44
9	0.00413	9.10	0.00426	9.53	-0.00013	-3.01
10	0.00475	10.45	0.00489	10.94	-0.00014	-2.93
11	0.00720	15.84	0.00714	15.97	0.00006	0.84
12	0.00099	2.18	0.00119	2.65	-0.00019	-16.32
sum	0.04545	100.00	0.04471	100.00	0.00074	1.65

Table D.6.: Deviation for the Offline V0 finder and Phojet (ite 1) - ϕ in R in the several R bins in mid p_t .

bin	data	%	MC	%	data-MC	%
0	0.00043	0.96	0.00035	0.74	0.00009	25.72
1	0.00095	2.09	0.00087	1.86	0.00008	8.95
2	0.00486	10.68	0.00485	10.35	0.00001	0.22
3	0.00292	6.43	0.00267	5.71	0.00025	9.35
4	0.00430	9.46	0.00456	9.74	-0.00026	-5.63
5	0.00343	7.55	0.00392	8.37	-0.00049	-12.40
6	0.00258	5.68	0.00254	5.42	0.00004	1.68
7	0.00377	8.30	0.00380	8.13	-0.00003	-0.83
8	0.00513	11.28	0.00500	10.68	0.00013	2.65
9	0.00413	9.10	0.00447	9.56	-0.00034	-7.59
10	0.00475	10.45	0.00518	11.07	-0.00043	-8.30
11	0.00720	15.84	0.00741	15.83	-0.00021	-2.84
12	0.00099	2.18	0.00119	2.55	-0.00020	-16.71
sum	0.04545	100.00	0.04680	100.00	-0.00135	-2.89

Table D.7.: Deviation for the Offline V0 finder and Pythia Perugia - 0 (ite 1) - ϕ in R in the several R bins in mid p_t .

bin	data	%	MC	%	data-MC	%
0	0.00379	5.73	0.00401	6.32	-0.00022	-5.55
1	0.00416	6.29	0.00414	6.53	0.00002	0.45
2	0.00703	10.64	0.00690	10.87	0.00013	1.94
3	0.00379	5.73	0.00333	5.24	0.00046	13.89
4	0.00622	9.41	0.00607	9.56	0.00015	2.49
5	0.00594	8.99	0.00564	8.89	0.00030	5.35
6	0.00532	8.04	0.00448	7.05	0.00084	18.76
7	0.00536	8.11	0.00496	7.82	0.00040	8.02
8	0.00685	10.35	0.00613	9.65	0.00072	11.69
9	0.00427	6.45	0.00435	6.85	-0.00008	-1.89
10	0.00469	7.09	0.00476	7.50	-0.00007	-1.53
11	0.00704	10.64	0.00677	10.66	0.00027	3.99
12	0.00167	2.52	0.00195	3.07	-0.00028	-14.41
sum	0.06613	100.00	0.06349	100.00	0.00263	4.15

Table D.8.: Deviation for the Onfly V0 finder and Phojet (ite 1) - ϕ in R in the several R bins in mid p_t .

bin	data	%	MC	%	data-MC	%
0	0.00379	5.73	0.00422	6.31	-0.00043	-10.15
1	0.00416	6.29	0.00435	6.51	-0.00019	-4.40
2	0.00703	10.64	0.00726	10.86	-0.00023	-3.17
3	0.00379	5.73	0.00353	5.28	0.00026	7.26
4	0.00622	9.41	0.00643	9.61	-0.00020	-3.17
5	0.00594	8.99	0.00608	9.09	-0.00013	-2.19
6	0.00532	8.04	0.00466	6.96	0.00066	14.18
7	0.00536	8.11	0.00521	7.80	0.00015	2.81
8	0.00685	10.35	0.00654	9.77	0.00031	4.73
9	0.00427	6.45	0.00457	6.84	-0.00031	-6.74
10	0.00469	7.09	0.00506	7.57	-0.00037	-7.30
11	0.00704	10.64	0.00706	10.55	-0.00002	-0.27
12	0.00167	2.52	0.00191	2.85	-0.00024	-12.54
sum	0.06613	100.00	0.06687	100.00	-0.00075	-1.12

Table D.9.: Deviation for the Onfly V0 finder and Pythia Perugia - 0 (ite 1) - ϕ in R in the several R bins in mid p_t .

bin	data	%	MC	%	data-MC	%
0	0.00113	1.08	0.00069	0.76	0.00044	64.24
1	0.00194	1.85	0.00171	1.88	0.00023	13.37
2	0.00733	7.00	0.00732	8.03	0.00001	0.17
3	0.00479	4.58	0.00408	4.47	0.00072	17.57
4	0.00877	8.38	0.00807	8.87	0.00069	8.59
5	0.00885	8.46	0.00781	8.57	0.00104	13.38
6	0.00840	8.03	0.00695	7.63	0.00145	20.88
7	0.00929	8.88	0.00836	9.18	0.00093	11.15
8	0.01318	12.60	0.01112	12.21	0.00206	18.52
9	0.00994	9.50	0.00783	8.60	0.00210	26.83
10	0.01044	9.98	0.00901	9.90	0.00143	15.84
11	0.01719	16.42	0.01532	16.82	0.00187	12.22
12	0.00340	3.25	0.00281	3.08	0.00059	20.97
sum	0.10464	100.00	0.09107	100.00	0.01357	14.90

Table D.10.: Deviation for the Offline V0 finder and Pythia (ite 2) - ϕ in R in the several R bins.

bin	data	%	MC	%	data-MC	%
0	0.00534	4.93	0.00527	5.20	0.00001	1.52
1	0.00586	5.41	0.00576	5.69	0.00010	1.70
2	0.00988	9.12	0.01015	10.02	-0.00027	-2.64
3	0.00535	4.93	0.00468	4.62	0.00067	14.27
4	0.00887	8.18	0.00845	8.34	0.00042	4.94
5	0.00855	7.89	0.00801	7.90	0.00054	6.75
6	0.00777	7.17	0.00693	6.84	0.00084	12.16
7	0.00832	7.67	0.00810	7.99	0.00022	2.72
8	0.01132	10.45	0.01037	10.24	0.00095	9.15
9	0.00803	7.41	0.00723	7.14	0.00080	11.08
10	0.00966	8.91	0.00859	8.48	0.00107	12.43
11	0.01588	14.66	0.01430	14.11	0.00158	11.05
12	0.00353	3.25	0.00350	3.46	0.00002	0.71
sum	0.10835	100.00	0.10133	100.00	0.00702	6.93

Table D.11.: Deviation for the Onfly V0 finder and Pythia (ite 2) - ϕ in R in the several R bins.

bin	data	%	MC	%	data-MC	%
0	0.00067	1.05	0.00041	0.72	0.00026	62.38
1	0.00120	1.87	0.00105	1.82	0.00015	14.14
2	0.00542	8.48	0.00548	9.50	-0.00006	-1.18
3	0.00355	5.55	0.00302	5.24	0.00052	17.32
4	0.00621	9.72	0.00586	10.15	0.00036	6.11
5	0.00622	9.73	0.00562	9.74	0.00060	10.68
6	0.00569	8.91	0.00487	8.44	0.00082	16.84
7	0.00616	9.65	0.00572	9.92	0.00044	7.77
8	0.00823	12.88	0.00727	12.60	0.00096	13.19
9	0.00540	8.46	0.00461	7.99	0.00079	17.25
10	0.00535	8.38	0.00485	8.40	0.00051	10.45
11	0.00823	12.88	0.00761	13.19	0.00062	8.13
12	0.00156	2.44	0.00133	2.30	0.00023	17.64
sum	0.06388	100.00	0.05769	100.00	0.00620	10.75

Table D.12.: Deviation for the Offline V0 finder and Pythia (ite 2) - ϕ in R in the several R bins in mid p_t .

bin	data	%	MC	%	data-MC	%
0	0.00402	5.81	0.00389	6.00	0.00013	3.41
1	0.00442	6.38	0.00423	6.53	0.00019	4.45
2	0.00734	10.60	0.00741	11.45	-0.00008	-1.02
3	0.00397	5.73	0.00338	5.21	0.00059	17.50
4	0.00638	9.22	0.00597	9.21	0.00041	6.92
5	0.00606	8.75	0.00562	8.67	0.00044	7.83
6	0.00537	7.76	0.00475	7.33	0.00062	13.13
7	0.00558	8.06	0.00540	8.34	0.00018	3.28
8	0.00727	10.51	0.00666	10.29	0.00061	9.17
9	0.00459	6.63	0.00423	6.53	0.00036	8.43
10	0.00495	7.15	0.00457	7.05	0.00038	8.42
11	0.00750	10.83	0.00692	10.68	0.00058	8.40
12	0.00177	2.56	0.00176	2.71	0.00001	0.76
sum	0.06922	100.00	0.06478	100.00	0.00444	6.85

Table D.13.: Deviation for the Onfly V0 finder and Pythia (ite 2) - ϕ in R in the several R bins in mid p_t .

bin	data	%	MC	%	data-MC	%
0	0.00066	0.96	0.00118	1.08	-0.00052	-43.92
1	0.00146	2.11	0.00204	1.87	-0.00058	-28.50
2	0.00624	9.02	0.00777	7.10	-0.00153	-19.70
3	0.00368	5.32	0.00506	4.62	-0.00138	-27.24
4	0.00564	8.15	0.00914	8.35	-0.00350	-38.33
5	0.00441	6.37	0.00912	8.33	-0.00471	-51.65
6	0.00345	4.98	0.00861	7.86	-0.00516	-59.97
7	0.00511	7.38	0.00964	8.80	-0.00453	-47.02
8	0.00721	10.41	0.01368	12.49	-0.00647	-47.32
9	0.00666	9.62	0.01041	9.51	-0.00376	-36.08
10	0.00882	12.75	0.01108	10.12	-0.00226	-20.42
11	0.01408	20.34	0.01823	16.65	-0.00415	-22.77
12	0.00179	2.59	0.00352	3.22	-0.00173	-49.10
sum	0.06920	100.00	0.10949	100.00	-0.04029	-36.80

Table D.14.: Deviation for the two data sets with Offline V0 finder - ϕ in R in the several R bins

bin	data	%	MC	%	data-MC	%
0	0.00486	4.78	0.00572	4.94	-0.00086	-15.11
1	0.00534	5.26	0.00628	5.42	-0.00094	-14.90
2	0.00919	9.04	0.01057	9.13	-0.00138	-13.09
3	0.00496	4.89	0.00572	4.94	-0.00075	-13.15
4	0.00846	8.33	0.00947	8.18	-0.00101	-10.65
5	0.00831	8.17	0.00912	7.88	-0.00082	-8.95
6	0.00763	7.51	0.00830	7.17	-0.00067	-8.08
7	0.00793	7.81	0.00889	7.67	-0.00095	-10.71
8	0.01058	10.41	0.01210	10.45	-0.00152	-12.55
9	0.00735	7.24	0.00858	7.40	-0.00122	-14.24
10	0.00902	8.88	0.01032	8.91	-0.00130	-12.58
11	0.01469	14.46	0.01698	14.66	-0.00229	-13.47
12	0.00327	3.22	0.00377	3.25	-0.00050	-13.32
sum	0.10160	100.00	0.11581	100.00	-0.01421	-12.27

Table D.15.: Deviation for the two data sets with Onfly V0 finder - ϕ in R in the several R bins

Bibliography

- [1] S. L. Glashow. *Symmetries of Weak Interactions*. Nucl. Phys, 22:579–588, 1962.
- [2] A. Salam. *Fundamental Theory of Matter: A Survey of Results and Methods*. In *Contemporary physics: Trieste Symposium: Proceedings of the International Symposium on Contemporary Physics organized by and held at the International Centre for Theoretical Physics, Trieste, from 7 to 28 June 1968*, volume 19, page 3. International Atomic Energy Agency, 1969.
- [3] A. Salam and others. *Weak and Electromagnetic Interactions in Elementary Particle Theory*, ed. N. Svartholm (Stockholm, 1968). Phys. Rev. D, 2:1285, 1970.
- [4] S. Weinberg. *A Model of Leptons*. Phys. Rev. Lett., 19(21):1264–1266, Nov 1967.
- [5] RJ Fries and B. Müller. *Heavy ions at LHC: Theoretical issues*. The European Physical Journal C-Particles and Fields, 34:279–285, 2004.
- [6] P. Braun-Munzinger and J. Stachel. *The quest for the quark-gluon plasma*. Nature, 448(7151):302–309, 2007.
- [7] C.Y. Wong. *Introduction to high-energy heavy-ion collisions*. World Scientific Pub Co Inc, 1994.
- [8] F. Karsch. *Lattice QCD at high temperature and density*. Lectures on Quark Matter, pages 209–249, 2002.
- [9] F. Karsch, E. Laermann, and A. Peikert. *Quark mass and flavour dependence of the QCD phase transition*. Nuclear Physics B, 605(1-3):579–599, 2001.
- [10] T. Matsui and H. Satz. *J/ψ suppression by quark-gluon plasma formation*. Physics Letters B, 178(4):416–422, 1986. ISSN 0370-2693.
- [11] J. D. Bjorken. *Energy Loss of Energetic Partons in Quark - Gluon Plasma: Possible Extinction of High $p(t)$ Jets in Hadron - Hadron Collisions*. FERMILAB-PUB-82-059-THY.
- [12] S. Turbide, C. Gale, S. Jeon, and G.D. Moore. *Energy loss of leading hadrons and direct photon production in evolving quark-gluon plasma*. Physical Review C, 72(1):14906, 2005.
- [13] D.E. Groom and S.R. Klein. *Passage of particles through matter*. The European Physical Journal C-Particles and Fields, 15(1):163–173, 2000.
- [14] M.K. Sundareshan. *Handbook of particle physics*. CRC, 2001.
- [15] *LHC webpage*.
URL <http://lhc.wb.cern.ch/lhc/>
- [16] *ALICE webpage*.
URL <http://aliceinfo.cern.ch/static/Documents>
- [17] K. Aamodt et al. *The ALICE experiment at the CERN LHC*. JINST, 3:S08002, 2008.

- [18] ALICE Collaboration. *ALICE Inner Tracking System (ITS): Technical Design Report*. Technical Design Report ALICE. CERN, Geneva, 1999.
- [19] ALICE collaboration collaboration collaboration collaboration. *Alignment of the ALICE Inner Tracking System with cosmic-ray tracks*. Journal of Instrumentation, 5(03):P03003, 2010. URL <http://stacks.iop.org/1748-0221/5/i=03/a=P03003>
- [20] J. Alme et al. *The ALICE TPC, a large 3-dimensional tracking device with fast readout for ultra-high multiplicity events*. Technical Report arXiv:1001.1950, Jan 2010. Comments: 55 pages, 82 figures.
- [21] ALICE Collaboration. *ALICE Time Projection Chamber (TPC): Technical Design Report*. Technical Design Report ALICE. CERN, Geneva, 2000.
- [22] ALICE Collaboration. *ALICE Transition-Radiation Detector (TRD): Technical Design Report*. Technical Design Report ALICE. CERN, Geneva, 2001.
- [23] C. Adler, A. Andronic, H. Appelshäuser, J. Bielcikova, C. Blume, P. Braun-Munzinger, D. Bucher, O. Busch, et al. *Position reconstruction in drift chambers operated with Xe, CO₂ (15%)*. Nuclear Instruments and Methods in Physics Research Section A: Accelerators, Spectrometers, Detectors and Associated Equipment, 540(1):140–157, 2005.
- [24] ALICE Collaboration. *ALICE Time-Of-Flight system (TOF): Technical Design Report*. Technical Design Report ALICE. CERN, Geneva, 2000.
- [25] ALICE Collaboration. *ALICE High-Momentum Particle Identification (HMPID): Technical Design Report*. Technical Design Report ALICE. CERN, Geneva, 1998.
- [26] ALICE Collaboration. *ALICE Photon Spectrometer (PHOS): Technical Design Report*. Technical Design Report ALICE. CERN, Geneva, 1999.
- [27] ALICE Collaboration. *ALICE Electromagnetic Calorimeter (EMCal): Technical Design Report*. CERN-LHCC-2008-014. ALICE-TDR-014. Geneva, Aug 2008.
- [28] ALICE Collaboration. *ALICE trigger data-acquisition high-level trigger and control system: Technical Design Report*. Technical Design Report ALICE. CERN, Geneva, 2004.
- [29] P. Giubellino. *Status of the ALICE Experiment*. Technical Report CERN-ALI-2002-003. CERN-ALICE-PUB-2002-03, CERN, Geneva, Mar 2002.
- [30] B. Alessandro, F. Antinori, JA Belikov, C. Blume, A. Dainese, P. Foka, P. Giubellino, B. Hippolyte, C. Kuhn, G. Martínez, et al. *ALICE: Physics performance report, volume II*. Journal of Physics G: Nuclear and Particle Physics, 32:1295–2040, 2006.
- [31] A. Marín (for the ALICE Collaboration). *Exploring the LHC medium with direct photons*. The European Physical Journal C, 61(4):735–740, 2009.
- [32] *Private communication with Markus Rammler*.
- [33] *Conversion Group*. URL <https://twiki.cern.ch/twiki/bin/view/ALICE/PWG4GammaConversion>
- [34] A. Marín, K. Aamodt, and K. Koch. *ALICE Conversion Software*. URL <http://alisoft.cern.ch/viewvc/branches/v4-18-Release/PWG4/GammaConv/>
- [35] S. Gorbunov and I. Kisel. *AliKF Package*. URL <http://alisoft.cern.ch/viewvc/branches/v4-18-Release/STEER/AliKFParticle.h>

- [36] S. Gorbunov and I. Kisel. *Reconstruction of decayed particles based on the Kalman filter.*
URL <http://www.gsi.documents/DOC-2007-May-14-1.pdf>
- [37] *Private communication with Mario Sitta, Marco van Leeuwen and Massimo Masera.*
- [38] *Private communication with Marek Kowalski and Danilo Vranic.*

Acknowledgements

My greatest debt is to Prof. Dr. Johanna Stachel, giving me the opportunity to carry out my bachelor thesis and to obtain an insight into high energy particle physics as well as photon physics in particular.

Furthermore I would like to thank PD Dr. Klaus Reygers for reading and evaluating my thesis. I would like to express my special thanks to Dr. Ana Marín for guiding and supporting me during my whole thesis.

I wish to express my gratitude to Kathrin Koch, Markus Rammner, Martin Wild, Eulogio Serradilla and the whole conversion group for all the support and discussions, which taught me a lot.

I would like to thank Silvia Masciocchi, Alexander Kalweit and the whole ALICE group at GSI for their help and especially for the possibility to use the GSI computer farm for the analysis and the simulations.

I wish to thank the detector experts of the ITS and TPC for their fruitful cooperation.

Moreover I appreciated the help of Jochen Thäder, who was reading the thesis.

In addition I would like to express my thanks to all people in the group providing such a kind working environment and help: Felix Reidt, Maren Hellwig, Mustapha Al-Helwi, Dr. Oliver Busch, Jochen Klein, Kai Schweda and many more.

Last not least, I want to thank my family and friends, especially my boyfriend Simon, for their support and their never ending patience.

Erklärung

Ich versichere, dass ich diese Arbeit selbständig verfasst habe und keine anderen als die angegebenen Quellen und Hilfsmittel benutzt habe.

Heidelberg, den 28. Juni 2010

Unterschrift:
Friederike Bock